

		ESA Contract:	1/6287/11/I-NB
		Doc. Title	D4200 Product Validation
		Doc. No	Report NCL_CRUCIAL_D4200
		Version No	3
		Date	30.08.17

**CryoSat-2 sUccess over Inland water And Land (CRUCIAL) Contract
1/6287/11/I-NB**

D4200 Product Validation Report (PVR)

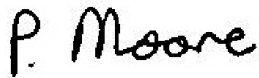
Document No: **NCL_CRUCIAL_D4200**

Issue: **3**

Issue Date: **30 August 2017**

		ESA Contract:	1/6287/11/I-NB
		Doc. Title	D4200 Product Validation Report
		Doc. No	NCL_CRUCIAL_D4200
		Version No	3
		Date	30.08.17

Author (Chapters 1-4): Philip Moore

Signature: 

Author (Chapter 5): Steve Birkinshaw

Signature: 

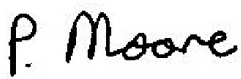
Author (Chapter 6): Peter Bauer-Gottwein

Signature: 

Author (Chapter 6): Raphael Schneider

Signature: 

Authorised by: Philip Moore

Signature: 

		ESA Contract:	1/6287/11/I-NB
		Doc. Title	D4200 Product Validation
		Doc. No	Report NCL_CRUCIAL_D4200
		Version No	3
		Date	30.08.17

Document Change Record

Version	Date	Modified by	Description
1	16.08.16	PM	Created
2	20.10.16	PM, P.B-G, RS	Corrections as recommended by ESA/ESRIN
3	30.08.17	PM	Consistency with D4400

		ESA Contract:	1/6287/11/I-NB
		Doc. Title	D4200 Product Validation
		Doc. No	Report NCL_CRUCIAL_D4200
		Version No	3
		Date	30.08.17

Abstract

This Product Validation Report summarises the validations of the methodologies described in the Algorithm Theoretical Basis Document (ATBD, D4100) used to estimate inland water heights from CryoSat-2 SAR and SARin FBR Level 1A data. In particular this report details comparisons of inland water heights from Cryosat-2 SAR and SARin L1A FBR data against in situ river gauge data and heights derived from the OSTM mission. In addition, use is made of data from ESA's Ground-Processing on demand (G-POD) services SARvatore (**SAR Versatile Altimetric Toolkit for Ocean Research & Exploitation**) and SARinvatore (**SARin Versatile Altimetric Toolkit for Ocean Research & Exploitation**). Cryosat-2 heights across the Brahmaputra are assimilated and utilized in hydrodynamic modelling.

		ESA Contract:	1/6287/11/I-NB
		Doc. Title	D4200 Product Validation
		Doc. No	Report NCL_CRUCIAL_D4200
		Version No	3
		Date	30.08.17

Contents

Abstract.....	4
Figures.....	7
Tables.....	12
1 Introduction	13
1.1 Purpose and Scope	13
1.2 Inland Water Studies.....	13
2 SAR/SARin waveforms from L1A data.....	18
2.1 Multi-look Analysis.....	18
2.2 Normalised Residual Error (NRE).....	20
2.3 G-POD SARvatore and SARinvatore	22
2.4 SARin analyses of cross angle.....	23
3 FBR Product and Validation.....	27
3.1 Tonlé Sap	27
3.2 Mekong.....	45
3.3 Amazon.....	57
4 SARin FBR Product and Validation	62
4.1 Ocean.....	62
4.2 Amazon.....	69
4.2.1 SARin Heights	69
4.2.2 Validation against gauge data at Tabatinga calibration.....	75
4.2.3 Analysis of the cross angle near the Tabatinga gauge	78
4.3 Brahmaputra.....	87
5 Summary of validation of FBR SAR and SARin inland water heights	90
6 Assimilation of CryoSat-2 data to 1-dimensional hydrodynamic models	92
6.1 Data and methods	93

		ESA Contract:	1/6287/11/I-NB
		Doc. Title	D4200 Product Validation
		Doc. No	Report NCL_CRUCIAL_D4200
		Version No	3
		Date	30.08.17

6.1.1 Hydrologic-hydrodynamic model of the Brahmaputra River	93
6.1.2 Cryosat-2 data	94
6.1.3 Processing of the data	95
6.1.4 Cross section calibration	95
6.1.5 DHI Data Assimilation Framework	97
6.1.6 Synthetic DA experiment.....	98
6.2 Results and Discussion.....	99
6.2.1 Discharge calibration.....	99
6.2.2 Cross section calibration	101
6.2.3 Results of synthetic DA.....	103
6.2.4 Results of real DA	105
6.3 Conclusions	107
7. References	109

		ESA Contract:	1/6287/11/I-NB
		Doc. Title	D4200 Product Validation
		Doc. No	Report NCL_CRUCIAL_D4200
		Version No	3
		Date	30.08.17

Figures

Figure 1: Pass across Tonlé Sap of 3 Dec 2011. 80 Hz burst data (black); running average over 4 points of burst data (blue) and multi-look with N=40 (red). The orthometric height is the height on the surface above the EGM96 geoid.	19
Figure 2: SAR empirical retracker. X-axis is gate number (1-256), Y-axis is power amplitude ...	21
Figure 3: Normalised Residual Error (NRE) for a pass across Tonlé Sap of 3 Dec 2011.	22
Figure 4: Schematic of water reflectors in SARin waveforms. The angle θ is the offset (cross angle) of the water reflectors from the nadir direction. B is the baseline between the two antennae.....	26
Figure 5: Map of the Mekong River including Tonlé Sap.	28
Figure 6: Google earth image of Tonlé Sap. The locations of the 62 Cryosat-2 heights are given by the yellow circles. The location of the two gauges are indicated by turquoise markers. The position of the S-N OSTM altimetric pass is given by the red marker.....	33
Figure 7: Cross-section of Tonlé Sap at Prek Kdam. X-axis is distance (m) across the river from point on the west embankment.	34
Figure 8: Cryosat-2 ground points across Tonlé Sap (3 Dec 2011) North to South pass.....	35
Figure 9: Geoid height measurements across Tonlé Sap (3 Dec 2011) with various multi-look combinations. Hamming window applied to waveforms. Upper: Retracked using empirical waveforms (Figure 2). Lower: OCOG/Threshold retracker used.....	36
Figure 10: Multi-look waveforms (#116-121 top left – lower right) across Tonlé Sap on 3 Dec 2011 at times 18647.03-18647.26 s constructed from a stack with N=10 (green), N=40 (red), N=110 (blue) using Hamming weighting. X-axis is gate number (1-256 in SAR mode), Y-axis is power amplitude.....	37
Figure 11: Waveforms (# 117-121, 175 top left to lower right) across Tonlé Sap on 3 Dec 2011. N=123 with cosine weighting (blue), N=123 unit weight (green) and G-POD (red). Waveforms #117-121 over water, #175 on land near edge of Tonlé Sap. X-axis is gate number (1-256 in SAR mode), Y-axis is power amplitude.	39
Figure 12: Waveforms (# 117-121, 175 top left to lower right) across Tonlé Sap on 3 Dec 2011. N=123 with cosine weighting (blue), N=123 unit weight (green) and G-POD (red). Zoomed version of Figure 10. X-axis is gate number (1-256 in SAR mode), Y-axis is power amplitude.	40

		ESA Contract:	1/6287/11/I-NB
		Doc. Title	D4200 Product Validation
		Doc. No	Report NCL_CRUCIAL_D4200
		Version No	3
		Date	30.08.17

Figure 13: WF #117 across Tonlé Sap on 3 Dec 2011. Waveforms aligned at peak (amplitude and bin). G-POD (equivalent to N=120), and N=110, 40. The earlier bin retracked point for large N causes the range to surface to decrease, i.e. the land/water height above reference ellipsoid (and hence orthometric height) to increase. Lower N increases the noise on the waveform tail..... 41

Figure 14: Time series of aligned heights across Tonlé Sap. OSTM black points, Cryosat-2 red and Prek Kdam gauge heights blue points. 43

Figure 15: Google Earth image of 19 Apr 2011 Mekong crossing. Satellite ground track N-S..... 46

Figure 16: Estimated orthometric heights of 19 Apr 2011 Mekong crossing. In both plots G-POD heights (red) and retracked G-POD waveforms (blue). CRUCIAL cosine weighted waves (green) using N=110 in upper plot and N=40 in lower plot..... 47

Figure 17: Location of 5 gauges along the Mekong, the Khone Phapheng Falls and the 0 km chainage point of Fig. 18..... 48

Figure 18: SAR FBR heights along the Mekong (N=40). Gauges and range identified by lines/circles. Circles at gauge show low water level (Dec-Apr) and high water level (Aug-Sep). Gauges at Mukdahan, Khong Chiam, Pakse, Stung Teng, Kratie ordered from low to high chainage. Low water level (Dec-Apr). High water level Waterfall located at chainage 620km. The 0 km chainage location corresponds to (18.23536°N, 104.0412°E). 50

Figure 19: Comparison of Kratie gauge data with heights from near-by altimetric points from NCL (this study; N=110) and DTU. RMS 91.9 cm (NCL, empirical retrackers) and 96.8 cm (DTU)..... 52

Figure 20: Comparison of Kratie gauge data with heights from near-by altimetric points from NCL (this study) waveforms using N=40. RMS 67.8 cm (empirical retrackers) and 66.9 cm (OCOG/Threshold) using 3σ rejection level..... 53

Figure 21: As Figure 20 but for gauge at Stung Teng. All data included, no rejection criterion has been applied. 54

Figure 22: As Figure 20 but for gauge at Pakse. All data included, no rejection criterion has been applied. 55

Figure 23: As Figure 20 but for gauge at Khong Chiam. All data included, no rejection criterion has been applied..... 56

Figure 24: As Figure 20 but for gauge at Mukhadan. All data included, no rejection criterion has been applied. 57

		ESA Contract:	1/6287/11/I-NB
		Doc. Title	D4200 Product Validation
		Doc. No	Report NCL_CRUCIAL_D4200
		Version No	3
		Date	30.08.17

Figure 25: Google earth image of location near the Obidos gauge on the Amazon. Yellow hinge markers denote centre line of stretch considered for Cryosat-2 crossings. 59

Figure 26: Google earth image of location near the Manacapuru gauge on the Amazon. Green hinge markers denote centre line of stretch considered for Cryosat-2 crossings..... 60

Figure 27: FBR SAR heights (N=40, empirical retrackers) at Obidos (RMS 18.5 cm)..... 60

Figure 28: FBR SAR heights (N=40, empirical retrackers) at Manacapuru (RMS 52.6 cm)..... 61

Figure 29: Cryosat-2 descending pass on 28 April 2011 off the Amazon estuary. Cryosat-2 in SARin mode..... 64

Figure 30: Sea surface heights from SARin pass on 28 April 2011. G-POD values SSH_20Hz-MSS (blue) and OCOG1-MSS (green). 65

Figure 31: Sea surface heights from SARin pass on 28 April 2011. G-POD values SSH_20Hz-MSS (blue) and Emp1-MSS (green)..... 67

Figure 32: Top plot: multi-look waveforms (N=60) from the two Cryosat-2 antennae. Middle plot: coherence. Lower plot: phase differences between antennae over the bins (deg). Left plots for oceanic location 2.606878N, 49.262229W, right plots for oceanic location 2.062831N, 49.318856W..... 68

Figure 33: Derived slope from ocean pass (North to South) of 28 April 2011. Sub-satellite points hit land about latitude 0.4°N. Running average over 40 points (red curve) to show long-wavelength signatures. Standard deviation of points 0.4-3.0°S is 0.0034°, mean -0.00056° 69

Figure 34: Ascending Cryosat-2 ground track across Amazonas 5 May 2012 (SARin mode)..... 71

Figure 35: Multi-looked SARin waveforms across Amazon 5 May 2012. CRUCIAL waveforms N=60 (blue curves) ; G-POD SARin waveforms (green curves)..... 73

Figure 36: Heights derived by retracking multi-look SARin waveforms (N=60) across Amazon on 5 May 2012. G-POD heights from SARinwaveforms. 74

Figure 37: As Figure 36 but with G-POD waveforms retracked. 74

Figure 38: Google earth image of Amazon near Tabatinga. Gauge marked in red. Yellow markers denote centre line of stretch considered for Cryosat-2 crossings. 76

Figure 39: Tabatinga gauge heights and Cryosat-2 SARin (N=60, OCOG/Threshold) heights corrected for river slope. RMS difference 29.9 cm. 77

Figure 40: Plot of the 64 accepted cross angles comprising 44 ascending passes (black squares) and 20 descending passes (red squares). 77

		ESA Contract:	1/6287/11/I-NB
		Doc. Title	D4200 Product Validation
		Doc. No	Report NCL_CRUCIAL_D4200
		Version No	3
		Date	30.08.17

Figure 41: SARin waveforms (upper), coherence (middle) and cross angle in degrees (lower). In the upper plot the right antennae is coloured blue and the left antennae is green. X-axis is bin number; Y axis is power (upper), coherence (middle) and degree (lower). Left hand column location #274 (3.930 °S 70.207 °W); right hand column location #275 (3.927 °S 70.207 °W). Date of pass 5 May 2012. 80

Figure 42: OCOG/Threshold based difference between heights from the two SARin antennae (Upper). Cross angle (Lower). SARin Amazonas 5 May 2012. (Latitude -4.2° corresponds to longitude 70.179°W)..... 81

Figure 43: Google earth plot of ascending pass on 5 May 2012 across Amazon near Tabatinga (upper). Cross angles (deg) from SARin mode. The blue arrow points along direction of flight..... 82

Figure 44: Google earth plot of ascending pass on 25 August 2012 across Amazon near Tabatinga (upper). Cross angles (deg) from SARin mode (lower). The blue arrow points along direction of flight..... 83

Figure 45: Google earth plot of descending pass on 8 September 2012 across Amazon near Tabatinga (upper). Cross angles from SARin mode (lower). The blue arrow points along direction of flight. 84

Figure 46: Google earth plot of ascending pass on 23 September 2012 across Amazon near Tabatinga (upper). Cross angles (deg) from SARin mode (lower). The blue arrow points along direction of flight. 85

Figure 47: Google earth plot of ascending pass on 22 October 2012 across Amazon near Tabatinga (upper). Cross angles (deg) from SARin mode (lower). The blue arrow points along direction of flight. 86

Figure 48: Cryosat-2 SARin heights across the Brahmaputra. CRUCIAL heights (N=60, OCOG/Threshold) (black squares) and DTU derived heights (red squares)..... 88

Figure 49: The height difference between NCL and DTU heights across the Brahmaputra. Accepted points denoted by black squares, rejected points by red squares. Mean difference and standard deviation of accepted points 11.9cm and 15.8 cm, respectively. 89

Figure 50: The Brahmaputra basin model. The main discharge calibration station, Bahadurabad in Bangladesh is shown. Furthermore, the stretch of the model (the Assam Valley) relevant for the DA is highlighted, along with the Envisat virtual stations used in the cross section calibration..... 94

Figure 51: Section of the Brahmaputra in the Assam valley showing the Landsat river mask, the Cryosat-2 observations and their mapping to the 1D river model, all for 2013. 95

		ESA Contract:	1/6287/11/I-NB
		Doc. Title	D4200 Product Validation
		Doc. No	Report NCL_CRUCIAL_D4200
		Version No	3
		Date	30.08.17

Figure 52: Sketch of the two-step cross section calibration process for one cross section, displaying the optimization parameters datum and angle. 96

Figure 53: Flow chart showing the calibration of both discharge and water levels in the hydrodynamic model..... 97

Figure 54: Overview over the DHI Data Assimilation Framework. Source: Marc-Etienne Ridler, DHI. 98

Figure 55: Simulated discharge at Bahadurabad station together with in situ observations. Calibration period: 2002 - 2007, validation period: 2010 – 2013..... 100

Figure 56: Result of the cross section calibration step 1 for the Assam Valley for the period 2010 to 2013. All levels are shown relative to the reference model's cross section datums based on SRTM DEM. 102

Figure 57: Result of the cross section calibration step 2 for one virtual station. All levels are relative to the water levels at the time of the first Envisat observation. The orbit provides a 35 day repeat cycle..... 103

Figure 58: Results of the DA of *synthetic* Cryosat-2 data in terms of *discharge* at Bahadurabad station. The times of synthetic observations are marked with green dots on the x-axis. . 104

Figure 59: Results of the DA of *synthetic* Cryosat-2 data in terms of water level at Bahadurabad station. The times of synthetic observations are marked with green dots on the x-axis. . 104

Figure 60: Relative CRPS of the DA experiment compared to the respective open-loop run along the river. Values smaller than 1, i.e. below the black line indicate that the model predictions are improved by DA..... 105

Figure 61: Results of the DA of *real* Cryosat-2 data in terms of *discharge* at Bahadurabad station. The times of observations are marked with green dots on the x-axis. 106

		ESA Contract:	1/6287/11/I-NB
		Doc. Title	D4200 Product Validation
		Doc. No	Report NCL_CRUCIAL_D4200
		Version No	3
		Date	30.08.17

Tables

Table 1: Statistics of fit for pass across Tonlé Sap. G-POD: value from (indices 94:161) closest fit to CRUCIAL ground points in time; in parentheses values from indices 95-162. CRUCIAL values: top cosine weighting; lower unit weight.....	38
Table 2: Tracker types (see D4100) for the Tonlé Sap points. The single peak column is the sum of columns 1-3 and the dual peak column that of 4-5. A total of 68 waveforms were retracked.....	42
Table 3: Time difference and auto-correlations between gauge data at Prek Kdam against the Kumong Luong gauge data and OSTM altimetric heights.	44
Table 4: RMS differences between gauge data at Prek Kdam advanced 12 days and OSTM and Cryosat-2 altimetric heights.	44
Table 5: Details of the 5 gauges along the Mekong including low water level, the high water level to low water level range, chainage from the upstream point corresponding to the northern limit of the SAR mask and the chainage range for the altimeter height comparisons.	49
Table 6: Statistics from over 800 ocean points from pass on 28 April 2100. Data covers lat. 3.01484°S – 0.083832°S. Cryosat-2 in SARin mode.	66
Table 7: Statistics of cross track angles from the 64 passes near Tabatinga. The expected value of the slope from SARin height differences is -0.0025°.	78
Table 8: Performance criteria for simulated discharge Q at Bahadurabad station. bias = $(Q_{sim} - Q_{obs})/Q_{sim}$	101
Table 9: Results of DA experiments shown in Figure 58 and Figure 61 in terms of discharge at Bahadurabad station. Sharpness is given as the width of the 90% confidence intervals ..	106

		ESA Contract:	1/6287/11/I-NB
		Doc. Title	D4200 Product Validation
		Doc. No	Report NCL_CRUCIAL_D4200
		Version No	3
		Date	30.08.17

1 Introduction

1.1 Purpose and Scope

CryoSat-2 was launched on 8 April 2010. It follows on from previous ESA Earth orbiting satellite radar altimeters (e.g. ERS2 and Envisat) that have been used for land surface applications including mapping and measurement of river and lake systems. CryoSat-2's primary instrument is SIRAL (SAR Interferometric Radar Altimeter), which uses radar pulses to determine and monitor the spacecraft's altitude. Although the CryoSat-2 primary aim is to measure sea ice and ice sheets it can provide valuable data over the rest of the Earth surface. SIRAL operates in one of three modes, depending on where (above the Earth's surface) CryoSat-2 is flying. The three modes are: the conventional altimeter mode or Low resolution Mode (LRM), the Synthetic Aperture Radar (SAR) mode and Interferometric Synthetic Aperture Radar (SARin) mode. CryoSat-2 is in a low non Sun-synchronous Earth orbit of period of 100 minutes. The orbit of Cryosat-2 drifts across the Earth's surface with a repeat cycle of 369 days.

This study is investigating innovative land and water applications from CryoSat-2 with a forward-look component to the future Sentinel-3 mission. This Product Validation Report presents the approach developed to process and utilize SAR FBR data over inland waters. It does not consider LRM data as that is relatively well understood from previous missions and is not relevant for Sentinel 3 processing. This report thus focuses on SAR FBR and SARin FBR data and hydrological modelling

Deliverable D4200 presents the product and validation of the theoretical and computational aspects of the SAR FBR and SARin FBR algorithms and hydrological modelling described in D4100 (ATBD).

1.2 Inland Water Studies

Over the last two decades inland water studies using space altimetry provided valuable results over lakes (e.g. Birkett, 1995, Crétaux and Birkett, 2006, Song et al., 2014, 2015a,b), rivers (e.g. Frappart et al., 2006; Birkett et al., 2002 and Becker et al., 2014) and wetlands (e.g. Frappart et al., 2005, and Zakharova et al., 2014). ESA has funded previous studies including the River & Lakes

		ESA Contract:	1/6287/11/I-NB
		Doc. Title	D4200 Product Validation
		Doc. No	Report NCL_CRUCIAL_D4200
		Version No	3
		Date	30.08.17

(R&L) contract utilizing ERS-2 and Envisat altimeter missions over land and inland waters including mapping (Berry et al, 2010a,b,c ; Smith & Berry 2011) and measurement of river and lake systems (Berry, 2009; Wheeler et al., 2010, Berry et al., 2012a,b). All such studies utilized standard nadir pointing altimetry while the CryoSat-2 mission is the first to operate a SAR mode altimeter. With the exception of ERS-1 in its geodetic phase and now Cryosat-2 all previous altimeter missions have a repeat orbit in which the satellite follows the same ground-track after a number of days; 35 days for ERS-2 and Envisat and 10 days for Topex/Posidon, Jason-1, Jason-2 (OSTM) and the recently launched Jason-3 (OSTM2). This presents an added difficulty for hydrological modelling as well as for the validation as the crossing points of inland waters migrate with the ground track. Studies of Cryosat-2 over inland waters include Villadsen et al. (2015) for the Ganges-Brahmaputra basin. In that study the amplitude and phase of peak flow from retracked SARin Level 1B waveforms was compared against Envisat results. The results showed agreement with the largest difference in amplitude of about 30 cm and mean difference of about 10 cm. The phase of the annual variation captured by CryoSat-2 had a mean difference of 2.7 days with Envisat results.

Water heights from Cryosat-2 retracked Level 1B SAR waveforms were compared against gauge levels from 5 lakes in Scandanavia (Nielsen et al., 2015). The authors utilize a static and a dynamic model, the latter using observations that are close in time. The dynamic model provides reliable heights even for noisy and sparse data while the static approach fails on occasions. A dynamic approach is viable over slowly fluctuating lake levels with multiple passes but cannot be transferred to a river with highly fluctuating water levels even at close time intervals. The rms values presented in that paper show agreement with gauge data at the 5-16 cm level for the larger lakes. The paper infers that for smaller lakes Cryosat-2 derived heights are of higher accuracy compared to Envisat heights.

Song et al. (2014, 2015a,b) used Cryosat-2 altimetry and ICESat data to investigate change in lakes levels over the Tibetan Plateau. The authors used Level 2 heights from SARin data. Comparisons against two gauges (Song et al., 2015a) for Tibetan lakes yielded a rms value of 0.18 m for Namco and 0.28 m for Yamzhog Yumco. Over Lake Nasser, Kleinherenbrink et al. (2014) used retracked SARin Level 1B waveforms. A comparison against Jason-2 altimetric heights yielded an rms of 0.30 m which was an enhancement over the 0.73 m rms from Level 2 data. The level 2 retracker errors range from 0.23 m over tracks with hardly any waveform pollution to 0.75 m with waveform pollution. The authors defined waveform pollution to be where several peaks were present in the cross-correlation function, which results in multiple elevations. Their retracker improves these values to 0.13 m and 0.21 m respectively. A dominant error source of about 0.2 m is the water surface slope caused by wind conditions and/or geoid errors.

		ESA Contract:	1/6287/11/I-NB
		Doc. Title	D4200 Product Validation
		Doc. No	Report NCL_CRUCIAL_D4200
		Version No	3
		Date	30.08.17

1.2 Abbreviations and Acronyms

Abbreviation	Meaning
ASCII	American Standard Code for Information Interchange
ATBD	Algorithm Theoretical Basis Document
CRPS	Continuous Ranked Probability Score
CRUCIAL	CryoSat-2sUCcess over Inland water And Land
DA	Data Assimilation
DEM	Digital Elevation Model
DHI	Danish Hydraulic Institute
DTU	Danish Technical University
EGM96	Earth Gravity Model 1996
EGM08	Earth Gravity Model 2008
EnKF	Ensemble Kalman filter
ERS-1/2	European Remote Sensing satellites 1 and 2
ETKF	Ensemble Transform Kalman Filter
ERS2	European Remote Sensing satellite 2
Envisat	Environmental Satellite
ESA	European Space Agency
FBR	Full Bit Rate
FFT	Fast Fourier Transform
G-POD	ESA's Ground-Processing On Demand service
L1A	Level 1A
L1B	Level 1B

		ESA Contract:	1/6287/11/I-NB
		Doc. Title	D4200 Product Validation
		Doc. No	Report NCL_CRUCIAL_D4200
		Version No	3
		Date	30.08.17

LOTUS	Preparing Land and Ocean Take Up from Sentinel-3 (project supporting the development of GMES)
LRM	Low Resolution Mode
JASON	US/French Altimeter Satellite
MIKE	Generalized River Modeling Package
MSS	Mean Sea Surface
NCL	Newcastle University
NDVI	Normalised Difference Vegetation Index
NRE	Normalised Residual Error
NSE	Nash-Sutcliffe efficiency
OCOG	Offset Centre of Gravity
OSTM	Ocean Surface Topography Mission (JASON-2)
POCA	Point of Closest Approach
PVR	Product Validation Report
RA	Radar Altimeter
RMS	Root Mean Square
R&L	River and Lake
SAMOSA	SAR Altimetry MOde Studies and Applications
SAR	Synthetic Aperture Radar mode of CryoSat-2 SIRAL
SARin	Interferometric Synthetic Aperture Radar mode of CryoSat-2 SIRAL
SARvatore	SARin Versatile Altimetric Toolkit for Ocean Research & Exploitation
SARinvatore	SARin Versatile Altimetric Toolkit for Ocean Research & Exploitation
Sentinel-3	ESA Earth Observation Satellite Mission
SIRAL	SAR Interferometric Radar Altimeter
SRTM	Shuttle Radar Topography Mission

		ESA Contract:	1/6287/11/I-NB
		Doc. Title	D4200 Product Validation
		Doc. No	Report NCL_CRUCIAL_D4200
		Version No Date	3 30.08.17

SSH	Sea Surface Height
TRMM	Tropical Rainfall Measuring Mission
USDA	United States Department of Agriculture
WF	Waveform
.NET/C#	C# programs run on the .NET Framework

		ESA Contract:	1/6287/11/I-NB
		Doc. Title	D4200 Product Validation
		Doc. No	Report NCL_CRUCIAL_D4200
		Version No	3
		Date	30.08.17

2 SAR/SARin waveforms from L1A data

This section provides a quick overview of the SAR/SARin processing methodology. Full details are available in D4100.

2.1 Multi-look Analysis

In the SAR (SARin) mode the burst echoes at 80 (20) Hz are processed through the following steps

- Range FFT over 64 pulses in burst
- Beam formation and steering to nadir direction
- Form burst centre ground points from OCOG/Threshold retracker applied to nadir beam
- Form a sequence of ground points at beam angle using a coarse approximate steering
- Beam formation and steering to ground points
- Stack beams pointing at ground points
- Apply slant range correction, tracker range correction and Doppler range correction
- Height retrieval from empirical and OCOG/Threshold retrackers.

The multi-look waveforms for both SAR and SARin mode are about 320 m along the ground track; that is a reduction of resolution of a factor four compared to the burst echo separation. The orthometric height, that is the surface height above the geoid, for the burst centre ground points are derived by using the EGM96 model for ease of computation. EGM96 can be replaced by a higher resolution model such as EGM08 or a GRACE/GOCE model but at additional computational cost. Trials using EGM08 has negligible impact and hence the simpler lower order model was retained for this intermediate step. The higher resolution geoid model EGM08 was utilised in the final height retrieval step to derive the orthometric height.

An accurate geoid model should give constant orthometric heights across lake surfaces. Schwatke et al. (2012) showed that physical heights for large lakes, derived with EGM2008 are not flat and that gravity field models from GOCE indicate significant errors of EGM2008 in over land. The authors generated hybrid models by extending the GOCE models by the high frequency parts of EGM2008. Although these hybrid models improved the heights deviations from a flat surface

		ESA Contract:	1/6287/11/I-NB
		Doc. Title	D4200 Product Validation
		Doc. No	Report NCL_CRUCIAL_D4200
		Version No	3
		Date	30.08.17

remained indicating residual geoid error. However, within this project we utilized EGM08 but acknowledge that a small improvement may be observed with one of these hybrid models.

A pertinent question for inland water applications is whether the burst echoes can supply useful heights at the higher spatial and temporal resolution. As an illustration, Figure 1 shows the orthometric heights for the pass on 3 Dec 2011 across Tonlé Sap, Cambodia (see section 3.1 for further details). The figure shows the burst echoes heights derived by using the OCOG/Threshold retracker. Also given are heights from the stack forming the multi-look. The burst echo heights are considerably noisier than the multi-look data. To provide comparability at about 300 m resolution, a running average over 4 burst echo heights is also plotted but this also shows that the burst echoes by themselves cannot provide the precision of the multi-look approach. The speckle in the burst echo data affects the recovered heights and only through stacking and forming multi-look waveforms can precise heights be recovered. Burst echo heights are output for all passes studied within this project with similar results.

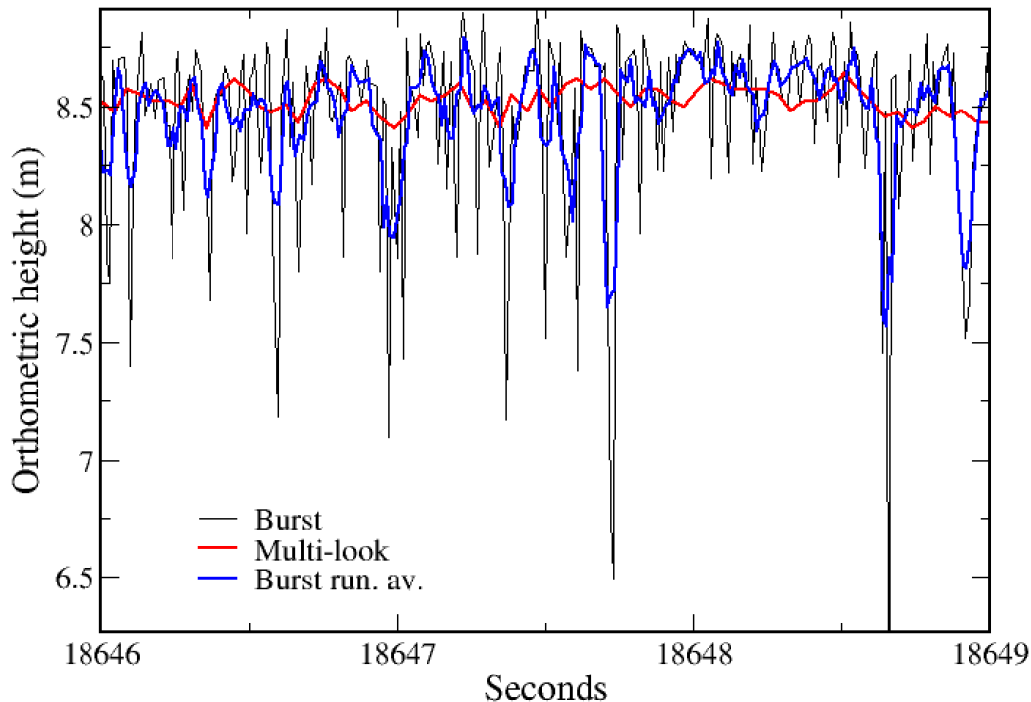


Figure 1: Pass across Tonlé Sap of 3 Dec 2011. 80 Hz burst data (black); running average over 4 points of burst data (blue) and multi-look with N=40 (red). The orthometric height is the height on the surface above the EGM96 geoid.

		ESA Contract:	1/6287/11/I-NB
		Doc. Title	D4200 Product Validation
		Doc. No	Report NCL_CRUCIAL_D4200
		Version No	3
		Date	30.08.17

2.2 Normalised Residual Error (NRE)

The waveforms derived from SAR and SARin data (see D4100) are multi-looked using a weighting scheme based on the Hamming window. The weighting provides a unit weight for the central burst beam ($n=0$) with minimum angle to the ground-point with other weights decreasing as the beam angle increases for bursts before and after this central beam, via

$$w(n) = 0.54 + 0.46 \cos(\pi n / N) \quad (1)$$

where N is the number of beams before or after the burst of minimum beam angle and $n = 0, \pm 1, \pm 2, \dots, \pm N$. We note that Eq. (1) is equivalent to the usual expression for a Hamming window as the usual definition has $2\pi n / 2N$ for the cosine argument. As an example of Eq. (1), for $N=40$, 81 waveforms centred on the beam directed closest to nadir are considered (for this reason, n has positive and negative values).

For retracking, empirical waveforms described in D4100 and plotted in Figure 2 were fitted to the observed multi-look waveforms using a least squares approach and solving for the location of the peak(s), the peak amplitude and the rate of exponential rise and decay of the peak. The best fitted empirical waveform in the sense of the lowest Normalized Residual Error

$$NRE = \frac{\sum_{i=1}^{B_{\max}} (P_i^{obs} - P_i^{mod})^2}{\sum_{i=1}^{B_{\max}} (P_i^{obs})^2} \quad (2)$$

was chosen. In Eq. 2 P_i^{obs} , P_i^{mod} are the observed and modelled power within bin i , respectively. In practice, single peak waveforms were preferred unless the NRE reduced by 10% or more with dual peaks to avoid over parameterization. The NRE in Eq. 2 is the sum of the residual power squared normalized with respect to the total waveform power squared. For SAR waveforms $B_{\max} = 256$; the 256 samples being derived from zero padding the original 128 samples for SAR. For SARin $B_{\max} = 1024$; i.e. zero padding the original 512 samples (Wingham et al., 2006). Figure 3 plots the NRE for the pass across Tonlé Sap on 3 Dev 3011. The NRE is typically 0.03 or less for waveforms that conform to one of the expected empirical retrackers. NRE values about this value indicate a complex waveform that may be indicative of contamination by other reflectors than the target. Values in excess of 0.3 indicate a very poor fit and are discarded for height extraction purposes.

		ESA Contract:	1/6287/11/I-NB
		Doc. Title	D4200 Product Validation Report
		Doc. No	NCL_CRUCIAL_D4200
		Version No	3
		Date	30.08.17

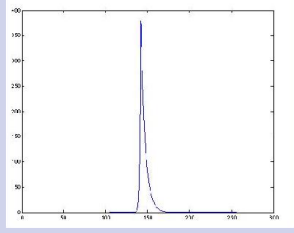
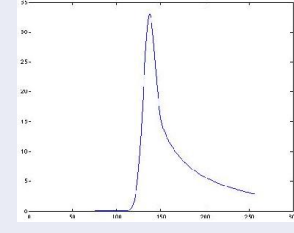
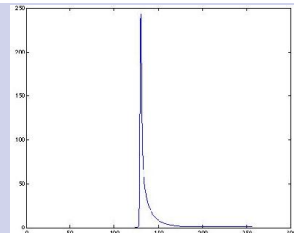
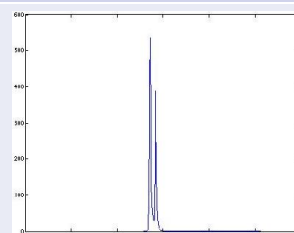
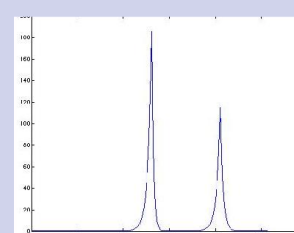
Retracker #	Description	Waveform Shape
1	Specular (still water)	
2	Ocean like (ruffled water)	
3	Ocean like with fall away at high # bins (ruffled waters)	
4	Two specular peaks (strong returns off two patches of still water)	
5	Retracker Type 2 with additional specular peak (ruffled and still water)	

Figure 2: SAR empirical retracker. X-axis is gate number (1-256), Y-axis is power amplitude

		ESA Contract:	1/6287/11/I-NB
		Doc. Title	D4200 Product Validation
		Doc. No	Report NCL_CRUCIAL_D4200
		Version No	3
		Date	30.08.17

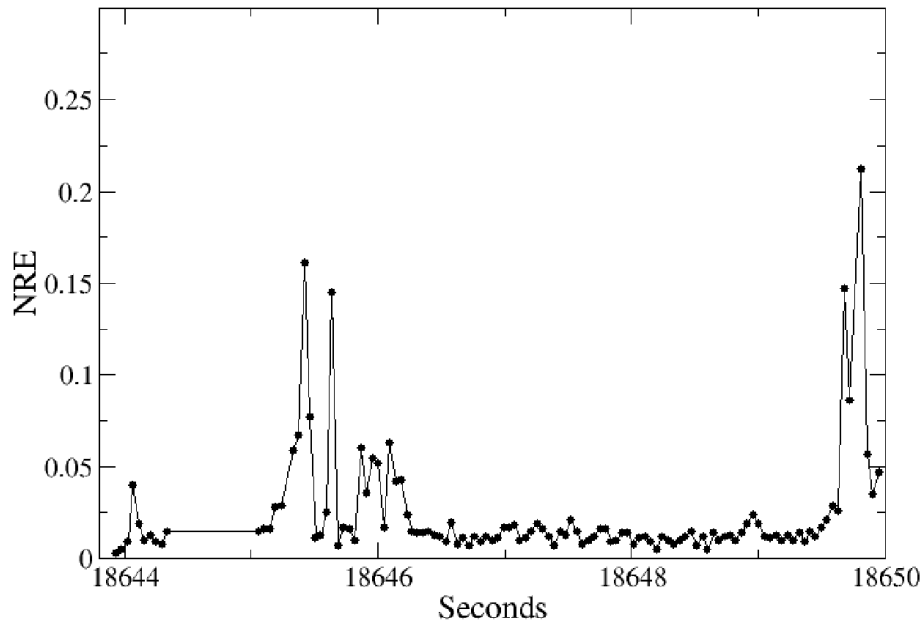


Figure 3: Normalised Residual Error (NRE) for a pass across Tonlé Sap of 3 Dec 2011.

2.3 G-POD SARvatore and SARinvatore

Within the validation analyses of this document, usage has been made of data downloaded from ESA’s Ground-Processing on demand (G-POD) services SARvatore (**SAR** Versatile Altimetric Toolkit for **Ocean Research & Exploitation**) and SARinvatore (**SARin** Versatile Altimetric Toolkit for **Ocean Research & Exploitation**). The SARvatore service can be accessed by using the link <http://wiki.services.eoportal.org/tiki-index.php?page=GPOD+CryoSat-2+SARvatore+Software+Prototype+User+Manual>. Both SAR and SARIN multi-look waveforms and heights derived by retracking with the SAMOSA2 retracker (Gommenginger et al., 2010) were downloaded. SARvatore and SARinvatore use all available waveforms in the stack to form the multi-look waveform. Note that the L2 products include the Stack Beam Index which gives the index of beams from 1 (minimum possible) to 260 (maximum possible) that have been summed to form the multi-look waveform. The SARvatore/SARinvatore orthometric heights, were derived from

$$GPOD_Ortho_20Hz = SSH_20HZ - EGM_2008_20Hz \quad (3)$$

		ESA Contract:	1/6287/11/I-NB
		Doc. Title	D4200 Product Validation
		Doc. No	Report NCL_CRUCIAL_D4200
		Version No	3
		Date	30.08.17

where SSH_{20Hz} are the sea-surface heights at 20HZ and $EGM_{2008_{20Hz}}$ the corresponding geoid heights from EGM2008.

Retracking of the waveforms using an alternative retracker to SAMOSA2 has been undertaken as part of CRUCIAL. Comparable heights to $GPOD_{Ortho_{20Hz}}$ utilise

$$\begin{aligned}
 GPOD_{Ortho_{20Hz}_{retrack}} = & altitude_{20Hz} - Window_{delay_{20Hz}} * c / 2 \\
 & + ht_{retrack_{20Hz}} - EGM_{2008_{20Hz}} \\
 & - GEO_{corr_{land_{20Hz}}}
 \end{aligned} \tag{4}$$

where $altitude_{20Hz}$ is the satellite altitude above the reference ellipsoid, $Window_{delay_{20Hz}}$ the two way time for the altimeter echo; c the speed of light, $GEO_{corr_{land_{20Hz}}}$ the geophysical corrections and $ht_{retrack_{20Hz}}$ the retracked height.

2.4 SARin analyses of cross angle

This section is taken from D4100 and included here for completeness. For SARin the power is recovered for the right and left antennae separately. The power of the multi-look waveforms is retracked to provide the height from the two antennae. Other parameters useful for SARin include the cross-power

$$\psi_{ml}^* = \sum_{i=1}^{N_{ml}} w_{b_i} \psi_{b_i}^+ \bar{\psi}_{b_i}^- / \sum_{i=1}^{N_{ml}} w_{b_i} ; \tag{5}$$

the multi-looked argument or phase, $A\psi_{ml}$,

$$A\psi_{ml} = Arg(\psi_{ml}^*); \tag{6}$$

and the multi-look coherence,

$$C\psi_{ml} = \frac{|\psi_{ml}^*|}{(P\psi_{ml}^+ P\psi_{ml}^-)^{1/2}} \tag{7}$$

		ESA Contract:	1/6287/11/I-NB
		Doc. Title	D4200 Product Validation
		Doc. No	Report NCL_CRUCIAL_D4200
		Version No	3
		Date	30.08.17

Eq. (6) and Eq. (7) are essentially those in Wingham et al. (2006) except that the full weighting in the multi-look waveforms is included in Eq. (5) rather than unit weighting of Wingham et al. The denominator in Eq. (7) utilizes the power of both antennae so that $C\psi_{ml} = 1$ if $\psi_{b_i}^+ = \psi_{b_i}^-$ for all waveforms i in the stack. The coherence of Eq. (7) can be influenced by the characteristics of the observed scenario (flat/rough surface).

Similar to Wingham et al. (2006) we propose determining the phase difference by minimizing the functional

$$\frac{C\psi_{ml}^3(\tau)}{1 - C\psi_{ml}(\tau)} (A\psi_{ml}(\tau) - g(\tau, \chi))^2 \quad (8)$$

with respect to parameters $\chi = \{\chi_1, \chi_2\}$ where

$$g(\tau, \chi) = \begin{cases} \chi_1 & \tau < \tau_0 \\ \chi_1 + \chi_2(\tau - \tau_0) & \tau > \tau_0 \end{cases} \quad (9)$$

In Eq. (9) τ_0 is the time determined from the range retracker. After determining χ_1 the surface slope or cross angle is recovered from

$$\theta = \sin^{-1}(\chi_1 / (k_0 \beta)) + \theta_{roll} \quad (10)$$

where θ_{roll} is the roll angle. In Eq. (10) k_0 is the carrier wave-number and β the interferometer baseline. The roll-angle can be biased and should be modified accordingly to avoid errors in the estimation of the height. This will be done in section 4.2.2.

Over ice margins the reflectance will come from the cross-track slice of the footprint. Given the wavelength of the altimeter (2.21 cm) the surface slope is limited to 1.08 degrees. Similarly, over oceans the footprint will be completely oceanic except near land and Eq. 9 gives the slope of the oceanic surface. For inland water surfaces, excluding large lakes, the dominant water reflectors will not be symmetric across the footprint slice and hence the interpretation of θ as the ground slope is incorrect. In fact, analysis of the waveforms from the two antennae in SARin mode assumes that the two waveforms illuminate the same surface area. Consider the schematic of Figure 4 where the dominant reflectors are from the water but where the water surface is offset from nadir. For simplicity we choose the centre of the water body in the cross track direction to give the retracked point. Note that if two water identical reflectors are present but situated on

		ESA Contract:	1/6287/11/I-NB
		Doc. Title	D4200 Product Validation
		Doc. No	Report NCL_CRUCIAL_D4200
		Version No	3
		Date	30.08.17

either side of the nadir direction between the two antennae then the summed effects would cancel to give a zero angle for θ . Thus, the angle θ is a sum of the effects of all water reflectors in the window and now gives the cross angle of the reflectance; that is the angle of the summed reflectance of the water body from the nadir direction. The first returned signal will be from the water body closest to the nadir in the cross-track direction. If this body is substantial, this will form the leading edge for tracking.

The computations with the cross angle use the convention of left antennae minus right antennae. Thus the phase difference will be positive if the target range using the left antennae exceeds that of the right antennae. Thus, for the schematic of Figure 4 with the satellite flying into the page, the cross track angle will be positive, giving a target to the right of the nadir point of the antennae center.

		ESA Contract:	1/6287/11/I-NB
		Doc. Title	D4200 Product Validation
		Doc. No	Report NCL_CRUCIAL_D4200
		Version No	3
		Date	30.08.17

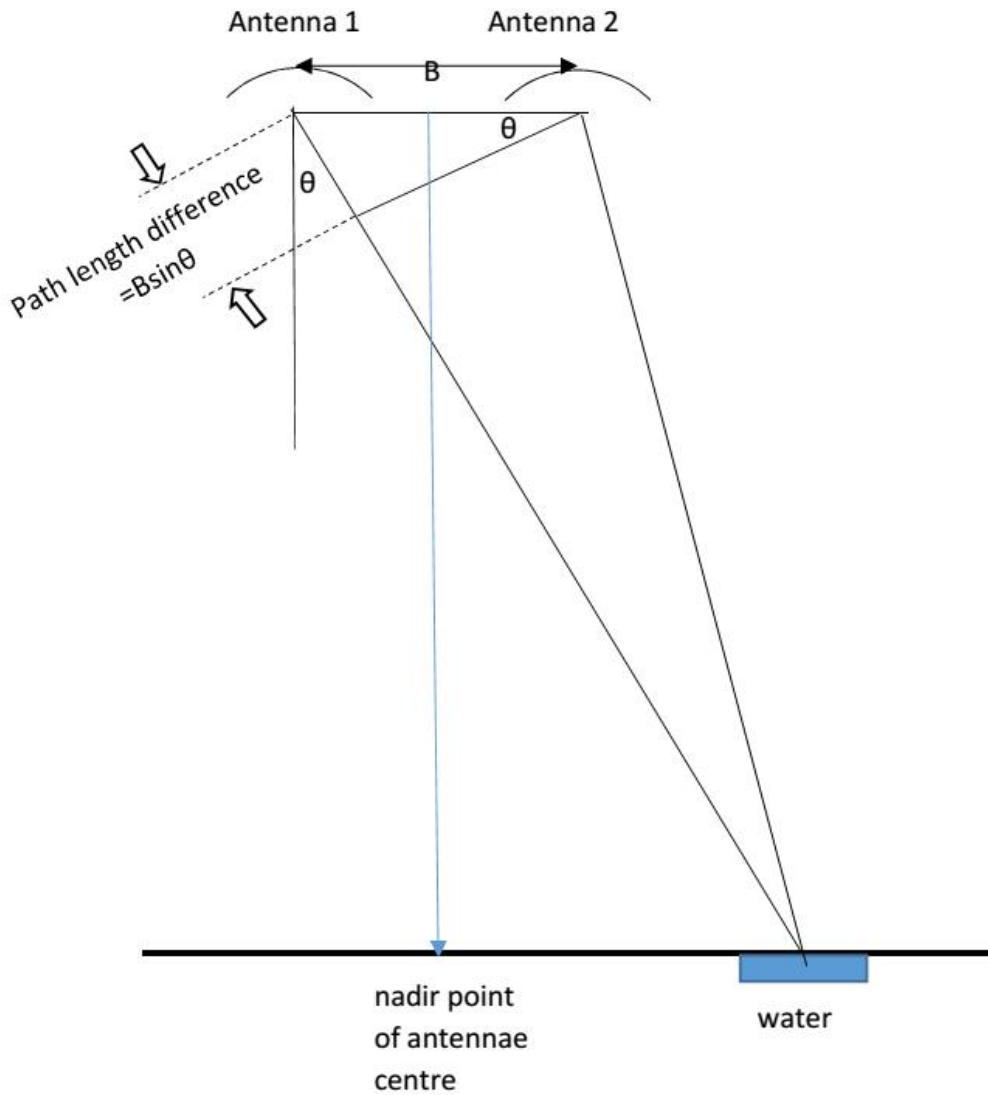


Figure 4: Schematic of water reflectors in SARin waveforms. The angle θ is the offset (cross angle) of the water reflectors from the nadir direction. B is the baseline between the two antennae

		ESA Contract:	1/6287/11/I-NB
		Doc. Title	D4200 Product Validation
		Doc. No	Report NCL_CRUCIAL_D4200
		Version No	3
		Date	30.08.17

3 FBR Product and Validation

The multi-look processor of D4100 estimates heights from the empirical retracker and OCOG/Threshold (threshold=0.75). The value of the threshold was chosen to give comparability between the heights from OCOG and the empirical retracker. In terms of the retracking the OCOG retracker with threshold = 0.75 has proved to be as precise as the empirical trackers employed. Heights from FBR SAR and SARin data are validated by comparison against in situ data from gauges where possible or against heights derived from the contemporaneous altimeter mission OSTM (Jason-2). In addition, the statistical analysis across wide stretches of inland water such as a lake gives insight into the precision (internal consistency) of the methodology.

Within the context of this study a number of primary and secondary validation sites were utilized, namely:

1. Tonlé Sap river, Cambodia (SAR)
2. Mekong River (SAR)
3. Amazon (SAR)
4. Ocean off Amazon estuary (SARin)
5. Amazon (SARin)
6. Brahmaputra (SARin)

3.1 Tonlé Sap

The Tonlé Sap river in Cambodia is selected as a primary validation site for FBR SAR data. Tonlé Sap is a straightforward target as due to the expanse of water it can be considered a lake. Hydrologically, Tonlé Sap is a combined lake and river, in which the flow changes direction twice a year; the lake expanding and shrinking dramatically with the seasons. From November to May (dry season) Tonlé Sap drains into the Mekong River at Phnom Penh while after heavy rains (start June) Tonlé Sap backs up to form a lake. The geography of the Mekong Basin is shown in Figure 5.

Validation of Cryosat-2 heights are undertaken by comparison of OSTM heights from the USDA. In addition a gauge is sited at Prek Kdam about 100 km chainage from the OSTM Tonlé Sap ground track with data available from the Mekong River Commission. A further gauge is located at Kompong Luong, data is not available for the time period of Cryosat-2, but only for OSTM (Jason-2). Figure 6 shows the location of the Cryosat-2 heights, the OSTM repeat pass location across

		ESA Contract:	1/6287/11/I-NB
		Doc. Title	D4200 Product Validation
		Doc. No	Report NCL_CRUCIAL_D4200
		Version No	3
		Date	30.08.17

Tonlé Sap with the location of the gauge at the bridge at Prek Kdam and at Kompong Luong which is close to a floating village. The cross-section of Tonlé Sap at Prek Kdam in Figure 7 shows that the river appears to stay within its bank except possibly at peak flow in October/November.

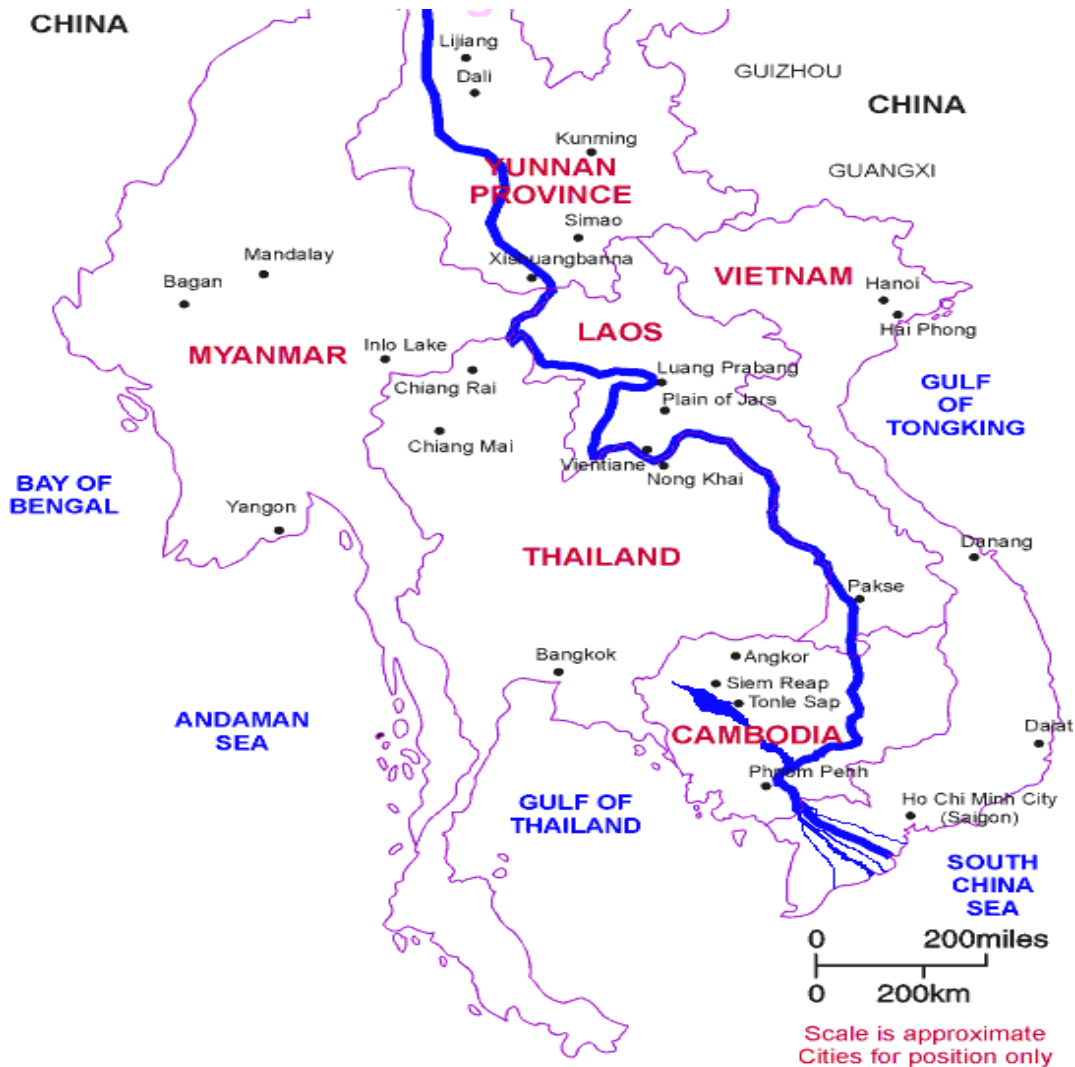


Figure 5: Map of the Mekong River including Tonlé Sap.

Analyses in D4100 showed that multi-looking over a large number of waveforms in the stack is preferable. To illustrate this we considered the pass on 3 Dec 2011 across Tonlé Sap. A total of 68 Cryosat-2 ground points (Figure 8) were identified as over the lake based on the waveform shape

		ESA Contract:	1/6287/11/I-NB
		Doc. Title	D4200 Product Validation
		Doc. No	Report NCL_CRUCIAL_D4200
		Version No	3
		Date	30.08.17

(i.e. corresponded to shape of a typically single peak empirical waveform). The stack was formed for values of N= 110, 90, 70, 40, 20 and 10 beams. Figure 9 shows the orthometric heights relative to EGM96 derived using the empirical retracker and the OCOG/Threshold retracker (threshold =0.75) for the pass. The heights for the selected N show systematic offsets from each other due to the differing slope of the leading edge. This can be seen in the waveforms (Hamming weighting) for points with time = 18647.03 – 18647.26 s in Figure 10, for N=110, 40 and 10. As N increases the weighted average of the waveform power decreases particularly at the leading edge. Since the empirical trackers identify the height from the bin at the mid-point of the leading edge for the empirical retracker and at a threshold of 0.75 for the OCOG/Threshold retracker the derived point moves towards a lower bin value as N increases. In consequence, the observed range is smaller with N=110 giving a larger orthometric or geoid height (Figure 9). This is an artefact of the stacking and weighting procedure and is not considered important as long as a consistent choice of N is used through the SAR or SARin multi-look waveform analysis. The differences between say N=110 and N=40 will appear as an altimeter bias in the orthometric height.

For each N the derived orthometric heights were fitted with a quadratic to remove any residual geoid. The residuals of the fit were taken to represent the scatter in the estimated water heights. The degree of fit is summarized in Table 1 which tabulates both the norm of the residuals as given by the 2-norm (Euclidean norm) and the standard deviation (sigma or σ). The scaled 2-norm is $\sqrt{\sum r_i^2 / df} = \sigma$ where r_i is residual of the i^{th} measurement and df is the degrees of freedom of the least-squares fit. The table shows that the minimum sum of the squares of the errors is at N = 40 and N=20 for the empirical and the OCOG/Threshold retracker, respectively. All retracker appear somewhat sensitive to N but the best fit values are near identical.

Data for this pass was additionally downloaded from ESA's G-POD Service. For comparability the 68 SARvatore waveforms closest to the corresponding CRUCIAL epochs were identified. As SARvatore uses all available waveforms in the stack to form the multi-look waveform, the G-POD waveforms and statistics are equivalent to N=123.

The two sets of waveforms had slightly different epochs due to the different choice of ground points in the two independent procedures. Figure 11, plots the waveforms for # 117, 118, 119, 120, 121 and 175. All waveforms, processed with N=123 to provide a sound comparison, have been normalised to maximum power of unity and the SARvatore waveforms adjusted in bin number to give best agreement with the other pair of waveforms. The colour scheme corresponds to Blue N=123 (Hamming window), Green N=123 (unit weight) and red (SARvatore). The last waveform #175 (lower right) is double peaked indicating multiple strong reflectors as the satellite crosses from water to land. The block of 6 waveforms shows the full bin range 0-255 while Figure 12 zooms onto the leading edge in bins 120-150. Interestingly, the use of the Hamming (cosine)

		ESA Contract:	1/6287/11/I-NB
		Doc. Title	D4200 Product Validation
		Doc. No	Report NCL_CRUCIAL_D4200
		Version No	3
		Date	30.08.17

window weighting of Eq. (1) or a unit weight for the waveforms in the stack appears to make little difference. Similarly the G-POD waveforms are in excellent agreement with the other pair although it must be remembered that the G-POD and CRUCIAL waveforms are not exactly at the same location. Figure 13 shows a normalised WF #117 (c.f. Figure 11). As in Figures 11 and 12, the waveforms have been aligned at peak (amplitude and bin) and show G-POD (equivalent to $N=120$) and $N=110, 40$. Similar to Figure 12, the earlier bin retracked point for large N causes the range to surface to decrease, i.e. the land/water height above reference ellipsoid (and hence orthometric height) to increase (Figure 9). For inland water it is the sharpness of the waveform leading edge that results in optimum height recovery while the tail is of little geophysical interest. Thus, although lower N increases the noise on the waveform tail, this is not significant.

Table 1 shows the rms residual fit to the SAMOSA2 heights after fitting a quadratic to remove residual geophysical signatures for consistency. As stated previously, for the CRUCIAL/SAMOS2 comparison the L1B data is processed with $N=123$. The G-POD SAMOSA2 values are from two sets of SARvatore values that straddle the epochs of the CRUCIAL data of Table 1. As the GPOD and CRUCIAL ground points do not coincide, but interleave each other, an exact comparison is not possible. The GPOD values with indices 64:161 are closest to the CRUCIAL ground points. The values in parenthesis utilise the GPOD heights from epochs after the CRUCIAL epochs. Differences between the G-POD SAMOSA2 values show the sensitivity of the recovered heights to the ground point locations. The table shows that the SAMOSA2 retracked heights are noisier than the CRUCIAL heights. Since the waveforms are near equivalent it would appear that this is caused by the SAMOSA2 retracker. To confirm this, the G-POD waveforms were retracked using the CRUCIAL empirical and OCOG/Threshold retrackers. As summarised in Table 1, the use of CRUCIAL empirical retracking significantly reduces the scatter in the derived heights. The inference is that the waveforms are comparable from CRUCIAL and SARvatore and it is the SAMOSA2 retracker that is the cause of the increased noise in the heights. However, further significant reduction in noise in the heights is possible through reducing the number of waveforms in the stack in the multi-look procedure. Table 1 shows that a 5 cm standard deviation is achievable giving a standard error of 6 mm for the mean value for this pass of 68 height measurements assuming independence of errors. The use of a Hamming window (cosine weighting) is clearly preferable and recommended (see Table 1).

Taking results from D4100, Table 2 gives the number of waveforms retracked with the single peak retrackers (1-3) and the dual peak retrackers (4-5) of Figure 2. The total numbers of single and dual peaks is also given. It is noted that the number of dual peaks increases as the number N decreases (Figure 10), especially for $N=10$. The multi-look waveform exhibits increasing noise in the tail as fewer looks are included. Further, the number of waveforms that were retracked best with retracker type 3 (ocean-like form) increased for $N=40$ and $N=20$. This reflects that the tail of

		ESA Contract:	1/6287/11/I-NB
		Doc. Title	D4200 Product Validation
		Doc. No	Report NCL_CRUCIAL_D4200
		Version No	3
		Date	30.08.17

the waveform has been modified by inclusion of a larger number of looks whereas the retracker of Type 2 can adapt to best-fit a high proportion of the waveforms for large N. It does not mean that the waveforms are becoming more specular but rather that the exponential decrease in the tail is better modelled by the simulated waveform. It is noted that there are no occurrences for the retracker number 1. This tracker is associated with still water and is applicable to a lake with minimal turbulence. Figure 10 also shows the weighted average of the power is lower as N increases. Thus, although more looks are included as N increases, the decreasing power in these looks reduces the overall power in the weighted multi-look waveform.

We used Table 1 and Table 2, as well as complementary results, in our decision to use N=40 as our preferred value giving multi-looks over 81 burst echoes. As the change in N causes an offset between the derived heights, which is indistinguishable from other contributions to the altimeter bias, a fixed value for N must be applied to all analyses to avoid bias.

For external validation, we plot (Figure 14) the OSTM, Cryosat-2 and Prek Kdam gauge heights when available. The time-series are aligned to provide the visual match. In practice 30 cm was added to the Cryosat-2 heights to align with OSTM. The gauge data has also been aligned at the maximum and minimum of the observed range by applying a single offset. Note that this is only approximately correct as without discharge data the relative heights between the time series is unknown. With discharge data the time of zero discharge will give zero slope along the river. Thus, the heights at the gauge and from altimetry should align. Using our arbitrary approach the Prek Kdam time series is earlier than that of OSTM and Cryosat-2. This is expected as the flow changes direction near the maximum height. A time correlation analysis by advancing the gauge data by an integral number of days was undertaken. The correlation results in Table 3 show that a time advance of 11-13 days is optimal. Utilising this advance an analysis of the differences between the gauge and altimetric heights shows that the 99 values of OSTM that overlap with the gauge data gave a RMS of 42.6 cm. For Cryosat-2 there are 26 values with RMS of 42.1 cm (see Table 4). Thus, there appears little difference between OSTM and Cryosat-2 heights for this test. It is noted that as the Cryosat-2 data is from non-repeating arcs we are reliant on the accuracy of the EGM08 geoid model to connect the ground tracks as well as the assumption that the time difference between the Cryosat-2 heights and the gauge data is the same 12 days as observed with OSTM. That this is not correct can be seen from the correlation analysis in Table 3 between the two gauges at Prek Kdam and Kumong Luong for the 8 years 2001-2009. For a location further north of the OSTM ground track such as Kumong Luong the time lapse compared to Prek Kdam is about 18.5 days. As the Cryosat-2 tracks cross Tonlé Sap in the main portion of the lake (see Figure 6) the use of 12 days is likely to be an underestimation. Further, as the lake is flowing the assumption that the lake surface is an equipotential surface is also questionable. Thus, we would cautiously infer that Cryosat-2 is performing better than OSTM across Tonlé Sap but more data is really needed to prove this inference.

		ESA Contract:	1/6287/11/I-NB
		Doc. Title	D4200 Product Validation
		Doc. No	Report NCL_CRUCIAL_D4200
		Version No	3
		Date	30.08.17

		ESA Contract:	1/6287/11/I-NB
		Doc. Title	D4200 Product Validation
		Doc. No	Report NCL_CRUCIAL_D4200
		Version No	3
		Date	30.08.17



Figure 6: Google earth image of Tonlé Sap. The locations of the 62 Cryosat-2 heights are given by the yellow circles. The location of the two gauges are indicated by turquoise markers. The position of the S-N OSTM altimetric pass is given by the red marker.

		ESA Contract:	1/6287/11/I-NB
		Doc. Title	D4200 Product Validation Report
		Doc. No	NCL_CRUCIAL_D4200
		Version No	3
		Date	30.08.17

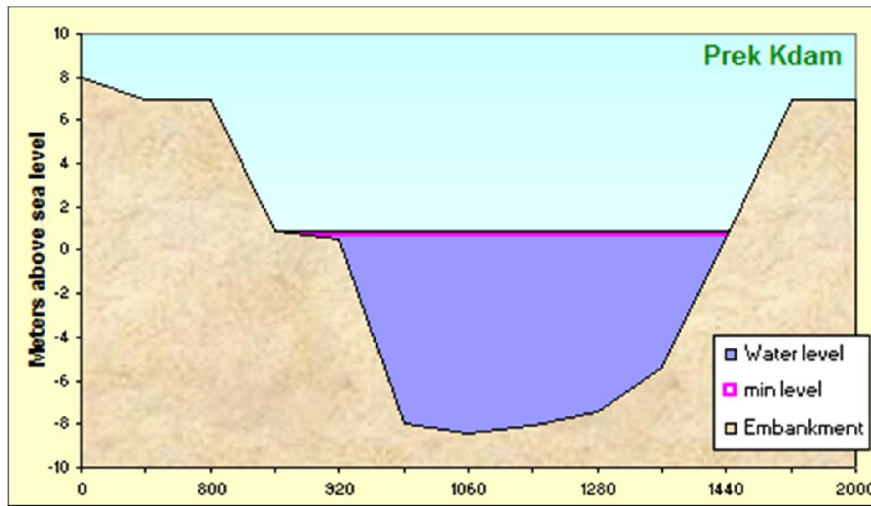


Figure 7: Cross-section of Tonlé Sap at Prek Kdam. X-axis is distance (m) across the river from point on the west embankment.

		ESA Contract:	1/6287/11/I-NB
		Doc. Title	D4200 Product Validation
		Doc. No	Report NCL_CRUCIAL_D4200
		Version No	3
		Date	30.08.17



Fig 4

Figure 8: Cryosat-2 ground points across Tonlé Sap (3 Dec 2011) North to South pass.

		ESA Contract:	1/6287/11/I-NB
		Doc. Title	D4200 Product Validation
		Doc. No	Report NCL_CRUCIAL_D4200
		Version No	3
		Date	30.08.17

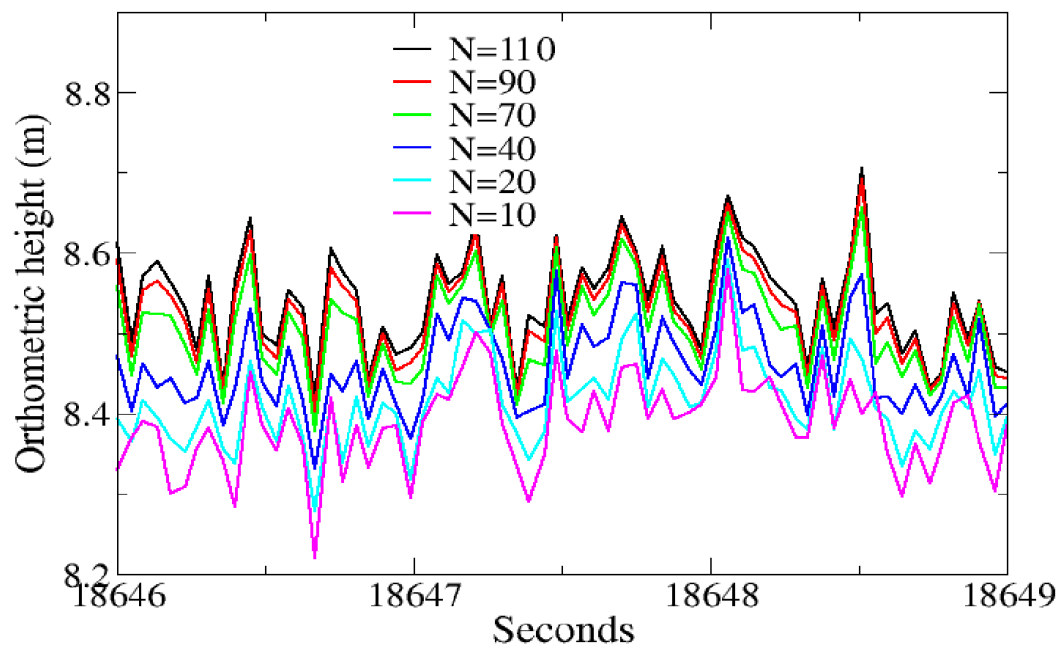
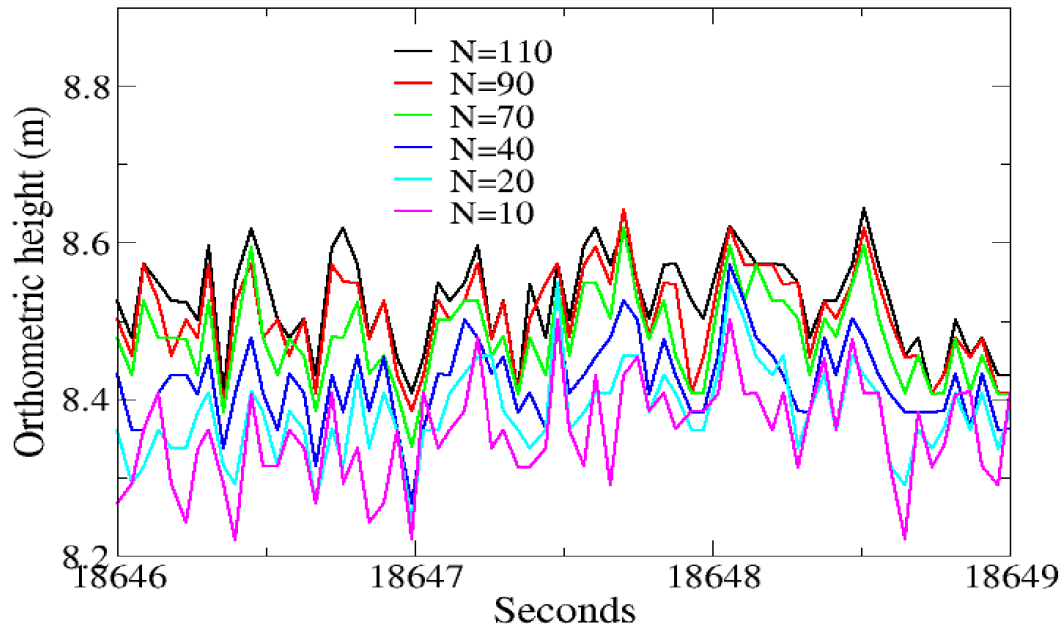


Figure 9: Geoid height measurements across Tonlé Sap (3 Dec 2011) with various multi-look combinations. Hamming window applied to waveforms. Upper: Retracked using empirical waveforms (Figure 2). Lower: OCOG/Threshold retracker used.

		ESA Contract:	1/6287/11/I-NB
		Doc. Title	D4200 Product Validation
		Doc. No	Report NCL_CRUCIAL_D4200
		Version No	3
		Date	30.08.17

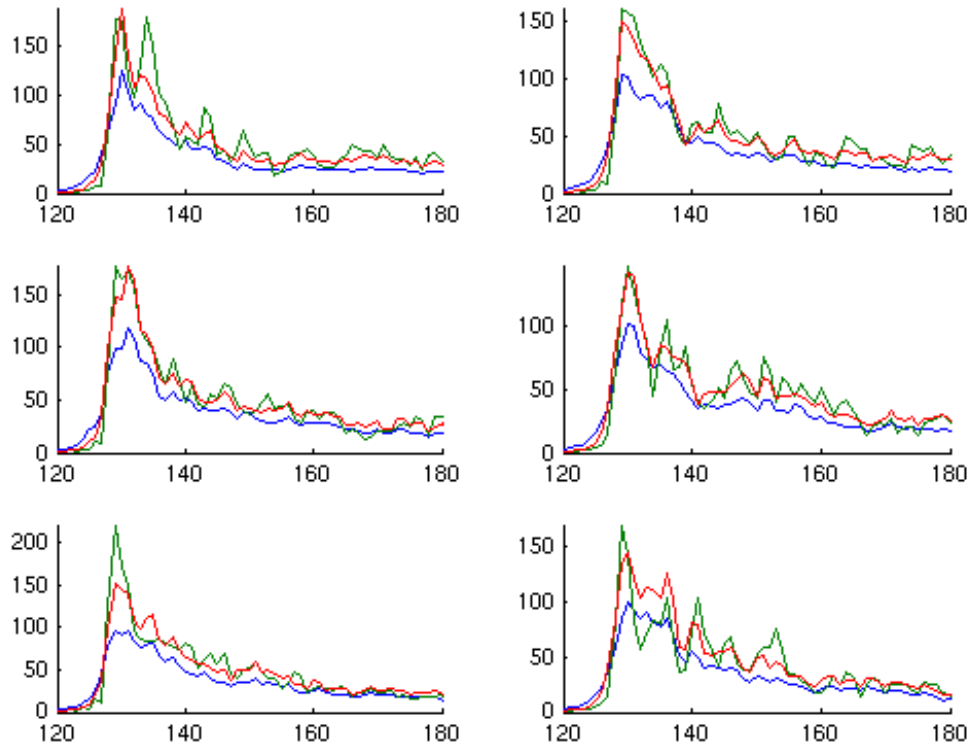


Figure 10: Multi-look waveforms (#116-121 top left – lower right) across Tonlé Sap on 3 Dec 2011 at times 18647.03-18647.26 s constructed from a stack with N=10 (green), N=40 (red), N=110 (blue) using Hamming weighting. X-axis is gate number (1-256 in SAR mode), Y-axis is power amplitude.

		ESA Contract:	1/6287/11/I-NB
		Doc. Title	D4200 Product Validation
		Doc. No	Report NCL_CRUCIAL_D4200
		Version No	3
		Date	30.08.17

Multi-look N	Norm: Empirical retrackers (cm)	Sigma (cm)	Norm: OCOg/Threshold (cm)	Sigma (cm)
G-POD: SAMOSA2 G-POD: retracked	60.96(60.18) 48.47(46.45)	7.39(7.30) 5.88(5.63)	59.20(54.40)	7.18(6.60)
120	46.91 49.60	5.69 6.01	50.61 51.38	6.14 6.23
110	47.15 49.60	5.72 6.01	50.12 51.38	6.08 6.23
90	47.39 49.60	5.75 6.01	49.53 51.38	6.01 6.23
70	46.05 48.60	5.58 5.89	47.92 52.35	5.81 6.35
40	41.33 48.40	5.01 5.87	44.34 48.49	5.38 5.88
20	42.87 48.48	5.20 5.88	41.99 46.75	5.09 5.67
10	49.01 47.35	5.94 5.74	44.10 41.51	5.35 5.03
5	75.86 62.55	9.20 7.59	63.12 57.04	7.66 6.92

Table 1: Statistics of fit for pass across Tonlé Sap. G-POD: value from (indices 94:161) closest fit to CRUCIAL ground points in time; in parentheses values from indices 95-162. CRUCIAL values: top cosine weighting; lower unit weight.

		ESA Contract:	1/6287/11/I-NB
		Doc. Title	D4200 Product Validation Report
		Doc. No	NCL_CRUCIAL_D4200
		Version No	3
		Date	30.08.17

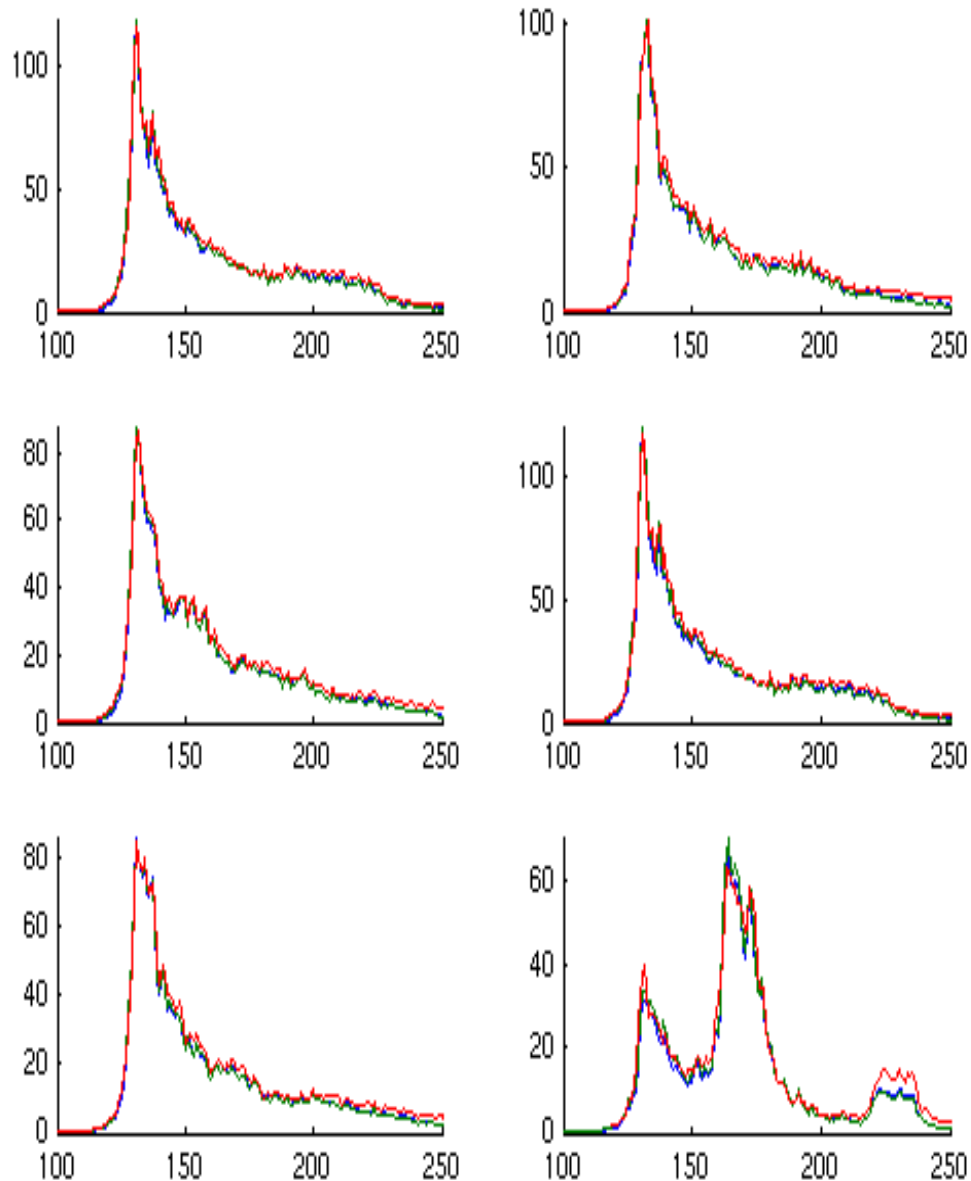


Figure 11: Waveforms (# 117-121, 175 top left to lower right) across Toulé Sap on 3 Dec 2011. N=123 with cosine weighting (blue), N=123 unit weight (green) and G-POD (red). Waveforms #117-121 over water, #175 on land near edge of Toulé Sap. X-axis is gate number (1-256 in SAR mode), Y-axis is power amplitude.

		ESA Contract:	1/6287/11/I-NB
		Doc. Title	D4200 Product Validation Report
		Doc. No	NCL_CRUCIAL_D4200
		Version No	3
		Date	30.08.17

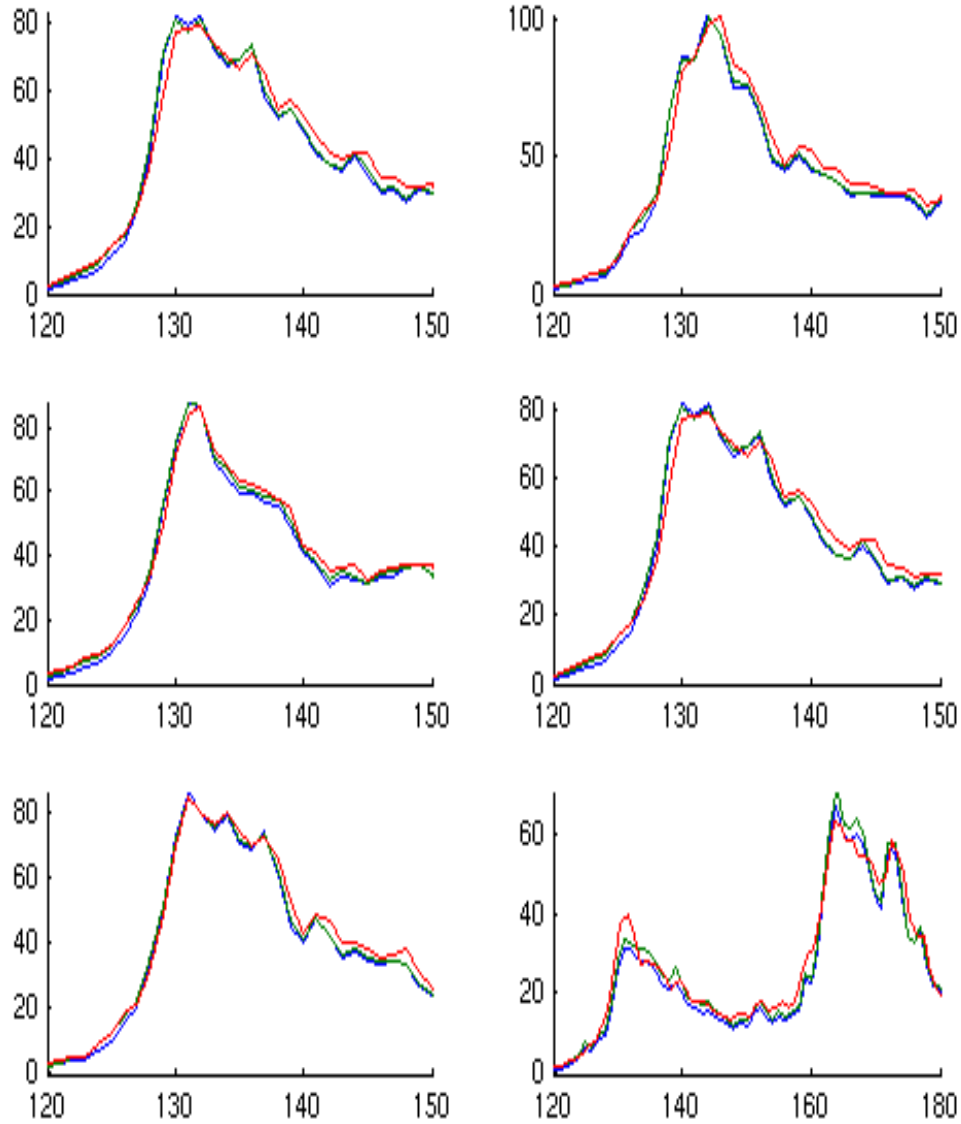


Figure 12: Waveforms (# 117-121, 175 top left to lower right) across Tonlé Sap on 3 Dec 2011. N=123 with cosine weighting (blue), N=123 unit weight (green) and G-POD (red). Zoomed version of Figure 10. X-axis is gate number (1-256 in SAR mode), Y-axis is power amplitude.

		ESA Contract:	1/6287/11/I-NB
		Doc. Title	D4200 Product Validation
		Doc. No	Report NCL_CRUCIAL_D4200
		Version No	3
		Date	30.08.17

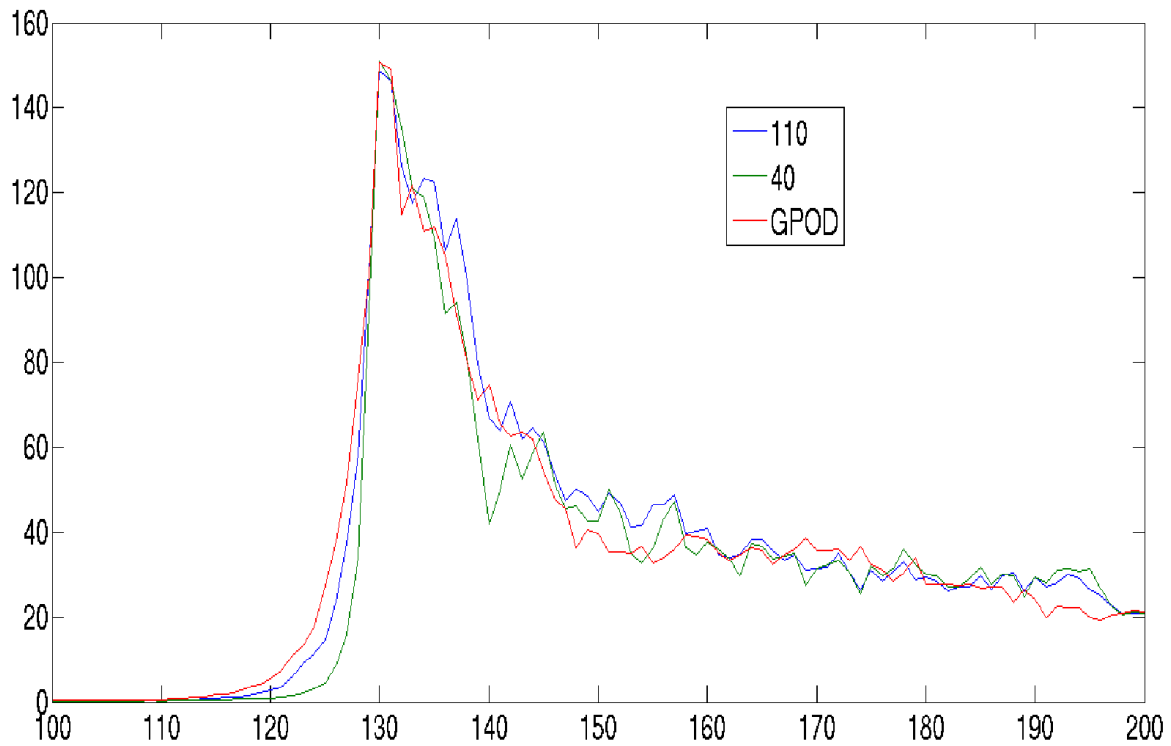


Figure 13: WF #117 across Tonlé Sap on 3 Dec 2011. Waveforms aligned at peak (amplitude and bin). G-POD (equivalent to $N=120$), and $N=110$, 40. The earlier bin retracked point for large N causes the range to surface to decrease, i.e. the land/water height above reference ellipsoid (and hence orthometric height) to increase. Lower N increases the noise on the waveform tail.

		ESA Contract:	1/6287/11/I-NB
		Doc. Title	D4200 Product Validation
		Doc. No	Report NCL_CRUCIAL_D4200
		Version No	3
		Date	30.08.17

	Empirical tracker type						
	1	2	3	4	5	Single Peak	Dual Peak
G-POD	0	29	37	2	0	66	2
N=110	0	30	37	1	0	67	1
N=90	0	26	40	2	0	66	2
N=70	0	18	49	1	0	67	1
N=40	0	5	57	3	3	62	6
N=20	0	5	57	3	3	62	6
N=10	0	8	34	11	15	42	26

Table 2: Tracker types (see D4100) for the Tonlé Sap points. The single peak column is the sum of columns 1-3 and the dual peak column that of 4-5. A total of 68 waveforms were retracked.

		ESA Contract:	1/6287/11/I-NB
		Doc. Title	D4200 Product Validation
		Doc. No	Report NCL_CRUCIAL_D4200
		Version No	3
		Date	30.08.17

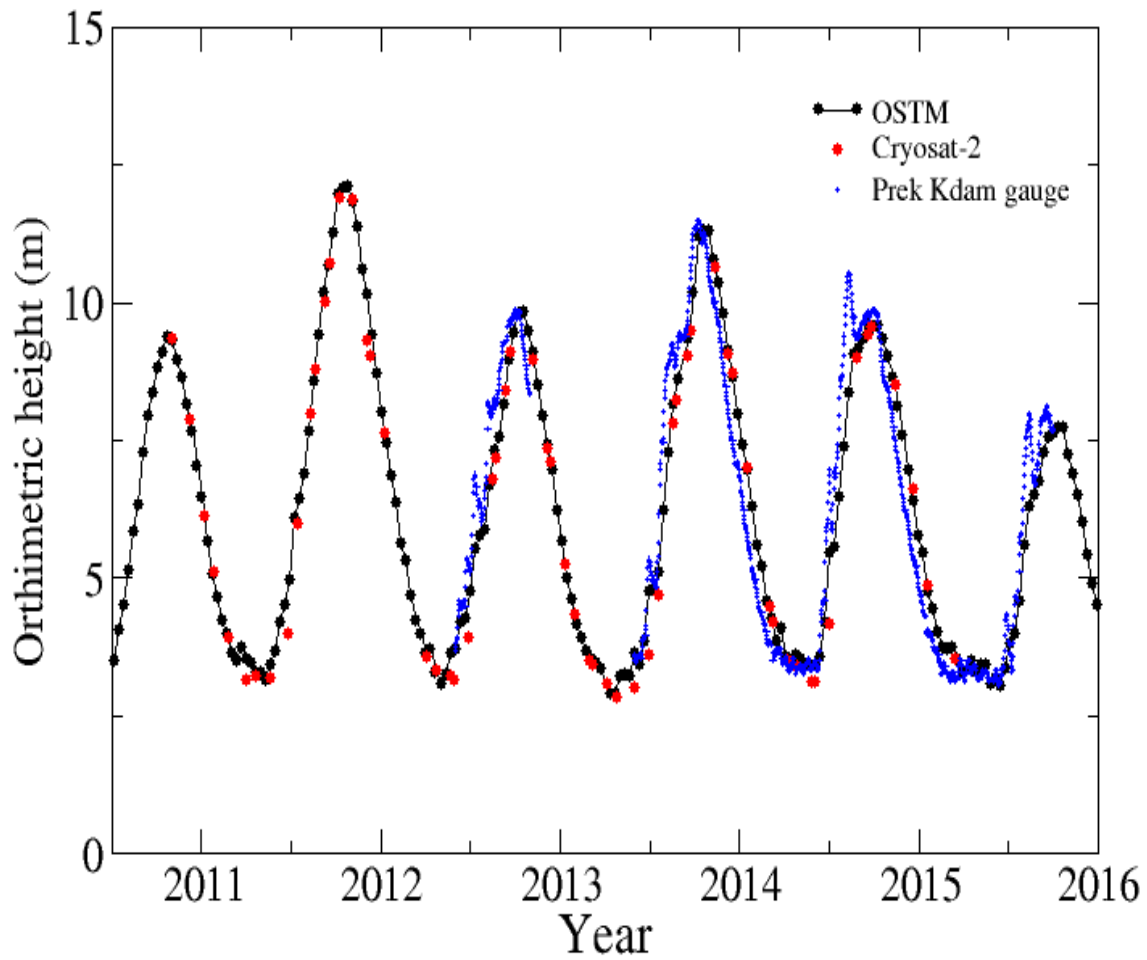


Figure 14: Time series of aligned heights across Tonlé Sap. OSTM black points, Cryosat-2 red and Prek Kdam gauge heights blue points.

		ESA Contract:	1/6287/11/I-NB
		Doc. Title	D4200 Product Validation
		Doc. No	Report NCL_CRUCIAL_D4200
		Version No	3
		Date	30.08.17

Prek Kdam days advanced	Correlation OSTM	Correlation Kumong Luong
0	0.962826	0.934639
6	0.982969	0.961042
11	0.988296	0.978429
12	0.988325	0.980823
13	0.987864	0.982860
17		0.987490
18		0.987807
19		0.987806
20		0.987491

Table 3: Time difference and auto-correlations between gauge data at Prek Kdam against the Kumong Luong gauge data and OSTM altimetric heights.

Satellite	#	RMS v Prek Kdam(t+12) (cm)
OSTM	99	42.6
Cryosat-2	26	42.1

Table 4: RMS differences between gauge data at Prek Kdam advanced 12 days and OSTM and Cryosat-2 altimetric heights.

		ESA Contract:	1/6287/11/I-NB
		Doc. Title	D4200 Product Validation
		Doc. No	Report NCL_CRUCIAL_D4200
		Version No	3
		Date	30.08.17

3.2 Mekong

The Mekong River is the eighth largest in the world in discharge (ca. 475 km³ year⁻¹) and the 12th largest in length (ca. 4800 km). Cryosat-2 is in SAR mode in the Lower Mekong Basin, downstream of the Myanmar/Laos border. All FBR SAR files 16 Jul 2010 – 31 Mar 2015 have been processed using the fine resolution Mekong river mask described in D4100. As an illustration of a typical pass we consider the data set of 19 Apr 2011. Ground track points across the Mekong are shown in Figure 15 with the derived orthometric heights in Figure 16. SAMOSA2 heights from SARvatore and retracked heights from the SARvatore waveforms using the empirical retrackers are plotted in the upper and lower subplots of Figure 16, along with heights from the CRUCIAL procedure with N=110 in the upper plot and N=40 in the lower plot. The enhancement in the SARvatore heights by replacing SAMOSA2 by the empirical retrackers within the SARvatore waveform analysis is again clearly evident. N=40 gives an additional value over N=110, again confirming that a lower value of N is beneficial. It is not feasible to compare the two heights retracked from the CRUCIAL and SARvatore waveforms as ground points are offset and the solutions are sensitive to location.

Validation of Cryosat-2 heights across the Mekong has been undertaken by comparison against gauge data. Figure 17 plots the location of the five Mekong River gauges within the Cryosat-2 SAR collection area with the gauge details in Table 3. About 50 km upstream from Stung Teng, are the Khone Phapheng waterfalls. These falls, the largest in south east Asia are the main reason that the Mekong is not fully navigable into China. The falls are characterised by a series of rapids with thousands of islands stretching over about 10 km and with the highest fall of 21 m. The low water level made available by the Mekong River Commission is plotted in Figure 18. The chainage is measured from the upper boundary of the SAR recording area in the Mekong basin. The falls are seen at chainage 620 km.

		ESA Contract:	1/6287/11/I-NB
		Doc. Title	D4200 Product Validation
		Doc. No	Report NCL_CRUCIAL_D4200
		Version No	3
		Date	30.08.17

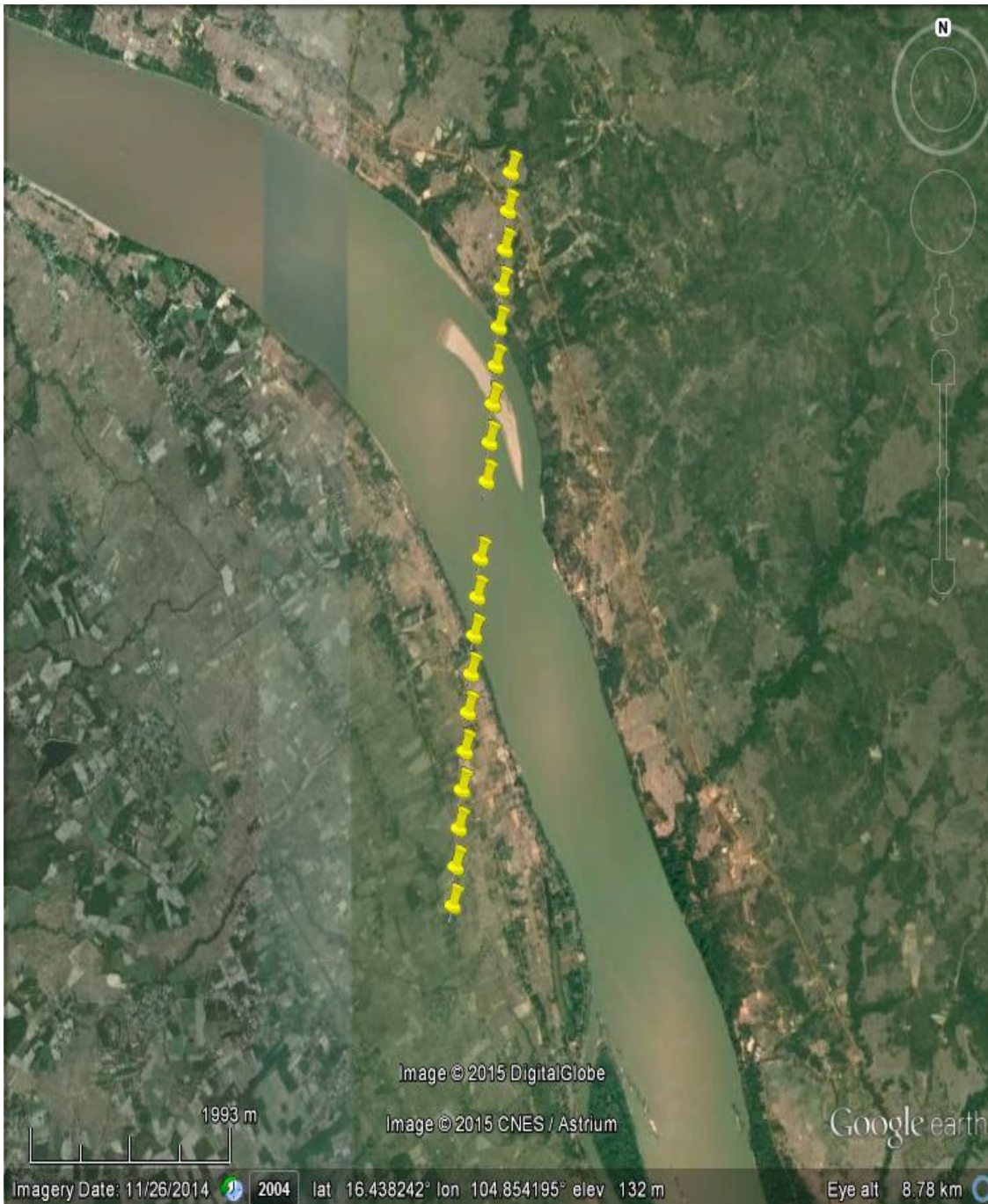


Figure 15: Google Earth image of 19 Apr 2011 Mekong crossing. Satellite ground track N-S.

		ESA Contract:	1/6287/11/I-NB
		Doc. Title	D4200 Product Validation
		Doc. No	Report NCL_CRUCIAL_D4200
		Version No	3
		Date	30.08.17

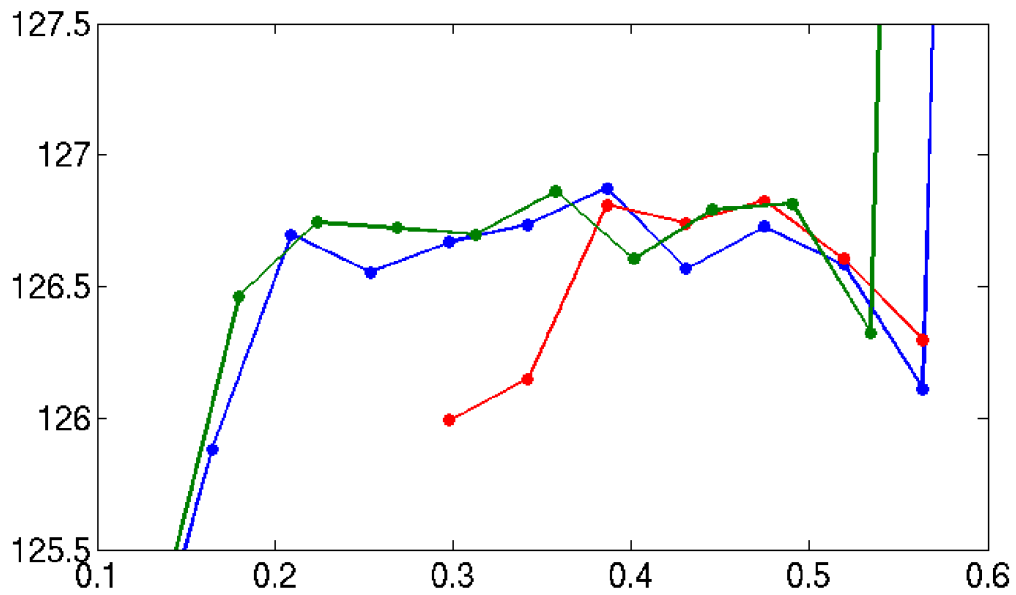
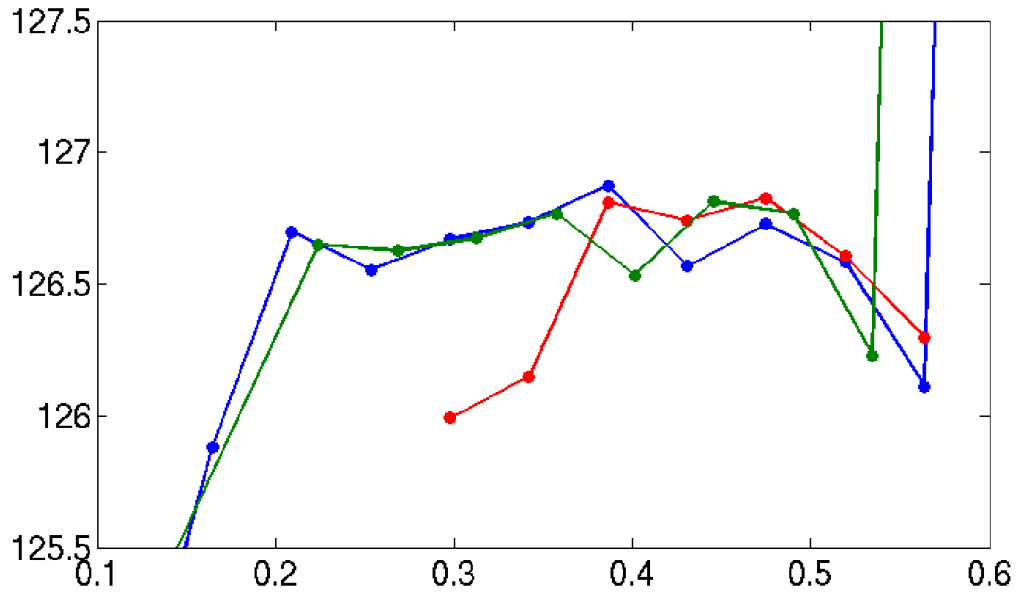


Figure 16: Estimated orthometric heights of 19 Apr 2011 Mekong crossing. In both plots G-POD heights (red) and retracked G-POD waveforms (blue). CRUCIAL cosine weighted waves (green) using $N=110$ in upper plot and $N=40$ in lower plot.

		ESA Contract:	1/6287/11/I-NB
		Doc. Title	D4200 Product Validation
		Doc. No	Report NCL_CRUCIAL_D4200
		Version No Date	3 30.08.17

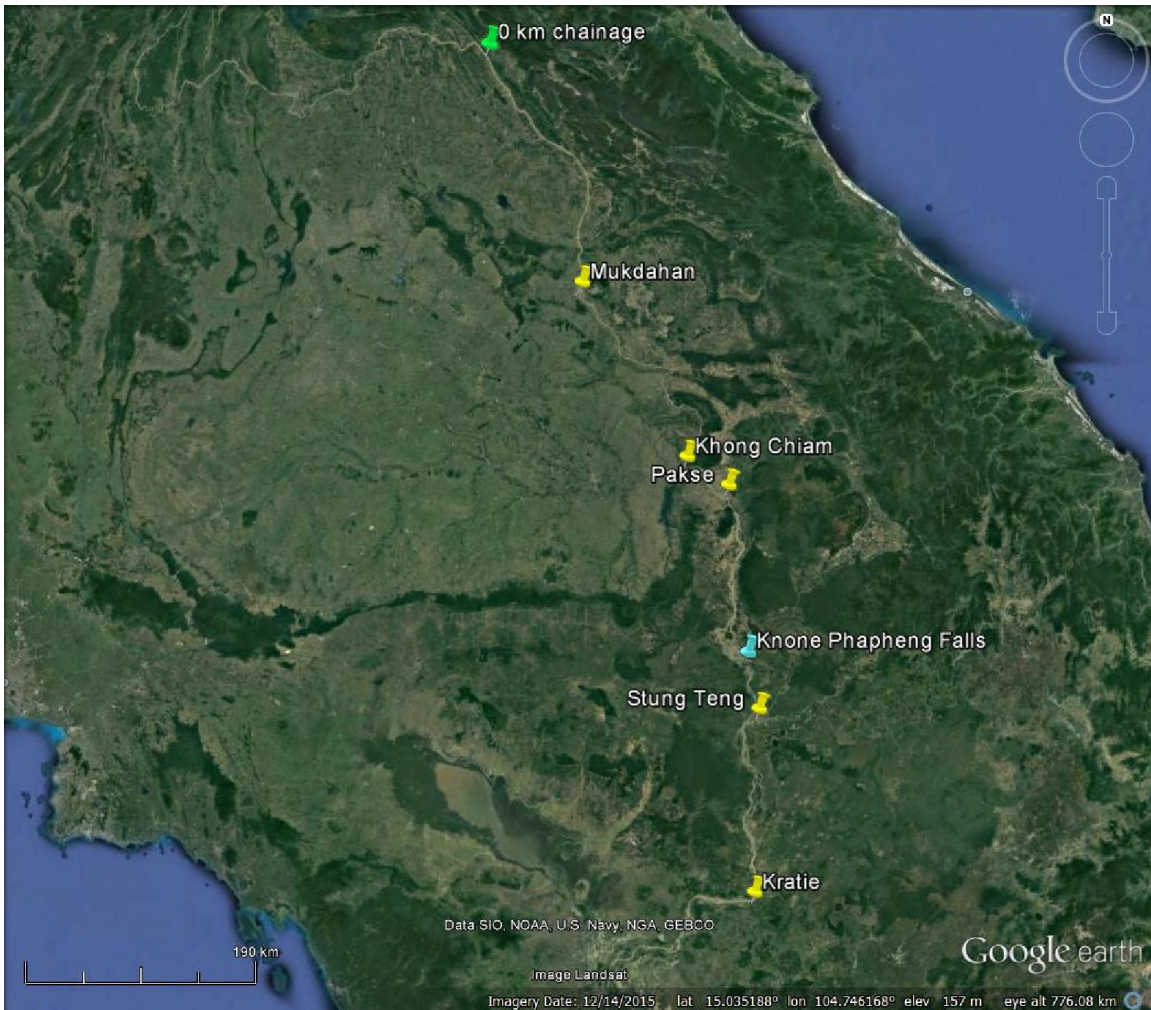


Figure 17: Location of 5 gauges along the Mekong, the Khong Phapheng Falls and the 0 km chainage point of Fig. 18.

		ESA Contract:	1/6287/11/I-NB
		Doc. Title	D4200 Product Validation
		Doc. No	Report NCL_CRUCIAL_D4200
		Version No	3
		Date	30.08.17

#	Site	Latitude (deg)	Longitude (deg)	Low water level (m)	Range (m)	Chainage of gauge (km)	Chainage range altimetry (km)
013402	Mukdahan	16.540	104.737	124.5	11	222	158-321
013801	Khong Chiam	15.318	105.500	89.8	14	433	338-441
013901	Pakse	15.117	105.800	86.8	12	473	446-615
014501	Stung Teng	13.545	106.017	38.2	9	659	650-740
014901	Kratie	12.240	105.987	2.85	16	810	741-890

Table 5: Details of the 5 gauges along the Mekong including low water level, the high water level to low water level range, chainage from the upstream point corresponding to the northern limit of the SAR mask and the chainage range for the altimeter height comparisons.

		ESA Contract:	1/6287/11/I-NB
		Doc. Title	D4200 Product Validation
		Doc. No	Report NCL_CRUCIAL_D4200
		Version No	3
		Date	30.08.17

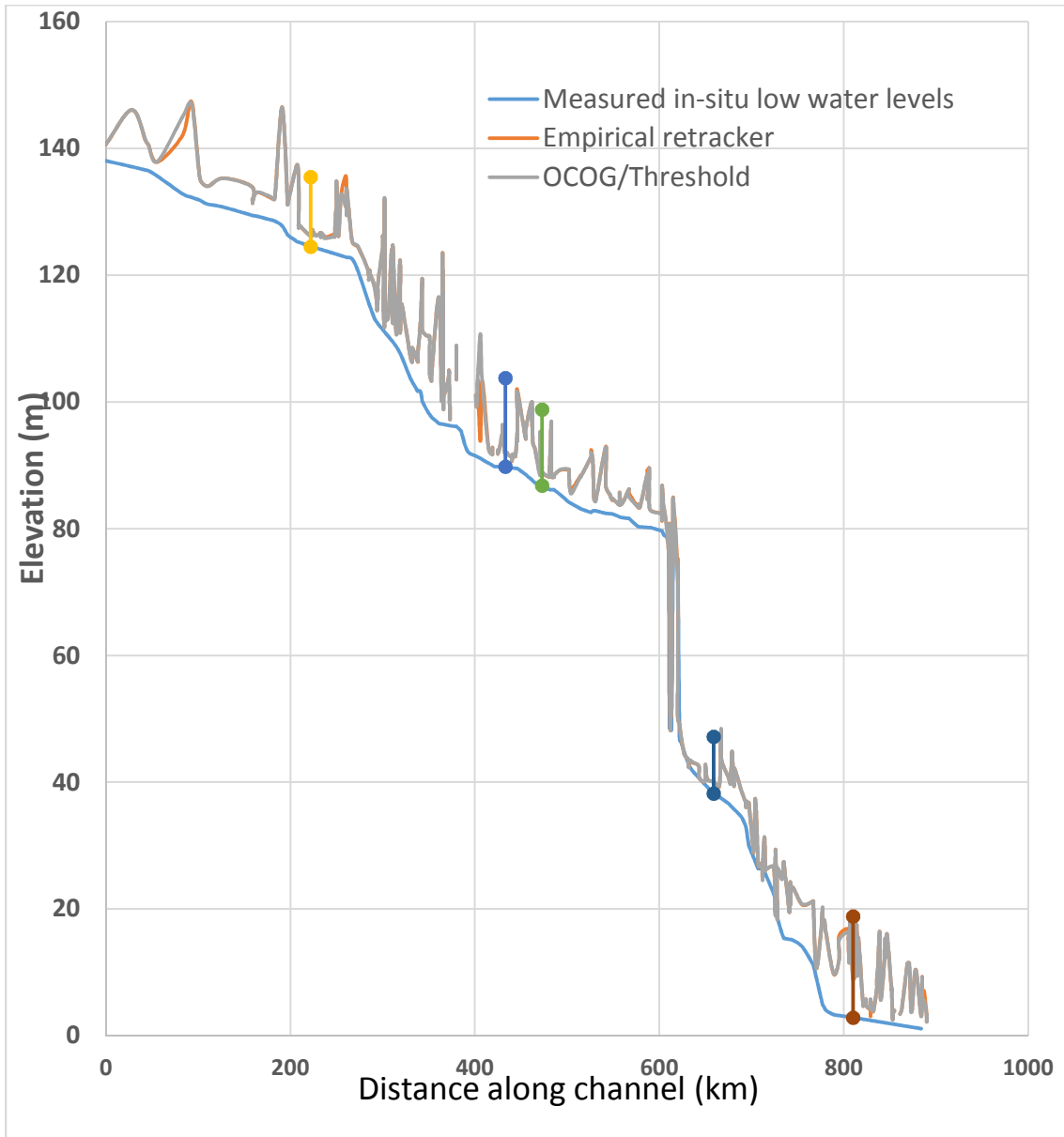


Figure 18: SAR FBR heights along the Mekong (N=40). Gauges and range identified by lines/circles. Circles at gauge show low water level (Dec-Apr) and high water level (Aug-Sep). Gauges at Mukdahan, Khong Chiam, Pakse, Stung Teng, Kratie ordered from low to high chainage. Low water level (Dec-Apr). High water level Waterfall located at chainage 620km. The 0 km chainage location corresponds to (18.23536°N, 104.0412°E).

		ESA Contract:	1/6287/11/I-NB
		Doc. Title	D4200 Product Validation
		Doc. No	Report NCL_CRUCIAL_D4200
		Version No	3
		Date	30.08.17

Figure 18 also shows the location of the 5 gauges along the Mekong with the circles denoting high (Aug-Sep) and low (Dec-Apr) flow levels. The low water levels at the gauges and the range are also given in Table 5. Table 5 also presents the chainage of each gauge from the 0 km chainage point (18.23536°N, 104.0412°E) and the chainage range for the altimeter height comparison. The zero chainage point corresponds to the northern limit of the Cryosat-2 SAR mode mask. All FBR SAR processed heights are plotted in Figure 18. Obvious outliers have been removed. Many of these are 10's of metres off the minimum level and represent unrealistic values. The outliers are identifiable without the low water level. These values are probably off ranging to water on high ground where the altimeter tracker is unable to follow the rapid change in topography from the highlands down to the river surface. This figure shows that the derived heights fall within the expected range near the gauge and also the spread of river locations that have been crossed by the satellite.

To quantify and validate the Cryosat-2 Mekong processing the heights were assigned to the nearest gauge to the Mekong crossing. The heights were subsequently corrected to the gauge location using the low water level slope. Such a correction will be less accurate at high water levels as the range is not consistent along the Mekong (Figure 18, Table 5). In addition to CRUCIAL derived heights, the Danish Technological University supplied their retracked heights based on the L1B waveforms. Figure 19 shows the heights from both DTU and NCL (empirical retracker, N=110) at Kratie. The objective here was to inter-compare the two solutions from DTU and from NCL rather than a validation against the in situ data. The RMS between the accepted DTU and NCL heights is 9.1 cm including values that are clearly off the Mekong. Both retracked data sets have similar RMS values compared with the Kratie gauge data (NCL 91.9 cm; DTU 96.8 cm).

A more comprehensive validation was undertaken using results from N=40. In this case, multiple crossings of the Mekong were eliminated and replaced by a single value. Outliers were also excluded using a 3σ criterion. An alternative would be to use the confidence bounds for the mean Mekong profile (Birkinshaw et al. 2010). A comparison of the OCOG/Threshold (RMS 66.9 cm) and empirical retracker (67.8 cm) for N=40 in Figure 20 shows a slight preference for the OCOG/Threshold retracker. These differences are comparable to those of Birkinshaw et al (2010) where an RMS of 76 cm was seen for ERS-2 for the years 1995-2003 and 57 cm for Envisat for the years 2002-2008. Differences between Cryosat-2 and the gauge are larger than those of Envisat. One explanation for this is the large distribution of chainage between the Mekong crossings and the gauge of ± 100 km. The associated slope and differences in apparent range along this stretch is evident in Figure 18. That Cryosat-2 performs almost as well as the repeat pass data of Envisat is highly encouraging.

Plots of the CRUCIAL Cyrosat-2 heights (N=40) derived from the empirical and OCOG/Threshold retracker for the other 4 gauges are plotted as Figure 21-24. Given the reduced number of data

		ESA Contract:	1/6287/11/I-NB
		Doc. Title	D4200 Product Validation
		Doc. No	Report NCL_CRUCIAL_D4200
		Version No	3
		Date	30.08.17

points no statistical analyses has been attempted and all data points have been plotted. Qualitatively, the Cryosat-2 heights are in better agreement at low to medium water levels perhaps due to the more accurate correction for slope.

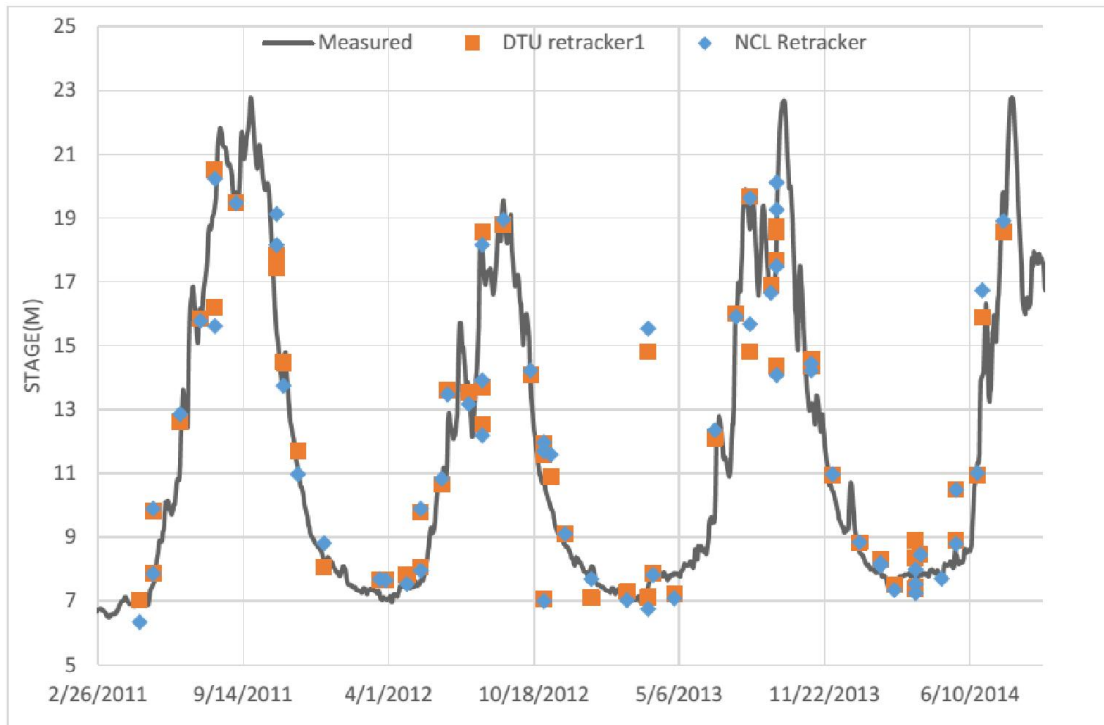


Figure 19: Comparison of Kratie gauge data with heights from near-by altimetric points from NCL (this study; N=110) and DTU. RMS 91.9 cm (NCL, empirical retracker) and 96.8 cm (DTU).

		ESA Contract:	1/6287/11/I-NB
		Doc. Title	D4200 Product Validation
		Doc. No	Report NCL_CRUCIAL_D4200
		Version No	3
		Date	30.08.17

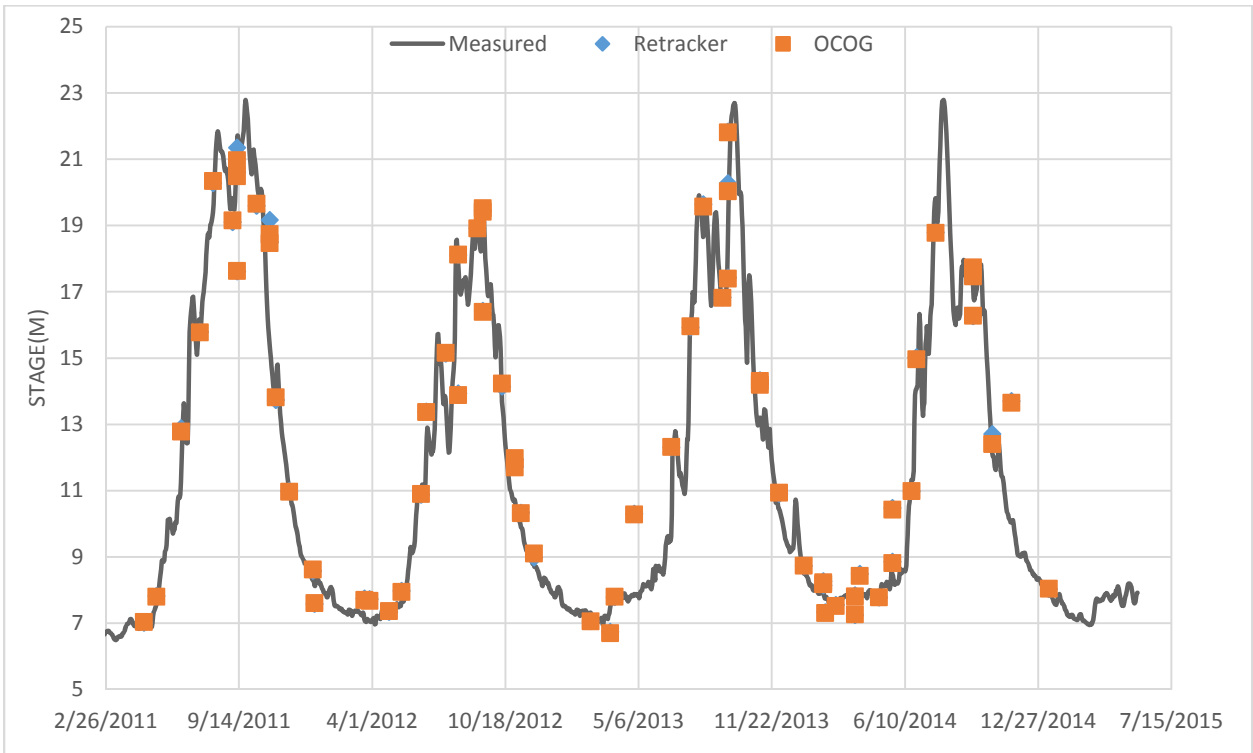


Figure 20: Comparison of Kratie gauge data with heights from near-by altimetric points from NCL (this study) waveforms using $N=40$. RMS 67.8 cm (empirical retracker) and 66.9 cm (OCO/Threshold) using 3σ rejection level.

		ESA Contract:	1/6287/11/I-NB
		Doc. Title	D4200 Product Validation
		Doc. No	Report NCL_CRUCIAL_D4200
		Version No	3
		Date	30.08.17

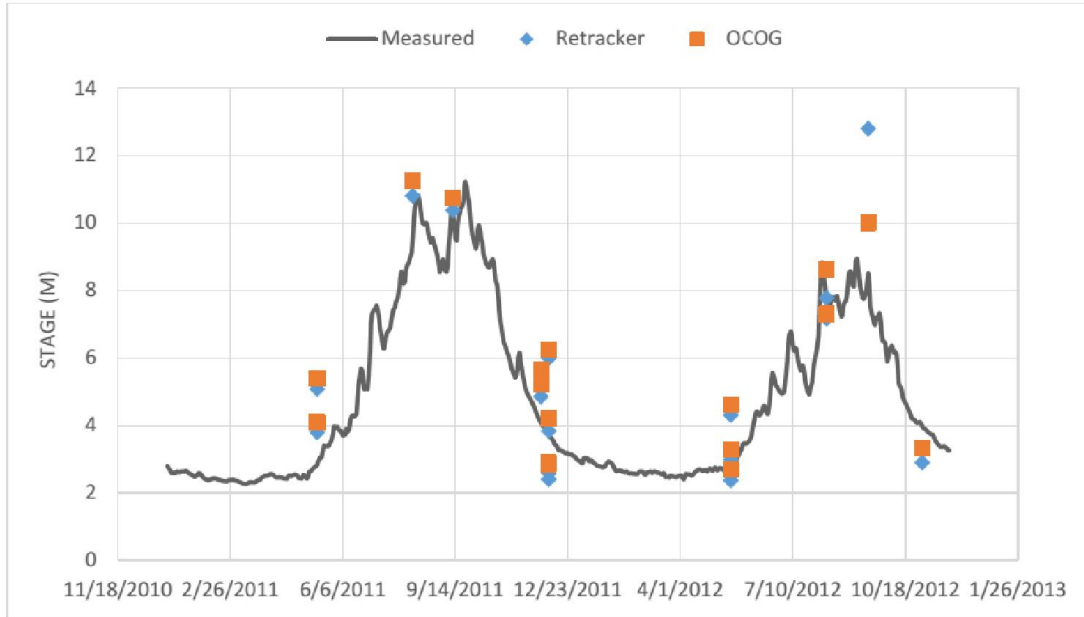


Figure 21: As Figure 20 but for gauge at Stung Teng. All data included, no rejection criterion has been applied.

		ESA Contract:	1/6287/11/I-NB
		Doc. Title	D4200 Product Validation Report
		Doc. No	NCL_CRUCIAL_D4200
		Version No	3
		Date	30.08.17

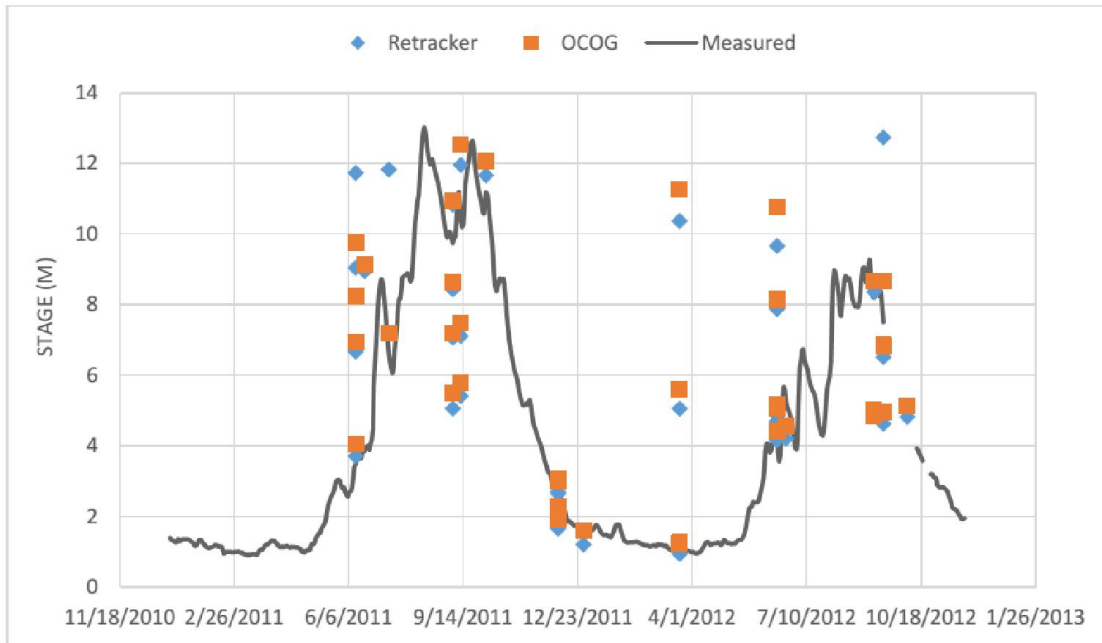


Figure 22: As Figure20 but for gauge at Pakse. All data included, no rejection criterion has been applied.

		ESA Contract:	1/6287/11/I-NB
		Doc. Title	D4200 Product Validation
		Doc. No	Report NCL_CRUCIAL_D4200
		Version No	3
		Date	30.08.17

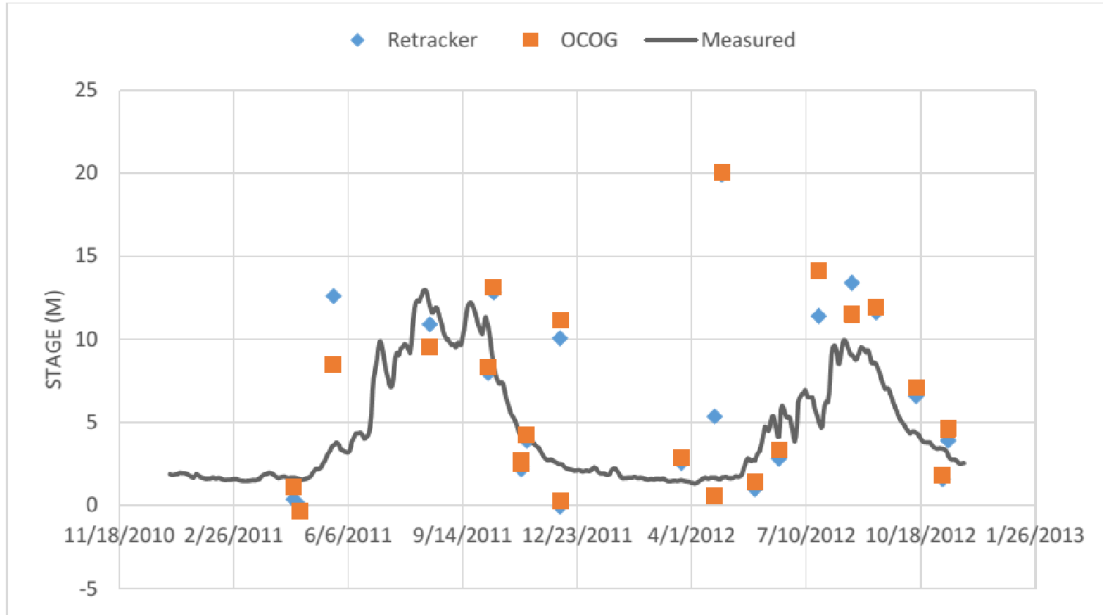


Figure 23: As Figure 20 but for gauge at Khong Chiam. All data included, no rejection criterion has been applied.

		ESA Contract:	1/6287/11/I-NB
		Doc. Title	D4200 Product Validation
		Doc. No	Report NCL_CRUCIAL_D4200
		Version No	3
		Date	30.08.17

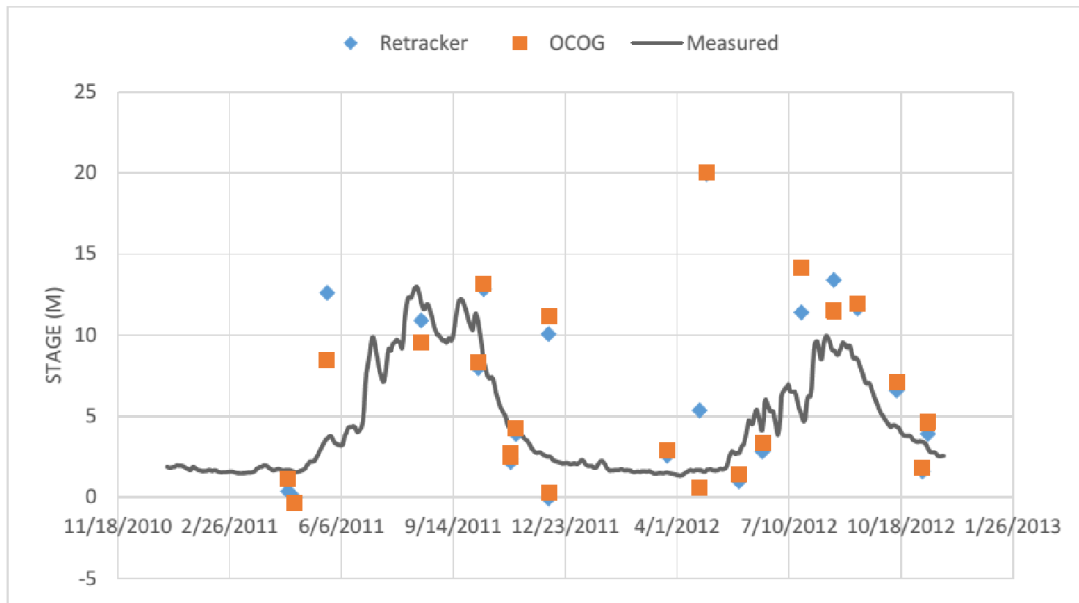


Figure 24: As Figure 20 but for gauge at Mukhadan. All data included, no rejection criterion has been applied.

3.3 Amazon

FBR SAR Level 1A data available in the Amazon basin has been compared against gauges at Obidos (1.9225°S, 55.6753°W) and Manacapuru (3.3122°S, 60.6303°W) (see Figures 25 and 26). Lines between the hinge points along the river were used to derive crossing points of the Amazon. The median height over 11 points centred on the epoch nearest to this line was derived with heights in excess of 1 m from this value rejected. Finally the mean and standard deviation of the measurements accepted were assumed to represent the actual values. The standard deviations typically were 5-20 cm. Both gauges used data over a long stretch of the river within approximately ± 45 km of the gauge. The gauge data is compared against the Cryosat-2 heights in Figures 27 and 28.

		ESA Contract:	1/6287/11/I-NB
		Doc. Title	D4200 Product Validation
		Doc. No	Report NCL_CRUCIAL_D4200
		Version No	3
		Date	30.08.17

At Obidos the 32 residuals between the gauge and Cryosat-2 gave an RMS value of 36.1 cm. The residuals were analysed against chainage using least squares to determine the river slope. The recovered slope was -0.216 ± 0.144 cm per km. The R^2 parameter for fit however was only just positive at 0.07. However, on correcting for the slope the RMS between Cryosat-2 and the Obidos gauge data was 34.9 cm. Applying a 2.5σ rejection criterion eliminated two data points but reduced the RMS to 27.3 cm.

Manacapuru is about 650 km upstream from Obidos. The RMS before allowing for the slope is 65.5 cm from 42 measurements. Adjusting for the slope of -0.429 ± 0.024 cm/km obtained by least squares yielded an RMS of 53.6 cm. Here the slope was well determined with the coefficient of determination $R^2 = 0.89$.

These RMS values can be compared against published values from Topex/Poseidon (Birkett et al., 2002), In that paper, validation exercises reveal that the time series had variable accuracies with mean ~ 1.1 m rms for 1992-1999 with the best results of 0.4–0.6 m rms from the Solimões, Amazon, Xingu and Unini rivers. Thus, the Cryosat-2 result of 53.6 cm at Manacapuru falls within the Birkett et al. (2002) best results while the Cryosat-2 result at Obidos is superior by a factor of two.

		ESA Contract:	1/6287/11/I-NB
		Doc. Title	D4200 Product Validation
		Doc. No	Report NCL_CRUCIAL_D4200
		Version No	3
		Date	30.08.17

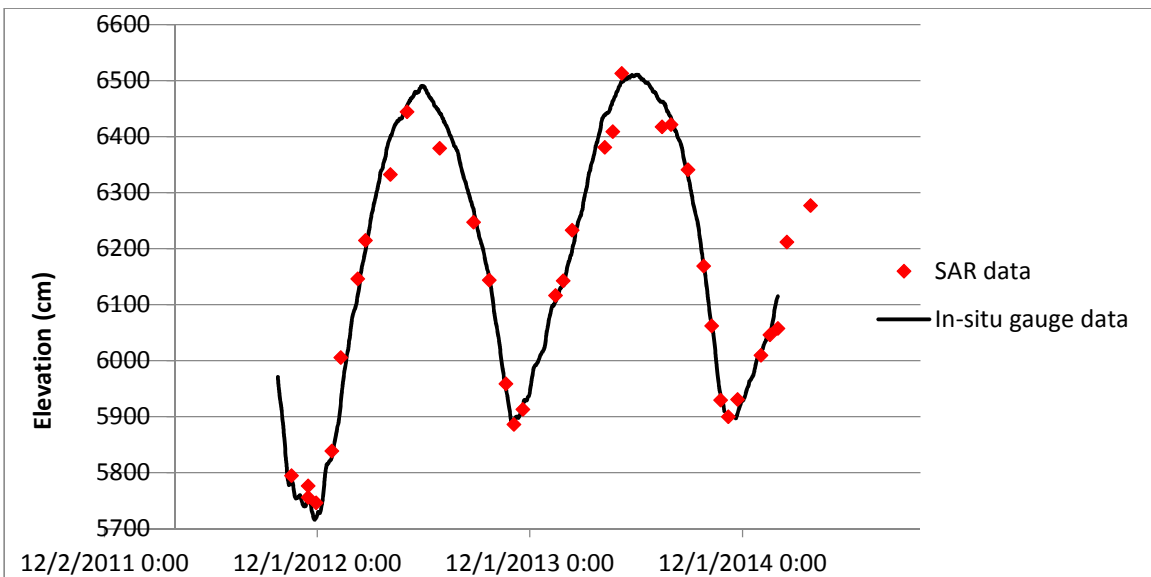


Figure 25: Google earth image of location near the Obidos gauge on the Amazon. Yellow hinge markers denote centre line of stretch considered for Cryosat-2 crossings.

		ESA Contract:	1/6287/11/I-NB
		Doc. Title	D4200 Product Validation
		Doc. No	Report NCL_CRUCIAL_D4200
		Version No	3
		Date	30.08.17



Figure 26: Google earth image of location near the Manacapuru gauge on the Amazon. Green hinge markers denote centre line of stretch considered for Cryosat-2 crossings.



		ESA Contract:	1/6287/11/I-NB
		Doc. Title	D4200 Product Validation
		Doc. No	Report NCL_CRUCIAL_D4200
		Version No	3
		Date	30.08.17

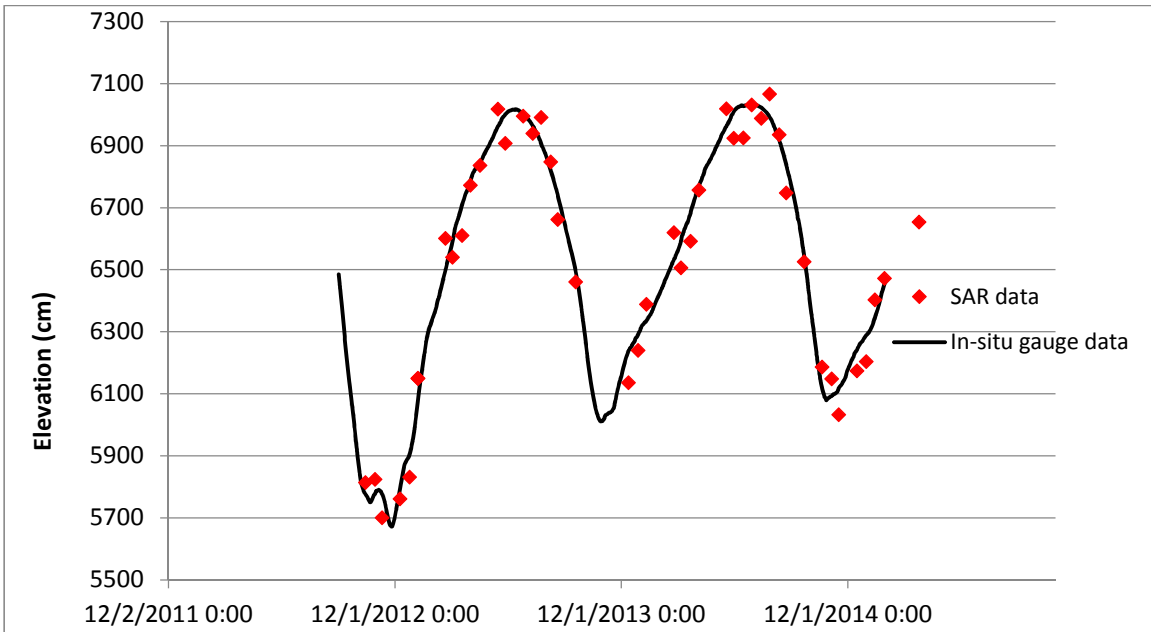


Figure 28: FBR SAR heights (N=40, empirical retracker) at Manacapuru (RMS 52.6 cm).

		ESA Contract:	1/6287/11/I-NB
		Doc. Title	D4200 Product Validation
		Doc. No	Report NCL_CRUCIAL_D4200
		Version No	3
		Date	30.08.17

4 SARin FBR Product and Validation

SARin mode was designed for regions such as polar ice margins where the ground slope can affect the point of closest approach (POCA). As the first radar return is along the direction perpendicular to the ground a sloping surface will have a POCA that is different from the nadir point. Adjustment over sloping surfaces for the POCA is necessary for correct interpretation of the waveform return and height recovery. Analysis of the waveforms from the two antennae in SARin mode assumes that the two waveforms illuminate the same surface area. If the satellite roll is accounted for, heights from the two antennae should be near identical over flat terrain and inland waters. Disparity between the measurements can then be used as a quality control with any difference identifying inconsistencies.

Use can also be made of the phase difference between the waveforms (Eq 6) and the coherence (Eq. 7) from the two antennae to investigate the cross angle. Such an approach requires least squares analyses of the weighted phase difference between the two antennae waveforms. Over inland waters reflectance is often near specular with the waveform power limited to a very small number of bins in the waveform. Outside these bins the coherence decreases as the signal to noise ratio reduces. Recovery of the ground slope from the waveform phase will also be somewhat ill-conditioned from a few bins leading to spurious results. Thus, as a compromise we used 20 bins either side of the retracked height.

4.1 Ocean

A single pass of L1A SARin FBR data over ocean (secondary site) has been analysed for internal validation of the processing methodology. The pass on 28 April 2011 is offshore of the Amazon estuary (Figure 29). The satellite passed N-S, starting over the ocean approaching land south of the Amazon estuary. The L1A FBR SARin data has been processed with data from each antennae and retracked using the empirical and OCOG/Threshold retrackers. The CRUCIAL processing utilized $N=60$ which effectively used all available waveforms in the stack to form the multi-look waveform. Data for the pass was also downloaded from the G-POD SARinvatore web site. Figure 30 plots the 20 Hz sea-surface heights (SSH_20Hz) from G-POD and the CRUCIAL heights using data from the left-hand antennae retracked using OCOG/Threshold (OCO1). The two sea-surface heights are strikingly similar with a small offset due to the different retrackers. Similarly, Figure

		ESA Contract:	1/6287/11/I-NB
		Doc. Title	D4200 Product Validation
		Doc. No	Report NCL_CRUCIAL_D4200
		Version No	3
		Date	30.08.17

31 plots the CRUCIAL analyses using the empirical retrackers but now zoomed onto the central ocean segment (800 ground points) of the pass. Again, the similarity is striking particularly the long-wavelength signatures that are almost certainly of oceanic origin. There are a few minor differences between the sets as the G-POD results are averaged over the two antennae while the CRUCIAL results pertain to a single antennae. The offset is due to the processing procedures and the retrackers used. There is a small along-track slope which is of unknown origin.

Table 6 summarises statistical analyses of the sea-surface heights for the segment containing the 800 points. The mean sea-surface (MSS) was that presented in the G-POD file. The MSS is equivalent to CLS01 (Hernandez and Schaeffer, 2001) over the ocean between 60°N and 60°S. Overall, the G-POD data agrees best with this MSS, with a standard deviation of 9.7 cm. In contrast the CRUCIAL values have standard deviations ranging from 10.7 – 14.4 cm; the best agreement in terms of sigma being through averaging the empirical retracker heights from the two antennae. Since most systematic errors in the data will cancel when the heights from the two antennae are differenced, the differences provide an insight into the scatter in the 20 Hz heights. For the OCOG retracker this gave a standard deviation of 6.7 cm, increasing to 8.6 cm on using the empirical retrackers. Assuming that the two antennae are independent these values show that the heights have precision between 4.7 and 6.1 cm for 20 Hz data. Further, assuming that the along-track measurements are independent this gives a precision of about 1.2 cm for 1 Hz data. Of course systematic errors will increase this value. The table shows that the CRUCIAL values are of comparable accuracy to G-POD. Note that the SAMOSA2 retracker is designed for ocean applications.

SARin data is designed for primary use over sloping surfaces where the POCA is off nadir. Over oceanic surfaces the POCA is expected to be in the nadir direction with an associated surface slope near zero degrees. Figure 32 shows two waveforms, their coherence and phase from locations along the ocean segment of the 800 points. These were chosen arbitrarily but other points gave similar plots. The two locations in this figure are 6 km apart. The top figures show the waveforms from the right and left antennae. There are differences over the trailing edges but the leading edges are almost exact. The middle plots show the coherence (Eq. 7). At the POCA (near bin 512) the coherence is about 0.84 for both locations. Again this is replicated in all other oceanic locations along this pass. The lower plot shows the phase difference between the complex values in the respective bins of the two antennae waveforms. The phase difference oscillates wildly in the signal noise of the first 490 bins. From bin 490 onwards the phase change is coherent. The required slope is determined from bin 490-530 on taking 20 bins either side of the tracked point. At bin 800 the phase jumps from -180° to +180°. The slope of the surface is derived from Eq. (9) having solved for χ from Eq. 8. The near constancy before the tracked point and linear afterwards is evident in the phase plots.

		ESA Contract:	1/6287/11/I-NB
		Doc. Title	D4200 Product Validation
		Doc. No	Report NCL_CRUCIAL_D4200
		Version No	3
		Date	30.08.17

Figure 33 shows the derived sea-surface slope from all ground points along the ocean pass. The satellite overflies land about latitude 0.4°N where the slope deviates rapidly from zero. Also included is a running average over 40 points to show the long-wavelength signatures. The standard deviation of points in the latitude range 0.4-3.0°S is 0.0034° with a mean of 0.0007°. Although only a single pass has been analysed there is no evidence that the mean differs from zero and hence the roll-bias utilized is correct.

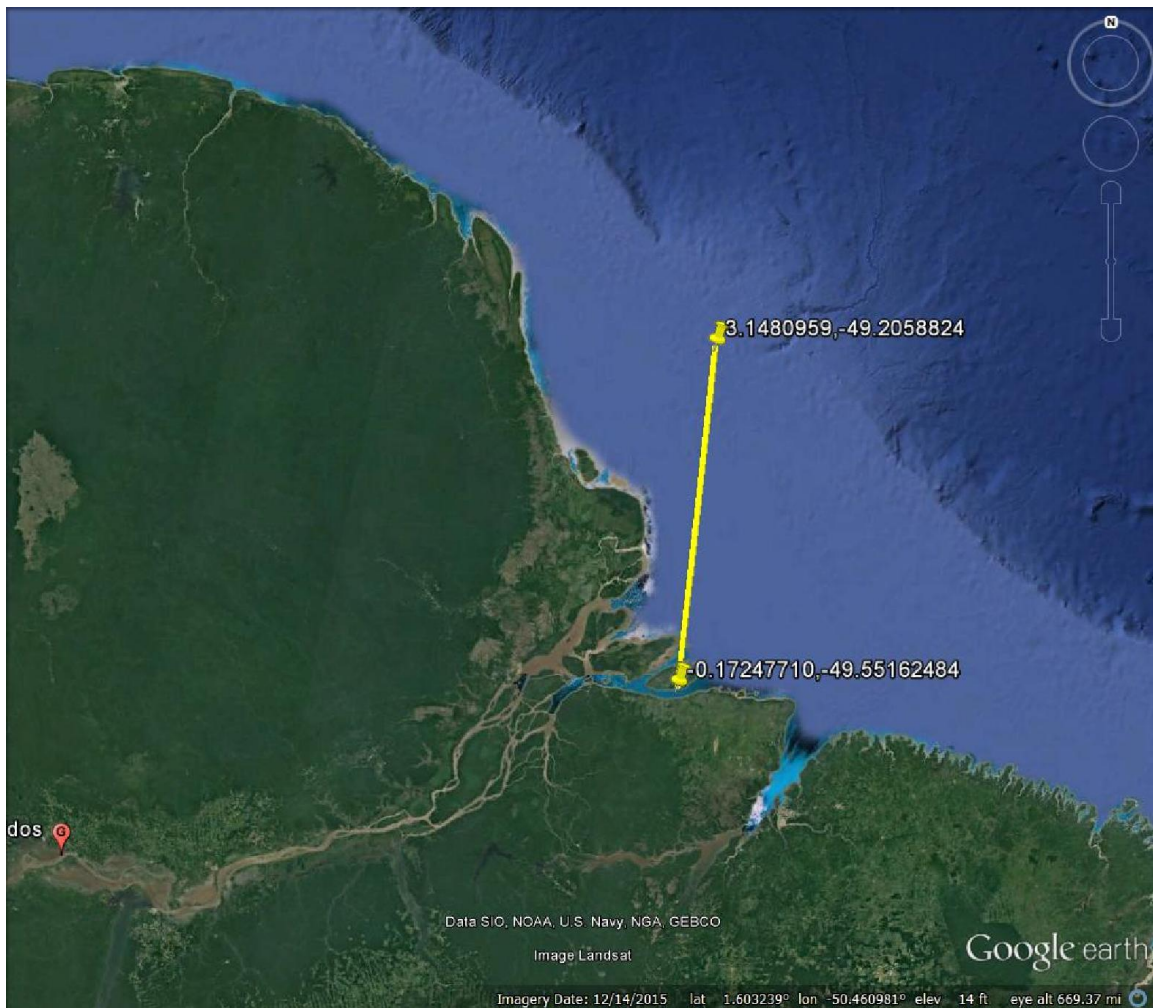


Figure 29: Cryosat-2 descending pass on 28 April 2011 off the Amazon estuary. Cryosat-2 in SARin mode.

		ESA Contract:	1/6287/11/I-NB
		Doc. Title	D4200 Product Validation
		Doc. No	Report NCL_CRUCIAL_D4200
		Version No	3
		Date	30.08.17

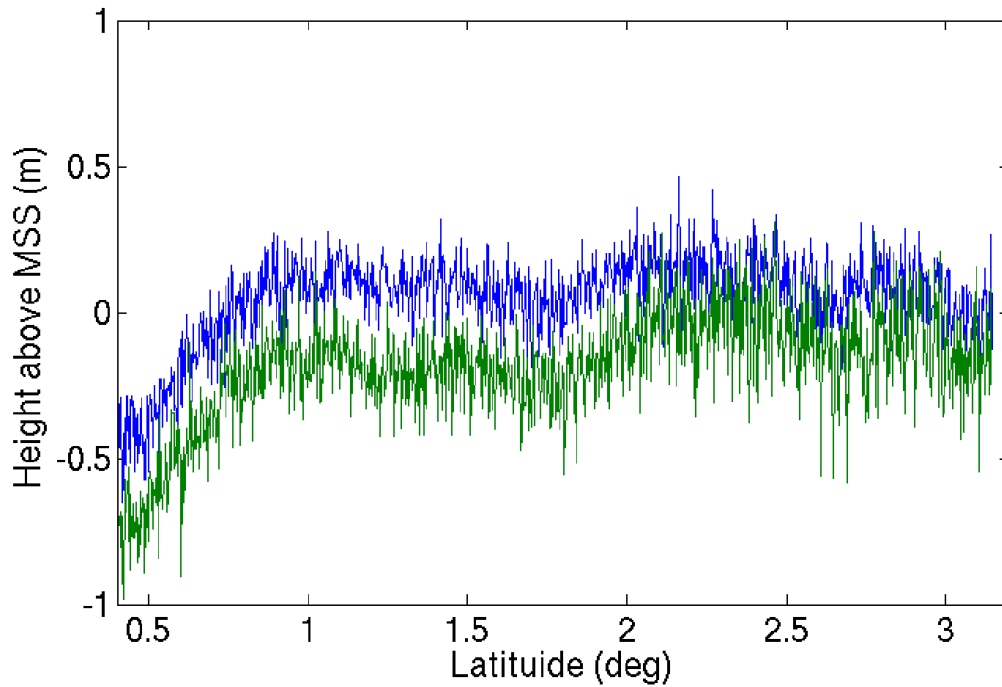


Figure 30: Sea surface heights from SARin pass on 28 April 2011. G-POD values SSH_20Hz-MSS (blue) and OCOG1-MSS (green).

		ESA Contract:	1/6287/11/I-NB
		Doc. Title	D4200 Product Validation
		Doc. No	Report NCL_CRUCIAL_D4200
		Version No	3
		Date	30.08.17

Difference v MSS	Mean (cm)	Sigma (cm)
GPOD-MSS	9.8	9.7
OCO _{G1} - MSS	-13.4	14.3
Emp1 - MSS	-12.2	11.1
OCO _{G2} - MSS	-13.8	14.4
Emp2 -MSS	-11.8	11.9
(OCO _{G1} + OCO _{G2})/2 - MSS	-13.6	13.9
(Emp1 + Emp2)/2 - MSS	-12.0	10.7
OCO _{G1} – OCO _{G2}	0.35	6.7
Emp1 – Emp2	0.39	8.6
(OCO _{G1} + OCO _{G2})/2 - GPOD	-23.0	14.9
(Emp1 + Emp2)/2 - GPOD	-21.8	11.4

Table 6: Statistics from over 800 ocean points from pass on 28 April 2100. Data covers lat. 3.01484°S – 0.083832°S. Cryosat-2 in SARin mode.

		ESA Contract:	1/6287/11/I-NB
		Doc. Title	D4200 Product Validation
		Doc. No	Report NCL_CRUCIAL_D4200
		Version No	3
		Date	30.08.17

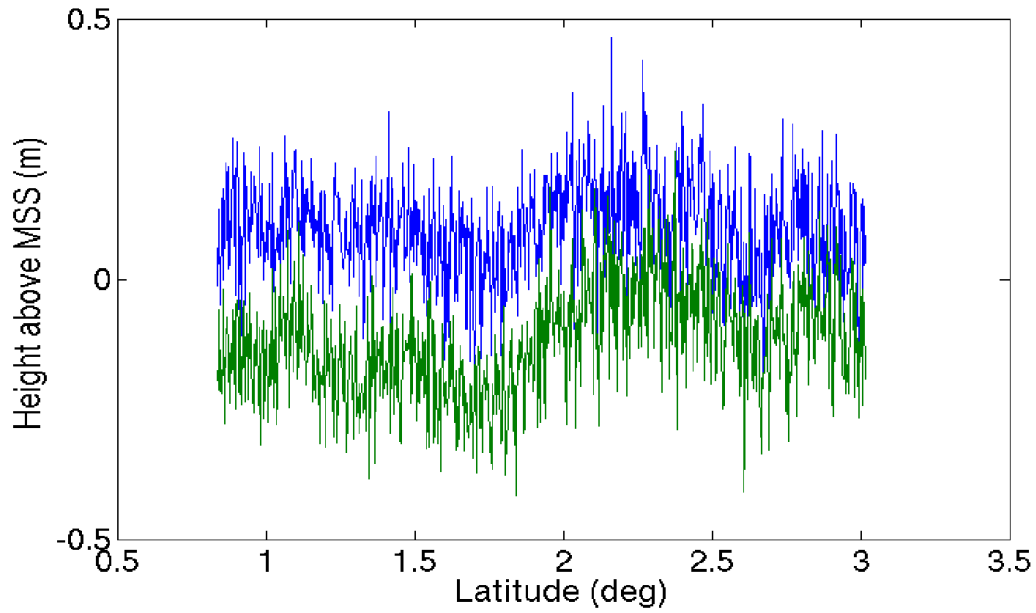


Figure 31: Sea surface heights from SARin pass on 28 April 2011. G-POD values SSH_20Hz-MSS (blue) and Emp1-MSS (green).

		ESA Contract:	1/6287/11/I-NB
		Doc. Title	D4200 Product Validation Report
		Doc. No	NCL_CRUCIAL_D4200
		Version No	3
		Date	30.08.17

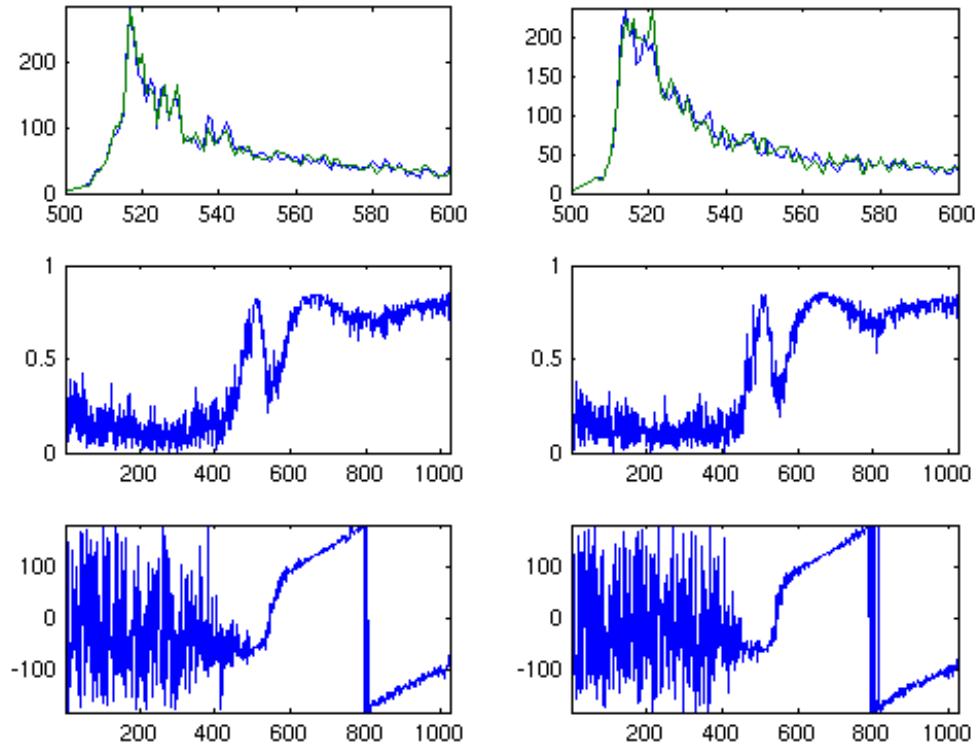


Figure 32: Top plot: multi-look waveforms (N=60) from the two Cryosat-2 antennae. Middle plot: coherence. Lower plot: phase differences between antennae over the bins (deg). Left plots for oceanic location 2.606878N, 49.262229W, right plots for oceanic location 2.062831N, 49.318856W.

		ESA Contract:	1/6287/11/I-NB
		Doc. Title	D4200 Product Validation
		Doc. No	Report NCL_CRUCIAL_D4200
		Version No	3
		Date	30.08.17

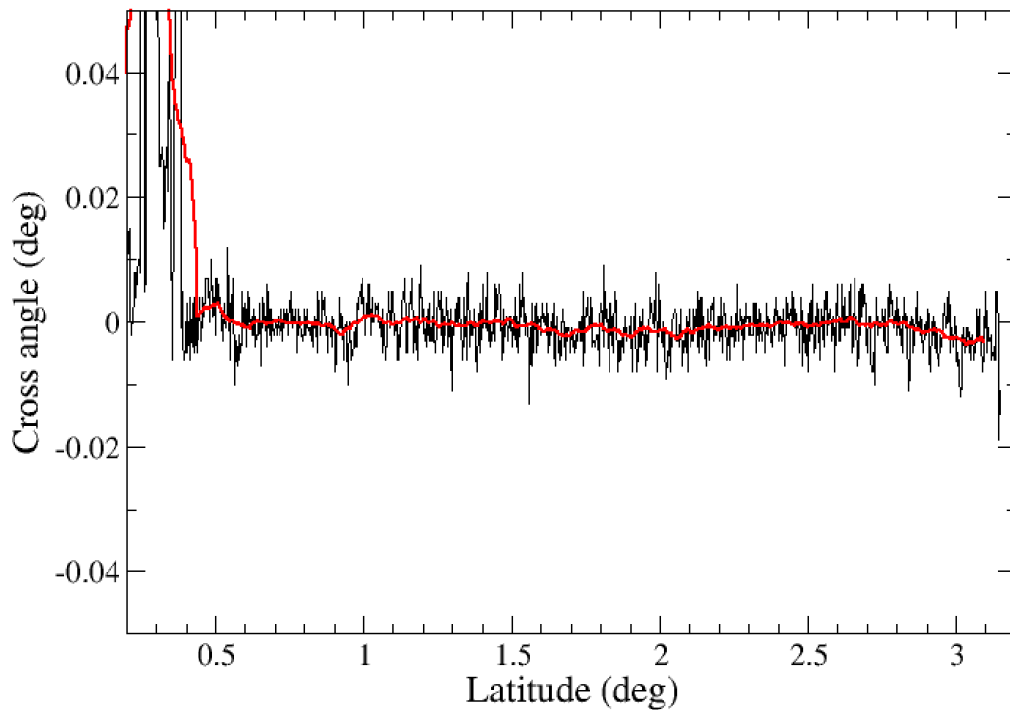


Figure 33: Derived slope from ocean pass (North to South) of 28 April 2011. Sub-satellite points hit land about latitude 0.4°N. Running average over 40 points (red curve) to show long-wavelength signatures. Standard deviation of points 0.4-3.0°S is 0.0034°, mean -0.00056°

4.2 Amazon

4.2.1 SARin Heights

As an exemplar of SARin over inland water we consider the South-North pass on 5 May 2012 across the Amazonas near the Tabatinga gauge (Figure 34). This figure shows that the Cryosat-2 ground track is close to a bifurcation of the river. The exact morphology of the river is not known at this date; Google earth image is dated 10 March 2016. Waveforms from both CRUCIAL (left-hand antennae) and from G-POD are shown as Figure 35. These waveforms correspond to the points over the Amazon in Figure 34. All waveforms have been normalized such that the maximum power is unity while the G-POD waveform bin numbers have been adjusted so that the bin of

		ESA Contract:	1/6287/11/I-NB
		Doc. Title	D4200 Product Validation
		Doc. No	Report NCL_CRUCIAL_D4200
		Version No	3
		Date	30.08.17

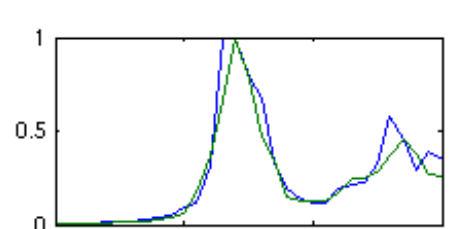
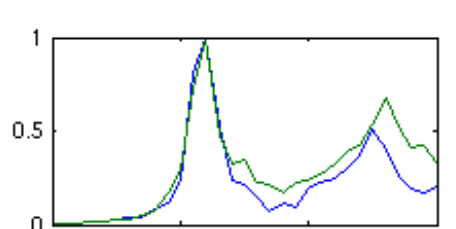
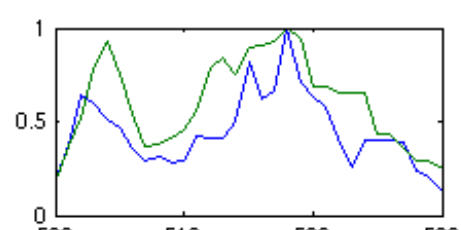
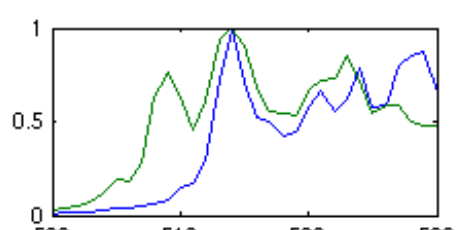
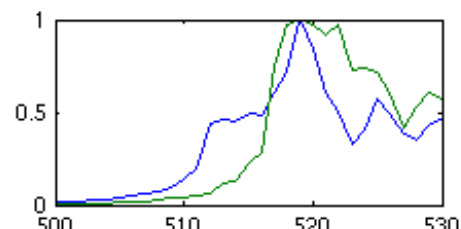
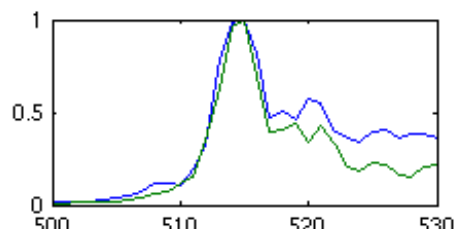
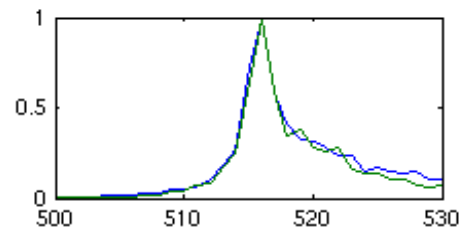
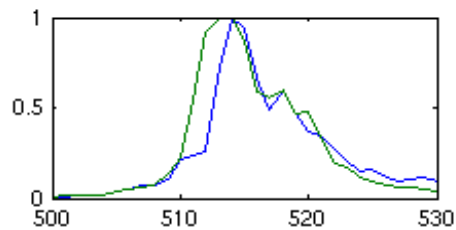
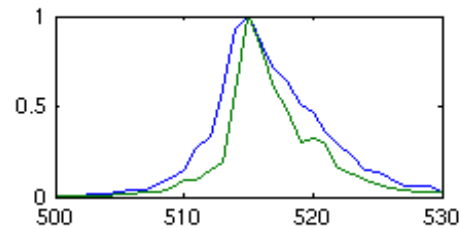
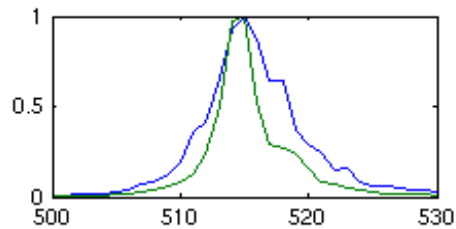
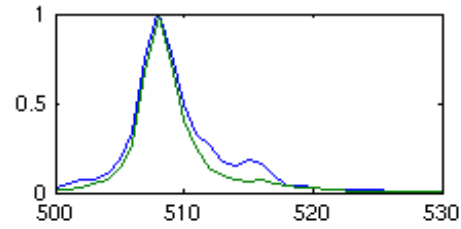
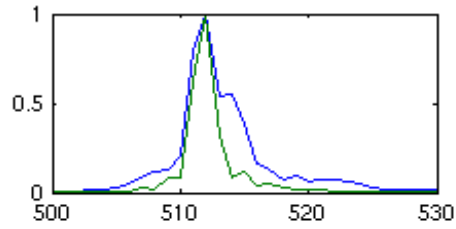
maximum power for the two waveforms now coincides. The first 6 waveforms are single peaks from water returns while the next six are more complex with multiple peaks. These are most likely when the satellite is near land with reflections from different branches of the river. The remaining 9 are also typical of inland water with a single peak. There is again close correspondence between the CRUCIAL and G-POD waveforms.

Figure 36 shows the derived heights from the SARin data. Both antennae have been considered separately with the numeral after the retracker (OCOG & Emp) denoting the right (1) and left (2) antennae. Thus Emp2 denotes the use of empirical retracker for the left-hand antenna. The figure shows that there is little difference between OCOG and the use of empirical retracker with all values similar except at the points over land centred at latitude -3.915° . In contrast the G-POD SARvatore heights reveal a larger variance. Figure 37 plots the OCOG1, Emp1 and G-POD values as in Figure 36 but also the heights from the retracked G-POD waveforms using the empirical retracker. As for the SAR data, the cause of the discrepancy is the use of the SAMOSA2 retracker rather than the waveforms which have already been proved to be similar (see Table 1).

		ESA Contract:	1/6287/11/I-NB
		Doc. Title	D4200 Product Validation
		Doc. No	Report NCL_CRUCIAL_D4200
		Version No	3
		Date	30.08.17



Figure 34: Ascending Cryosat-2 ground track across Amazonas 5 May 2012 (SARin mode)



		ESA Contract:	1/6287/11/I-NB
		Doc. Title	D4200 Product Validation
		Doc. No	Report NCL_CRUCIAL_D4200
		Version No	3
		Date	30.08.17

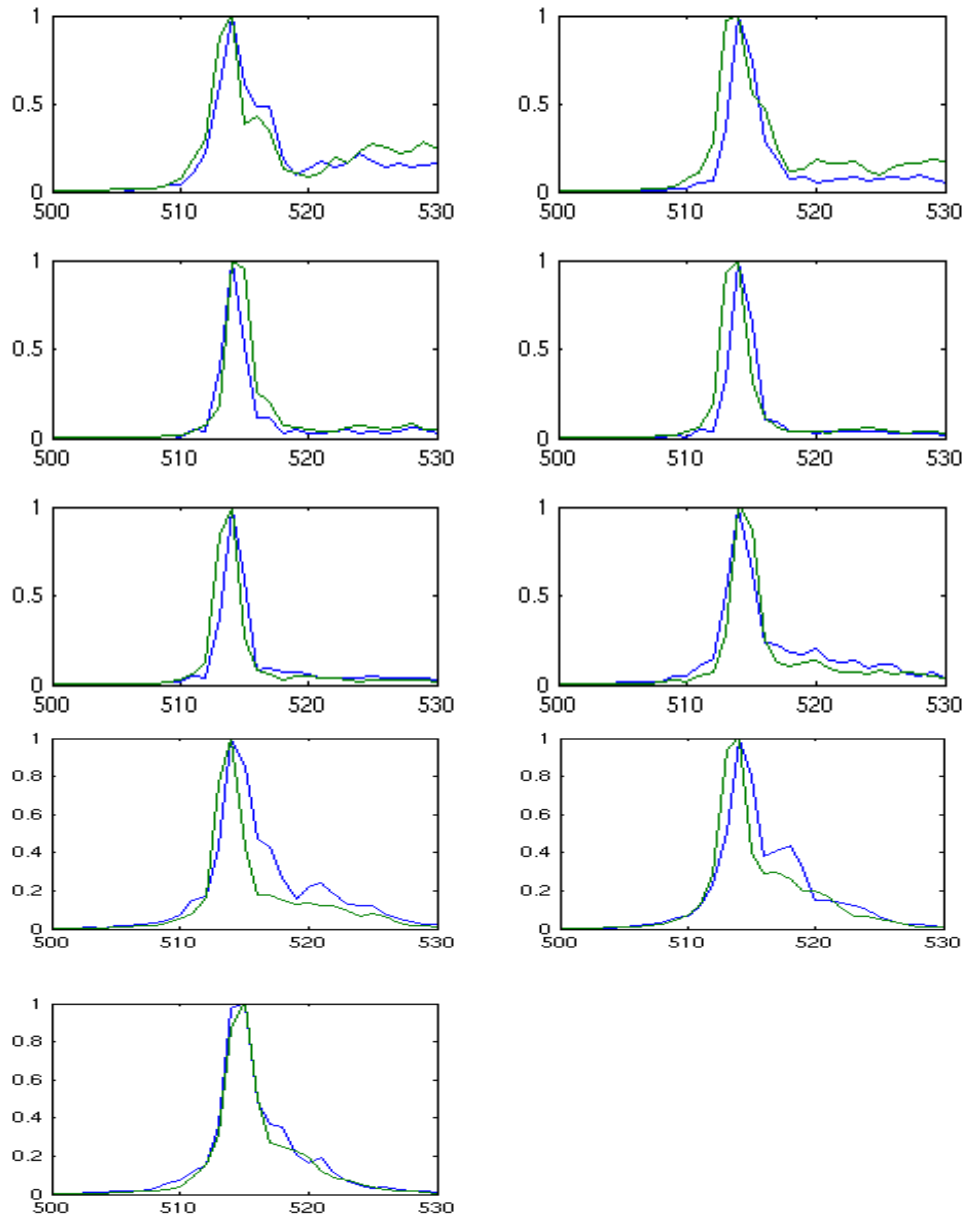


Figure 35: Multi-looked SARin waveforms across Amazon 5 May 2012. CRUCIAL waveforms N=60 (blue curves) ; G-POD SARin waveforms (green curves).

		ESA Contract:	1/6287/11/I-NB
		Doc. Title	D4200 Product Validation Report
		Doc. No	NCL_CRUCIAL_D4200
		Version No	3
		Date	30.08.17

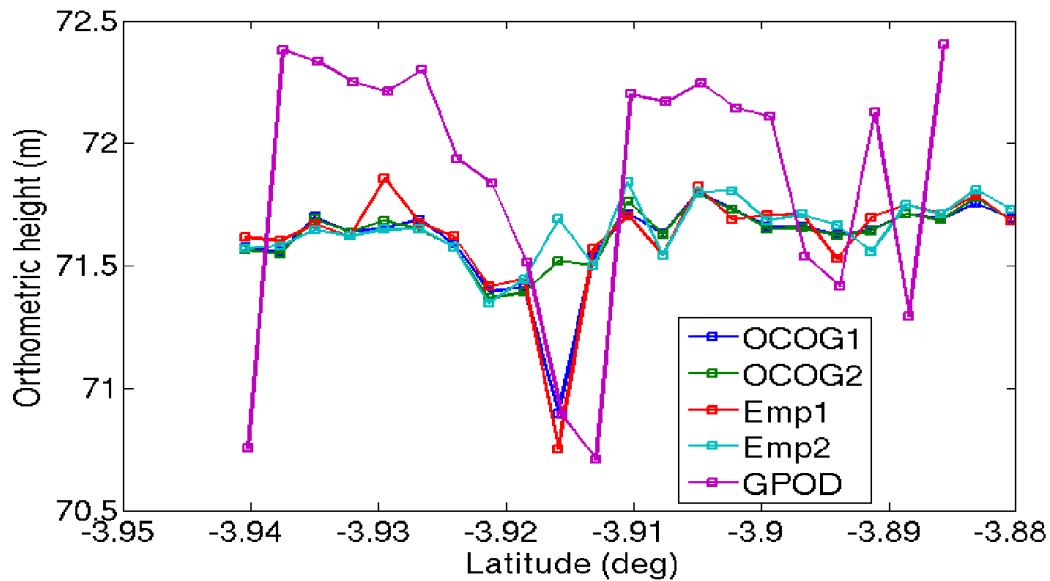


Figure 36: Heights derived by retracking multi-look SARin waveforms (N=60) across Amazon on 5 May 2012. G-POD heights from SARinvatore.

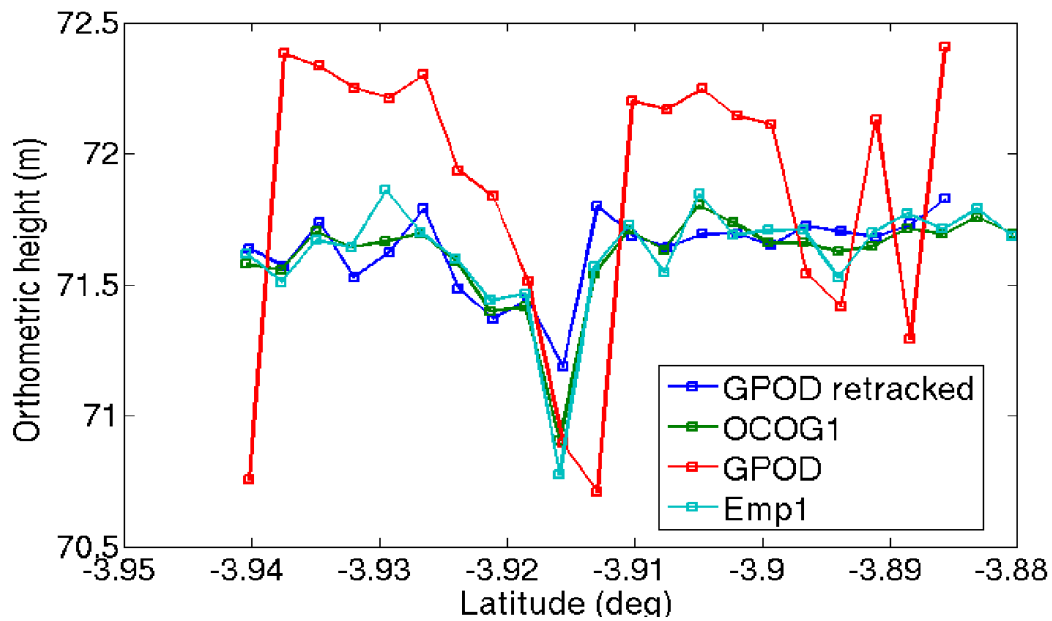


Figure 37: As Figure 36 but with G-POD waveforms retracked.

		ESA Contract:	1/6287/11/I-NB
		Doc. Title	D4200 Product Validation
		Doc. No	Report NCL_CRUCIAL_D4200
		Version No	3
		Date	30.08.17

4.2.2 Validation against gauge data at Tabatinga calibration

The Amazon near Tabatinga is plotted as Figure 38 for a stretch of the river some 150 km in length. This stretch has SARin mode passes that are about 2 days apart, but differ in longitude by 1.2° . Thus, given the small time difference we can assume that the derived SARin mode heights record the same river flows. The difference between the SARin river heights at the two locations provides an estimate of the slope of the river. Taking the average of these values gives a river slope of -4.42 cm per km along the river. This is equivalent to a ground slope of -0.0025° . On using this altimeter derived river slope and the location of the 64 crossings of the Amazon near Tabatinga, a slope corrected set of heights was obtained. The corrected heights, using RMS distances based on the centre line in Figure 38, and the gauge data are plotted as Figure 39. The agreement between gauge and altimetry has RMS of 29.9 cm on eliminating one clear outlier. This fit is better than that seen at Manacapuru although some 1500 km further upstream.

The SARin data has been used to derive the cross angle. The interpretation of the cross angle as the ground slope is, however, mostly incorrect as discussed in section 2.4. Even if the inland water body dominated the radar footprint the interpretation of the cross angle as the river slope is problematic as extreme care must be exercised in ensuring that the derived angle refers to the river. Even then the accuracy of the derivations must be lower than the river slope. The cross angle for 64 passes near Tabatinga are plotted as Figure 40 and summarized in Table 7. It would thus seem to be unrealistic to attempt to determine the Amazon river slope from SARin as the 95% confidence levels (2σ) are larger than the expected value.

In practice, Figure 40 shows a negative cross angle for both the North-South and South-North passes across the Amazon near the Tabatinga gauge. For confidence in the solution, the river slope should change sign with the pass direction. However, the roll-bias is subject to some uncertainty. If we allow the slope to change sign with the pass direction and then solve for a further roll-bias we infer a roll-bias correction of -0.004° and a slope of -0.0032° . This is close to the expected value but the 95% confidence interval is twice this value.

		ESA Contract:	1/6287/11/I-NB
		Doc. Title	D4200 Product Validation
		Doc. No	Report NCL_CRUCIAL_D4200
		Version No	3
		Date	30.08.17



Figure 38: Google earth image of Amazon near Tabatinga. Gauge marked in red. Yellow markers denote centre line of stretch considered for Cryosat-2 crossings.

		ESA Contract:	1/6287/11/I-NB
		Doc. Title	D4200 Product Validation
		Doc. No	Report NCL_CRUCIAL_D4200
		Version No	3
		Date	30.08.17

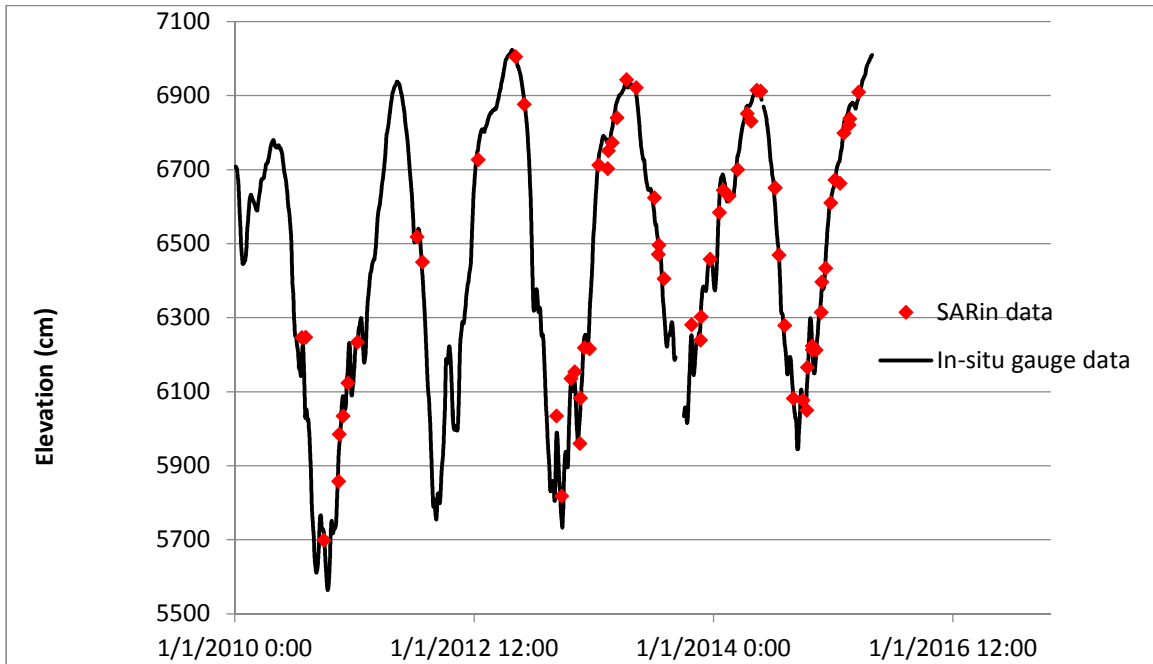


Figure 39: Tabatinga gauge heights and Cryosat-2 SARin (N=60, OCOG/Threshold) heights corrected for river slope. RMS difference 29.9 cm.

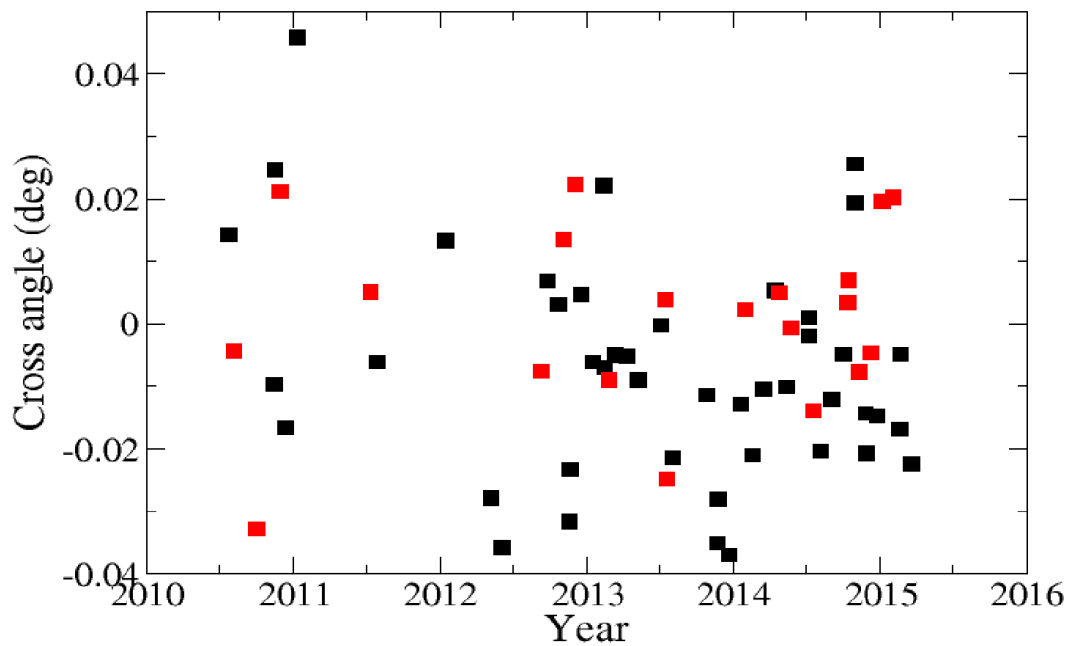


Figure 40: Plot of the 64 accepted cross angles comprising 44 ascending passes (black squares) and 20 descending passes (red squares).

		ESA Contract:	1/6287/11/I-NB
		Doc. Title	D4200 Product Validation
		Doc. No	Report NCL_CRUCIAL_D4200
		Version No	3
		Date	30.08.17

Pass	#	Mean (deg)	95% confidence (deg)
All	64	-0.0053	0.0054
Ascending	44	-0.0072	0.0053
Descending	20	-0.0009	0.0065

Table 7: Statistics of cross track angles from the 64 passes near Tabatinga. The expected value of the slope from SARin height differences is -0.0025°.

4.2.3 Analysis of the cross angle near the Tabatinga gauge

Figure 41 shows waveforms from the two antennae, the coherence and the phase for two locations over the Amazon. The left hand location (#274) is -3.929538°S, 70.207448°W with the adjacent (#275) at 3.926810°S, 70.207730°W in the right-hand column. The waveforms from the left and right antennae are near identical at both locations while the maximum coherence near the retrack point is 0.86 and 0.85 respectively for #274 and #275. The least squares estimated cross angle is 0.0296° for location #274 and 0.036° for location #275.

The differences between the heights from the two antennae and the cross angle as derived from the waveform bin phases are plotted as Figure 42. The Amazonas flood plain is visible as the latitudinal extent of low variability centered on 4.2°S. The difference in height measurements between the two antennae has a mean near zero and standard deviation near 1 cm. Note, differently from section 2.4, this difference uses the convention of height from the right antennae minus height from the second (left-side) antenna with antennae as orientated along the flight direction.

The interpretation of the cross angle is illustrated in Figure 43 where the upper plot shows the ground point locations of the 5 May 2012 ascending pass close to the Amazon while the lower plot aligns the cross angle. A positive offset of 0.025° was added to the cross angle to give a mean value near zero when the satellite was over the Amazon. A positive cross angle means that the dominant water body forming the leading edge of the waveform is under the right hand antenna and conversely for a negative cross angle. Thus the large and negative cross angle near latitude

		ESA Contract:	1/6287/11/I-NB
		Doc. Title	D4200 Product Validation
		Doc. No	Report NCL_CRUCIAL_D4200
		Version No	3
		Date	30.08.17

3.83°S is a response to the Amazon being to the left of the flight direct direction. The positive cross angles at the start of the pass are representative of a dominant reflectance from the right of the flight direction. Some care must be exercised as the actual extent of the Amazon at this time may differ from the Google earth image.

Other passes have been examined with a sample shown in Figures 44-47. In general the cross track angle is relatively noisy due to the complex nature of saturated ground and inland water. However, the plots generally show the expected behaviour of the cross angle particularly for large excursions of the river to left or right of the flight path.

		ESA Contract:	1/6287/11/I-NB
		Doc. Title	D4200 Product Validation Report
		Doc. No	NCL_CRUCIAL_D4200
		Version No	3
		Date	30.08.17

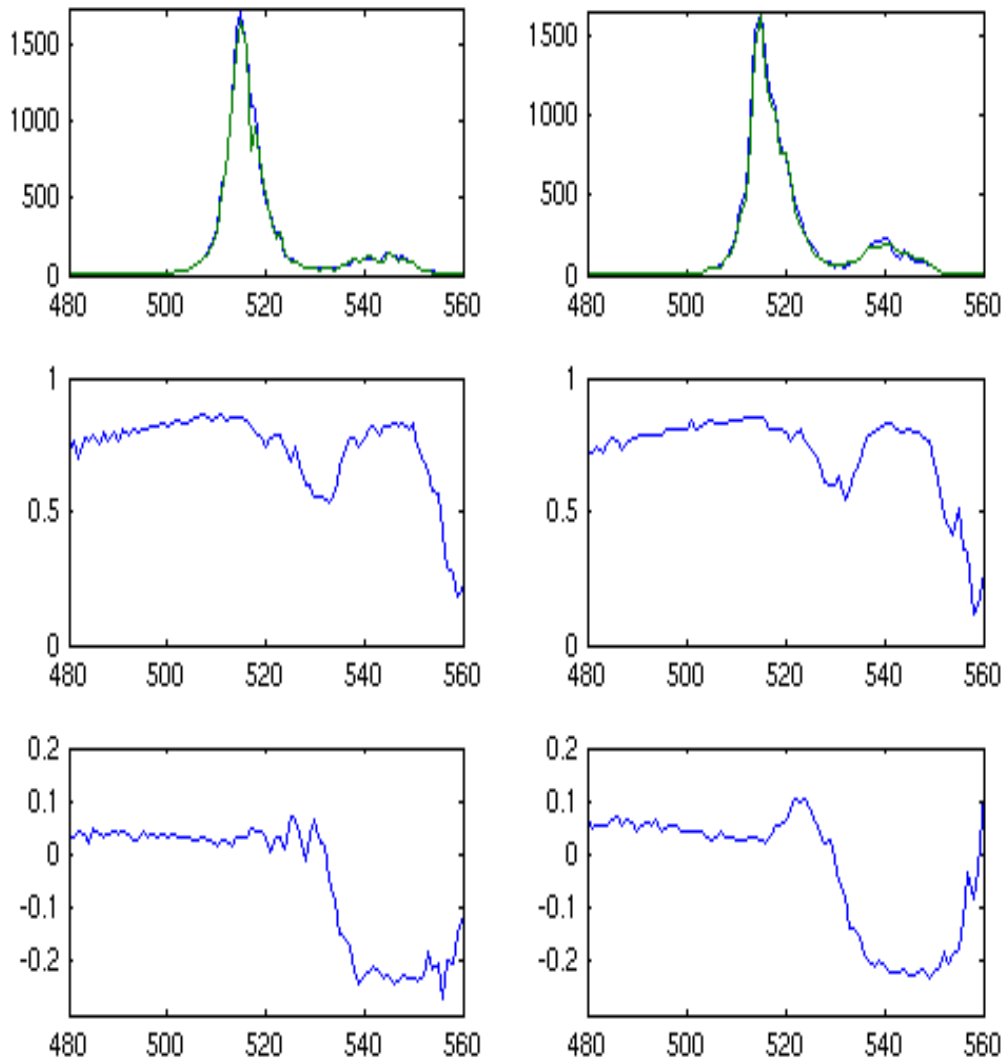


Figure 41: SARin waveforms (upper), coherence (middle) and cross angle in degrees (lower). In the upper plot the right antennae is coloured blue and the left antennae is green. X-axis is bin number; Y axis is power (upper), coherence (middle) and degree (lower). Left hand column location #274 (3.930 °S 70.207 °W); right hand column location #275 (3.927 °S 70.207 °W). Date of pass 5 May 2012.

		ESA Contract:	1/6287/11/I-NB
		Doc. Title	D4200 Product Validation
		Doc. No	Report NCL_CRUCIAL_D4200
		Version No	3
		Date	30.08.17

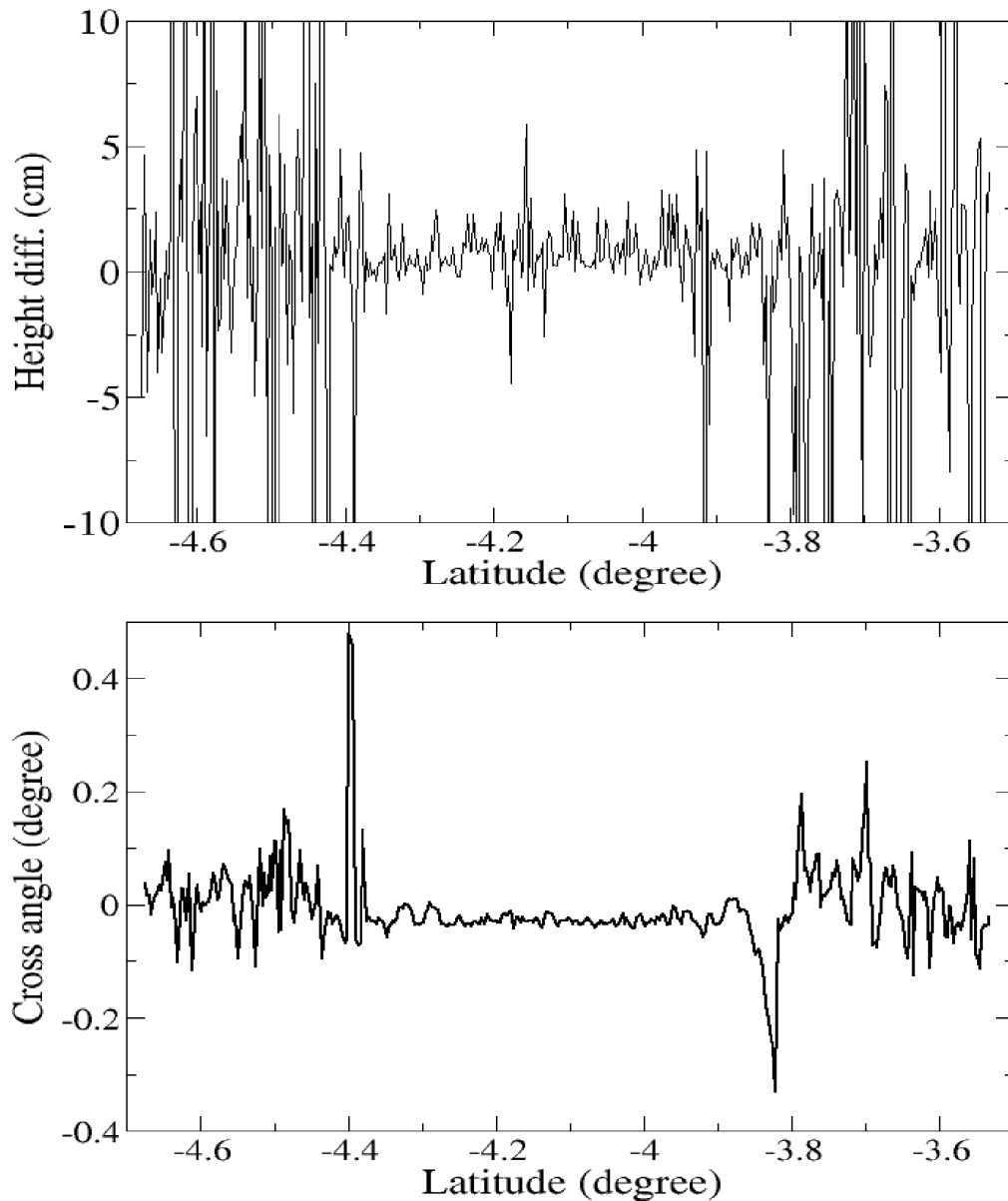


Figure 42: OCOG/Threshold based difference between heights from the two SARin antennae (Upper). Cross angle (Lower). SARin Amazonas 5 May 2012. (Latitude -4.2° corresponds to longitude 70.179°W).

		ESA Contract:	1/6287/11/I-NB
		Doc. Title	D4200 Product Validation
		Doc. No	Report NCL_CRUCIAL_D4200
		Version No	3
		Date	30.08.17



Figure 43: Google earth plot of ascending pass on 5 May 2012 across Amazon near Tabatinga (upper). Cross angles (deg) from SARin mode. The blue arrow points along direction of flight.

		ESA Contract:	1/6287/11/I-NB
		Doc. Title	D4200 Product Validation
		Doc. No	Report NCL_CRUCIAL_D4200
		Version No	3
		Date	30.08.17

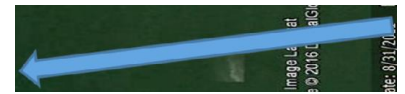


Figure 44: Google earth plot of ascending pass on 25 August 2012 across Amazon near Tabatinga (upper). Cross angles (deg) from SARin mode (lower). The blue arrow points along direction of flight.

		ESA Contract:	1/6287/11/I-NB
		Doc. Title	D4200 Product Validation
		Doc. No	Report NCL_CRUCIAL_D4200
		Version No	3
		Date	30.08.17

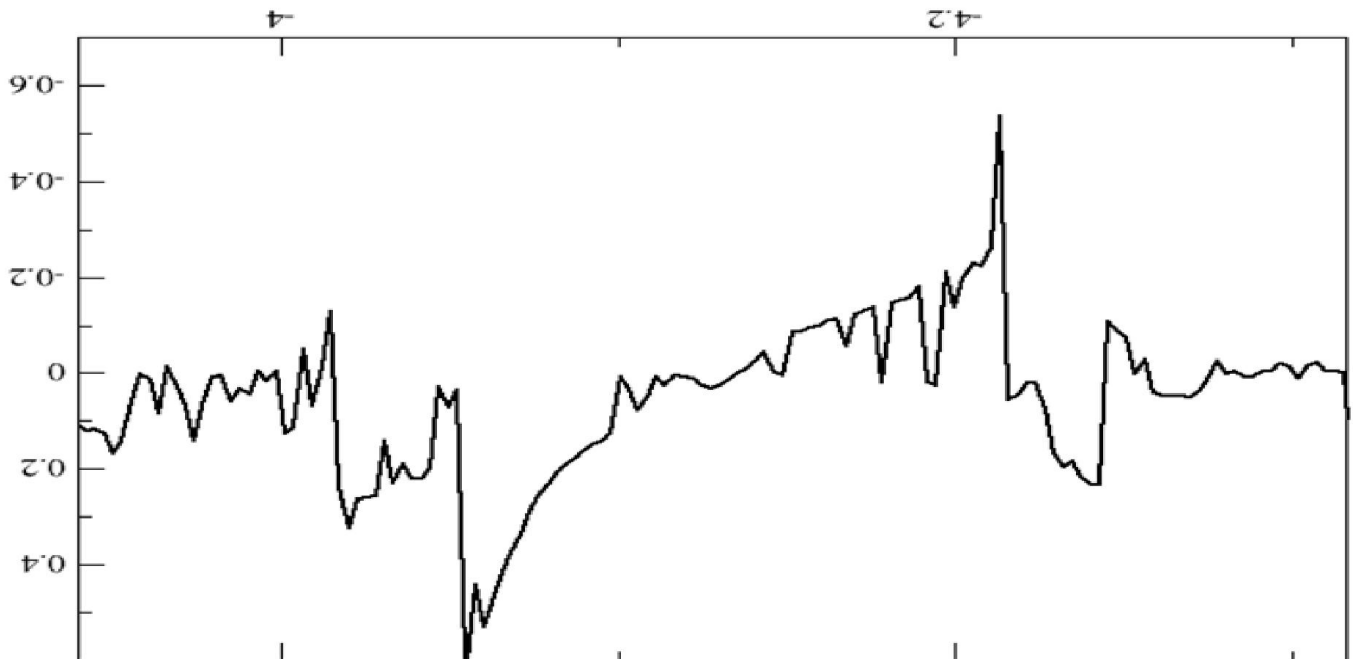


Figure 45: Google earth plot of descending pass on 8 September 2012 across Amazon near Tabatinga (upper). Cross angles from SARin mode (lower). The blue arrow points along direction of flight.

		ESA Contract:	1/6287/11/I-NB
		Doc. Title	D4200 Product Validation
		Doc. No	Report NCL_CRUCIAL_D4200
Version No		3	
Date		30.08.17	



Figure 46: Google earth plot of ascending pass on 23 September 2012 across Amazon near Tabatinga (upper). Cross angles (deg) from SARin mode (lower). The blue arrow points along direction of flight.

		ESA Contract:	1/6287/11/I-NB
		Doc. Title	D4200 Product Validation
		Doc. No	Report NCL_CRUCIAL_D4200
		Version No	3
		Date	30.08.17

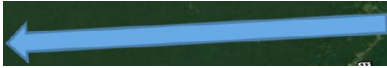


Figure 47: Google earth plot of ascending pass on 22 October 2012 across Amazon near Tabatinga (upper). Cross angles (deg) from SARin mode (lower). The blue arrow points along direction of flight.

		ESA Contract:	1/6287/11/I-NB
		Doc. Title	D4200 Product Validation
		Doc. No	Report NCL_CRUCIAL_D4200
		Version No	3
		Date	30.08.17

4.3 Brahmaputra

Cryosat-2 is in SARin mode for the upper and lower Brahmaputra. Given that SARin values from the University of Newcastle were not available early in the project the Danish Technological University used heights derived at DTU by retracking L1B waveforms. The purpose of this validation is to establish that the DTU heights and the heights derived later the University of Newcastle from L1A SARin FBR data are equivalent.

DTU used waveforms from the ESA baseline-b L1B 20 Hz data product with the waveforms retracked using a primary peak threshold retracker. In contrast, the CRUCIAL results utilized the FBR SAR L1A SAR data ab initio to construct the waveforms. For retracking DTU adopted a threshold of 0.8 compared with 0.75 in CRUCIAL. As stated previously, the L1B data use all waveforms ($N \approx 120$) while the CRUCIAL waveforms used in the stack are more tightly centred about the nadir directions ($N=40$). Details of the DTU approach are given in Villasden et al. (2015).

Utilising locations (latitude and longitude) retracked at DTU the equivalent L1A SARin FBR heights were derived by interpolating with respect to latitude. Interpolation is necessary as the respective data sets utilized different ground points. Interpolations within the University of Newcastle values produced the value at the nearest location to the DTU ground point. Note that interpolation between NCL values could involve a point off the river. However, as there are usually multiple points per pass this is not a major problem. Figure 48 plots the Newcastle and DTU derived heights for all interpolated points showing some obvious outliers. The difference between the NCL and DTU values are plotted as Figure 49. Again obvious outliers are evident. Points were rejected based on the median value and extending the window of data accepted to include all points within 3σ of the window mean. In practice hydrological assimilation requires a single value from the river crossing and use of say the median value would mitigate against spurious values. Figure 50 shows the stretch of the lower Brahmaputra used in hydrological modelling. These two figures involve data from 35 passes across the Brahmaputra some of which are a few days apart and thus the passes are indistinguishable on the time series plot. 170 heights out of the possible 185 heights were accepted. The mean difference was 11.8cm with standard derivation of 15.7 cm. The 12 cm offset is due to different procedures including the threshold for retracking. More important is the scatter in the data and with a standard deviation of just 16 cm we are confident that the data set used in the hydrological assimilation and modelling is of high accuracy.

		ESA Contract:	1/6287/11/I-NB
		Doc. Title	D4200 Product Validation
		Doc. No	Report NCL_CRUCIAL_D4200
		Version No	3
		Date	30.08.17

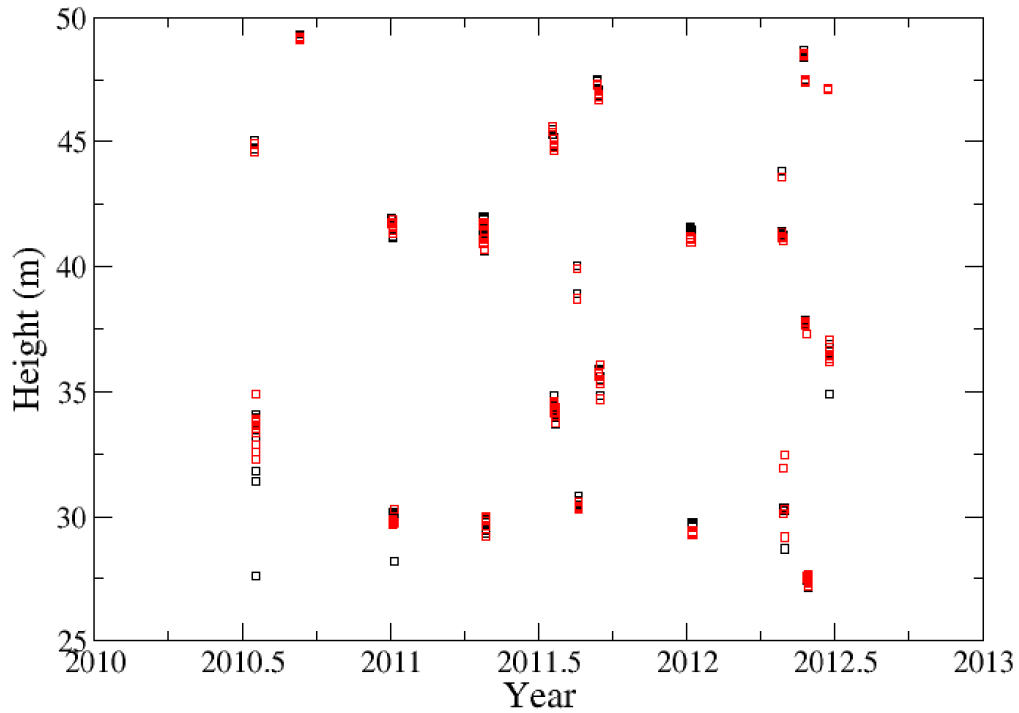


Figure 48: Cryosat-2 SARin heights across the Brahmaputra. CRUCIAL heights (N=60, OCOG/Threshold) (black squares) and DTU derived heights (red squares).

		ESA Contract:	1/6287/11/I-NB
		Doc. Title	D4200 Product Validation
		Doc. No	Report NCL_CRUCIAL_D4200
		Version No	3
		Date	30.08.17

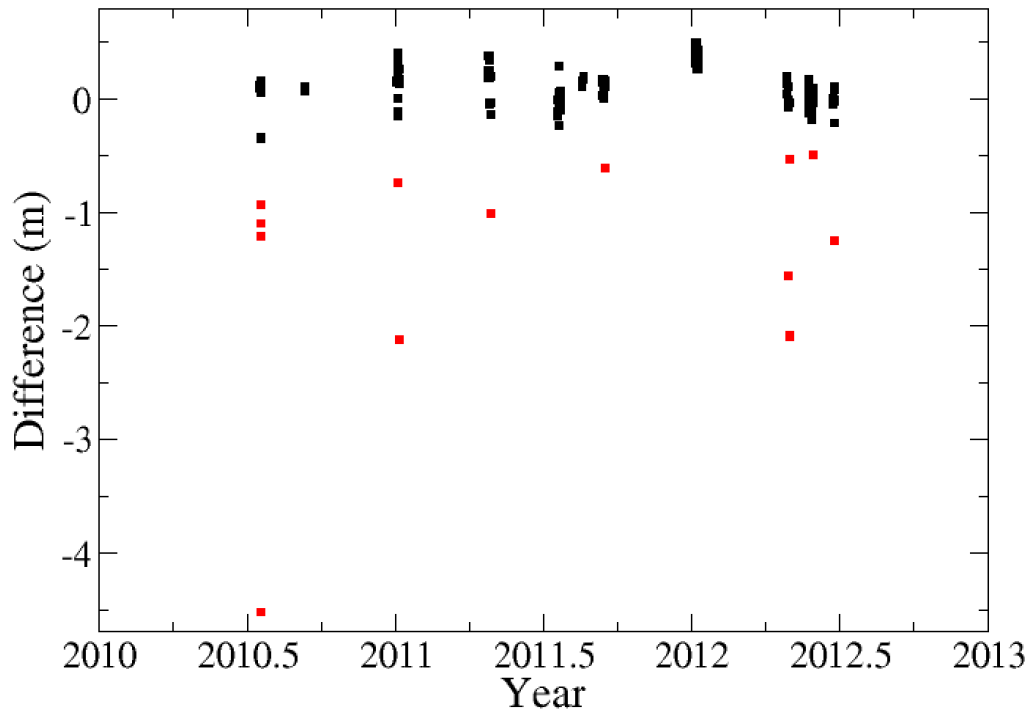


Figure 49: The height difference between NCL and DTU heights across the Brahmaputra. Accepted points denoted by black squares, rejected points by red squares. Mean difference and standard deviation of accepted points 11.9cm and 15.8 cm, respectively.

		ESA Contract:	1/6287/11/I-NB
		Doc. Title	D4200 Product Validation
		Doc. No	Report NCL_CRUCIAL_D4200
		Version No	3
		Date	30.08.17

5 Summary of validation of FBR SAR and SARin inland water heights

The above sections details the validation of heights derived by processing SAR and SARin FBR L1A data. A number of significant conclusions can be drawn for inland water studies.

- The speckle in the burst echoes affects the recovered heights from the 80 Hz SAR data and multi-look waveforms are essential for precise heights.
- The number of stacked waveforms used in the construction of the multi-look waveform is important for SAR altimetry. A reduction from the maximum possible number in the stack of approximately 240 (N=120) to say 81 (N=40) waveforms centred on the beam directed closest to nadir has been seen to reduce the variability in derived heights across Tonlé Sap.
- The reduction from N=120 to N=40 in the waveform stack sharpens the leading edge of the multi-look waveform. The change in N causes an offset between the derived heights which is indistinguishable from other contributions to the altimeter bias. In consequence, a fixed value for N must be applied to all analyses to avoid bias.
- The G-POD SARvatore and SARinvatore waveforms are almost identical to those derived within CRUCIAL on using N=120 or N=123.
- The use of a Hamming window (cosine weighting) is recommended (see Table 1).
- The difference between the empirical retrackers and OCOG/Threshold is not significant. More advanced retrackers or the use of auto-correlation between consecutive waveforms across large lakes might change this conclusion. Variability in height recovery has been shown to be 5 cm across Tonlé Sap for multi-look SAR data at about 20 Hz. This is equivalent to a precision of 1-2 cm in 1 Hz data.
- Validation of altimetric heights across Tonlé Sap is affected by distance from the gauge. For OSTM a 12 day lag has been inferred with respect to the Prek Kdam gauge. This lag increases with distance of the pass from Prek Kdam as shown by the auto-correlation analysis between the Prek Kdam and Kumong Luong gauges. The agreement between Prek Kdam and OSTM of 42.6 cm is slightly reduced to 42.1 cm between Prek Kdam and Cryosat-2. The latter assumes the time lag for all Cryosat-2 non-repeating passes is that of OSTM (i.e. 12 days) and that the EGM08 geoid is accurate. Since the former, in particular, has been shown to be incorrect there is evidence that Cryosat-2 is performing better than OSTM across Tonlé Sap.
- The SAMOSA2 retracking in G-POD is inappropriate for inland waters as seen by the statistics across Tonlé Sap in Table 1 and the Mekong in Figure 10. Retracking the G-POD waveforms

		ESA Contract:	1/6287/11/I-NB
		Doc. Title	D4200 Product Validation
		Doc. No	Report NCL_CRUCIAL_D4200
		Version No	3
		Date	30.08.17

using the empirical trackers developed in CRUCIAL or with the OCOG/Threshold retracker yields enhanced results.

- Validation of Cryosat-2 inland water heights along the Mekong are severely affected by the non-repeating orbit. Correction based on low flow river slope is not exact as the gauges show a difference in range and hence a change in slope at high flow.
- A comparison of the OCOG/Threshold (RMS 66.9 cm) and empirical retracker (67.8 cm) for N=40 in Figure 20 shows a slight preference for the OCOG/Threshold retracker. These differences are comparable to those of Birkinshaw et al (2010) where an RMS of 76 cm was seen for ERS-2 for the years 1995-2003 and 57 cm for Envisat for the years 2002-2008.
- FBR SAR data close to the Obidos gauge on the Amazon allowed the river slope to be computed from the gauge/altimetry residuals and chainage. Using least squares to determine the river slope. The recovered slope was -0.22 cm per km. On correcting for the slope the RMS between Cryosat-2 and the Obidos gauge data was 34.9 cm and applying a 2.5σ rejection criterion eliminated two points but reduced the RMS to 27.3 cm. The slope with $R^2 = 0.07$ was just positive. At Manacapuru, 650 km upstream from Obidos, the RMS, after similarly allowing for the slope, was 52.6 cm. Here the slope of -0.429 ± 0.024 was well determined with $R^2 = 0.89$. These RMS values can be compared against Birkett et al. (2002), where best results from Topex/Poseidon for 1992-1999 were in the range 0.4–0.6 m RMS. Thus, the Manacapuru RMS falls within the Birkett et al. (2002) best results while the Cryosat-2 result at Obidos is superior by a factor of two.
- Analyses of SARin FBR data for an ocean pass shows slightly less accurate results compared to the G-POD SARinatore heights. This is not unexpected as G-POD uses the SAMOSA2 retracker designed for ocean applications. Analysis of the sea-surface slope gave a mean and standard deviation of 0.0007° and 0.0034° respectively giving confidence to the procedure.
- Heights from SARin FBR data in the vicinity of the gauge at Tabatinga yielded an RMS of 29.9 cm. Again this is an improvement on the best results of Birkett et al. (2002) for the Amazon.
- The SARin cross angle is dominated by the location of the dominant water surface reflectors in the cross-track footprint slice.
- In general the cross track angle recovered from SARin FBR data is relatively noisy due to the complex nature of saturated ground and inland water. However, the results generally show the expected behaviour of the cross angle particularly for large excursions of the river to left or right of the flight path.
- Heights for the Lower Brahmaputra derived by DTU from SARin L1B waveforms retracked using a primary peak threshold retracker were consistent with results obtained within CRUCIAL from L1A data. A 12 cm offset is due to the different procedures including the waveform construction and threshold for retracking. More important is the scatter in the data

		ESA Contract:	1/6287/11/I-NB
		Doc. Title	D4200 Product Validation
		Doc. No	Report NCL_CRUCIAL_D4200
		Version No	3
		Date	30.08.17

and with a standard deviation of just 16 cm. We are thus confident that the DTU data used in the Data Assimilation work is of high accuracy.

6 Assimilation of CryoSat-2 data to 1-dimensional hydrodynamic models

The spatial and temporal resolution of Cryosat-2 altimetry data over rivers is not yet sufficient to create an estimate of river water levels (and respective discharges) continuous in space and time. This also applies if Cryosat-2 altimetry is combined with data from other satellite altimetry missions. Commonly, for river discharge and water level forecasting, hydrologic-hydrodynamic models are used. These models however can benefit from the information from satellite altimetry: data assimilation (DA) allows to inform models with observations from, for example, satellite altimeters, with the aim of improving the model's forecast skills.

DA of satellite altimetry data to hydrologic-hydrodynamic models is being performed successfully. Just a few examples are the works by Paiva et al. (2013) assimilating Envisat altimetry data to a model of the Amazon River, Michailovsky et al. (2013) assimilating Envisat altimetry data to a model of the Brahmaputra River, or Hossain et al. (2014) who have developed an operational forecasting system for the Brahmaputra and Ganges River in Bangladesh, which is being informed by altimetry data from JASON-2.

Most of the work using satellite altimetry data, as also the above mentioned studies, uses data in a virtual station format: Altimetry satellites usually are on an orbit with a repeat cycle between 10 and 35 days (see for example Schwatke et al. (2015) for an overview over the current satellite altimetry missions). Such orbits allow the extraction of time series of water levels at the distinct locations of the satellite ground track intersecting the river. This simplifies processing of the altimetry data and also its integration into river models.

Cryosat-2, however, has a unique drifting orbit with a repeat cycle of 369 days, which does not allow the (direct) extraction of water level time series. Hence, many common techniques of processing and working with satellite altimetry data over rivers are being challenged.

		ESA Contract:	1/6287/11/I-NB
		Doc. Title	D4200 Product Validation
		Doc. No	Report NCL_CRUCIAL_D4200
		Version No	3
		Date	30.08.17

6.1 Data and methods

For details of this section please refer to D4100, as this part of the project focusses on the results of assimilating Cryosat-2 altimetry data to a hydrologic-hydrodynamic river model.

6.1.1 Hydrologic-hydrodynamic model of the Brahmaputra River

To demonstrate the potential value of combining Cryosat-2 altimetry with river models, a hydrologic-hydrodynamic model of the Brahmaputra River in South Asia was set up. This was done in cooperation with DHI (Danish Hydraulic Institute, www.dhi.dk), using the DHI MIKE Hydro River software. The hydrologic part of the model consists of 33 lumped NAM rainfall-runoff subcatchments Nielsen and Hansen, 1973. The river flow then is modelled using a 1D dynamic wave routing based on the Saint Venant equations for unsteady flow MIKE by DHI, 2009.

Due to restricted access and limited availability of in situ data, the model's parameterization and forcing is almost entirely based on remote sensing data and other globally available data products. The only exception of this is in situ discharge data at Bahadurabad station, at the outlet of the Brahmaputra basin model. This station's data was used to calibrate discharge in the model. The reliance on globally available data sources ensures that the presented model setup and cross section calibration is applicable to any river basin of sufficient size.

		ESA Contract:	1/6287/11/I-NB
		Doc. Title	D4200 Product Validation
		Doc. No	Report NCL_CRUCIAL_D4200
		Version No Date	3 30.08.17

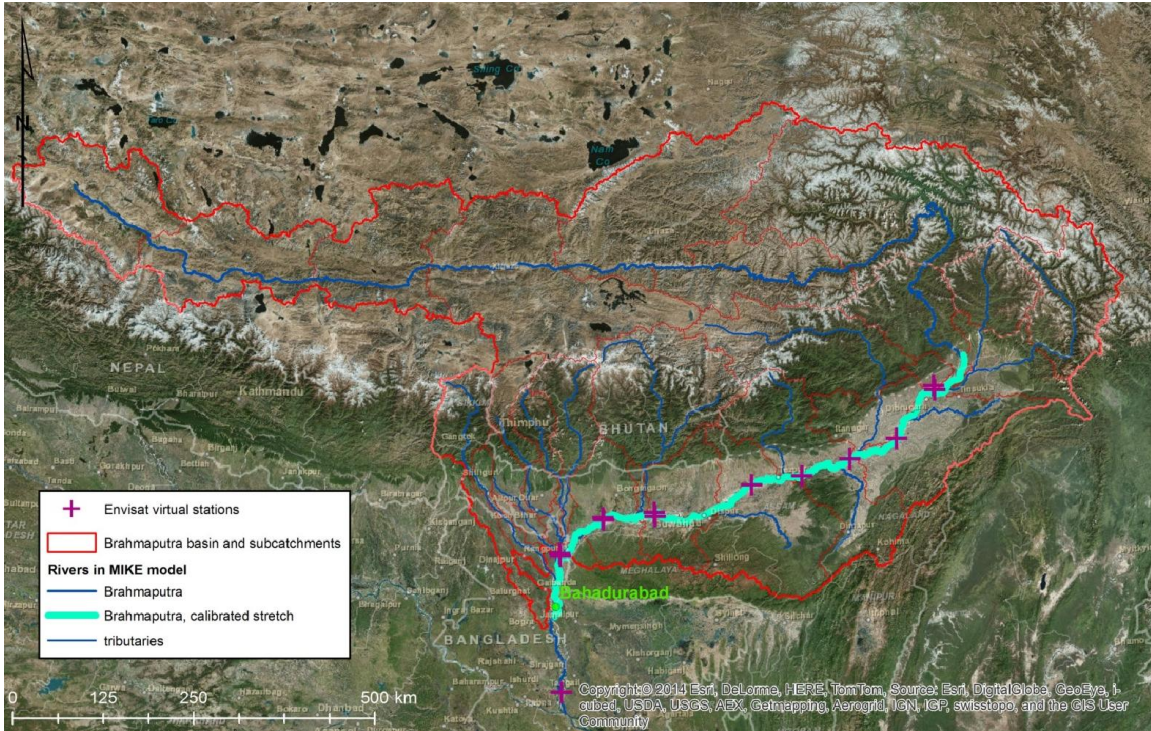


Figure 50: The Brahmaputra basin model. The main discharge calibration station, Bahadurabad in Bangladesh is shown. Furthermore, the stretch of the model (the Assam Valley) relevant for the DA is highlighted, along with the Envisat virtual stations used in the cross section calibration.

The further work will focus on the Assam Valley part of the Brahmaputra model (as highlighted in Figure 50), as this is the only stretch of the river where also virtual station altimetry data exists. This type of data is required for the calibration of simulated water levels, see section 6.1.4.

6.1.2 Cryosat-2 data

The Cryosat-2 data used in this part of the project was level 2 altimetry data that was processed and provided by The National Space Institute, Technical University of Denmark in the framework of the LOTUS project (<http://www.fp7-lotus.eu/>). This was retracked by Villadsen et al. (2015) using a primary peak threshold retracker. Most of the study area is covered in the Synthetic Aperture Radar Interferometer (SARin) mode of Cryosat-2. The SAR mode of Cryosat-2 offers an along track resolution of 300m, whereas the SARin mode is adopted to deal with areas presenting a high surface slope by additionally using a second across-track antenna. This allows to determine off-nadir locations of the altimetric observations Armitage and Davidson, 2014. The data is available since July 2010. For this report, data until the end of 2013 have been used.

		ESA Contract:	1/6287/11/I-NB
		Doc. Title	D4200 Product Validation
		Doc. No	Report NCL_CRUCIAL_D4200
		Version No	3
		Date	30.08.17

6.1.3 Processing of the data

Cryosat-2 data or metadata does not directly deliver reliable information whether it was acquired over land or over (small inland) water surfaces. Hence, the distinction between Cryosat-2 data points representing the water or land surface has to be based on a water mask. This water mask was derived from Landsat NDVI imagery. Because of the dynamic nature of the Brahmaputra's braided river bed, river masks were updated once per year.

After filtering over the relevant river masks, the Cryosat-2 data has to be projected onto the river model line as shown in Figure 51. Note that the river model is 1-dimensional. For details and the resulting extracted data from this procedure please refer to D4100.

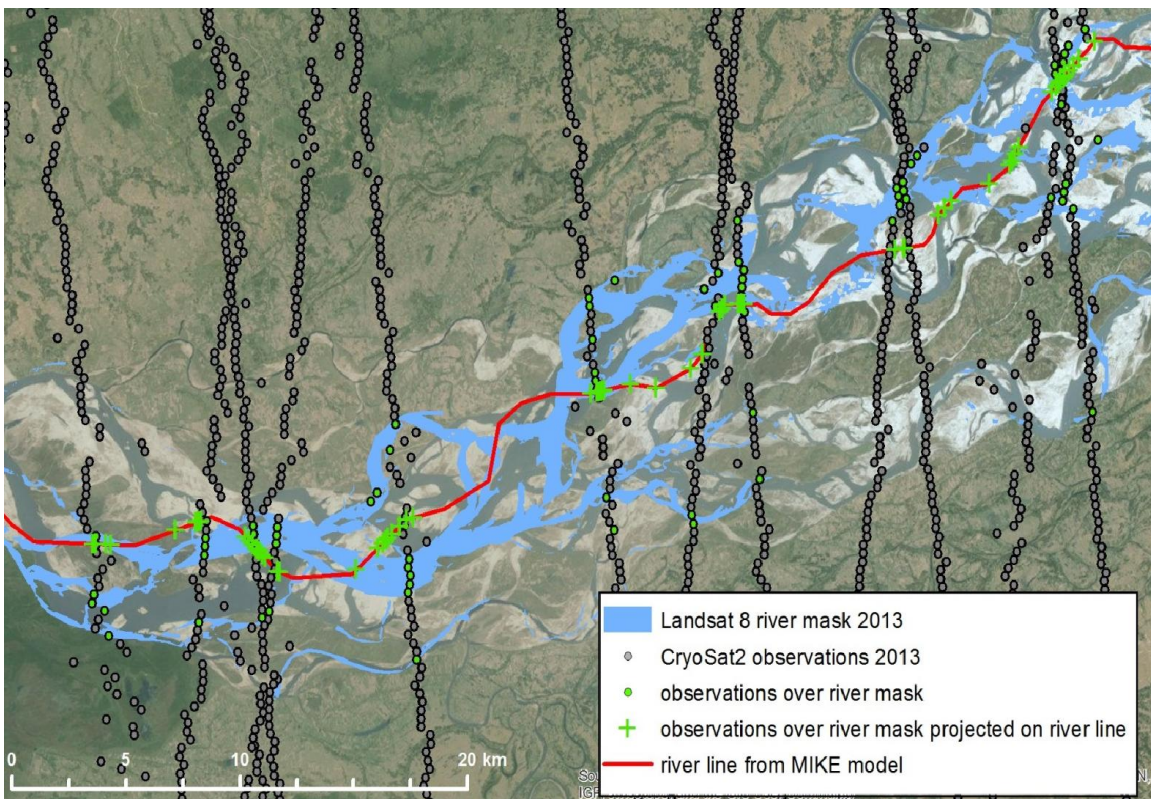


Figure 51: Section of the Brahmaputra in the Assam valley showing the Landsat river mask, the Cryosat-2 observations and their mapping to the 1D river model, all for 2013.

6.1.4 Cross section calibration

To be able to inform a hydrodynamic model with Cryosat-2 data in any way, it is necessary that the respective model accurately reproduces water levels. This again is affected by the distributed

		ESA Contract:	1/6287/11/I-NB
		Doc. Title	D4200 Product Validation
		Doc. No	Report NCL_CRUCIAL_D4200
		Version No	3
		Date	30.08.17

nature of the Cryosat-2 data, which requires that water levels – absolute water levels as well as water level amplitudes – are accurately modelled at any point in time and space of the model. Hence, after the discharge calibration of the model (see section 6.1.1 and details in D4100), also water levels had to be calibrated.

Lacking an accurate DEM, the reference model’s datums were extracted from the SRTM DEM, and bathymetry data, an approach using synthetic, triangular shaped cross sections was chosen. Those cross sections were i) datum-adjusted so that the average simulated water level profile along the river fitted to the observed Cryosat-2 altimetry data, and ii) angle-adjusted so that the simulated water level amplitudes fitted to the observed water level amplitudes in Envisat virtual station altimetry. A sketch of this for one cross section is shown in Figure 52.

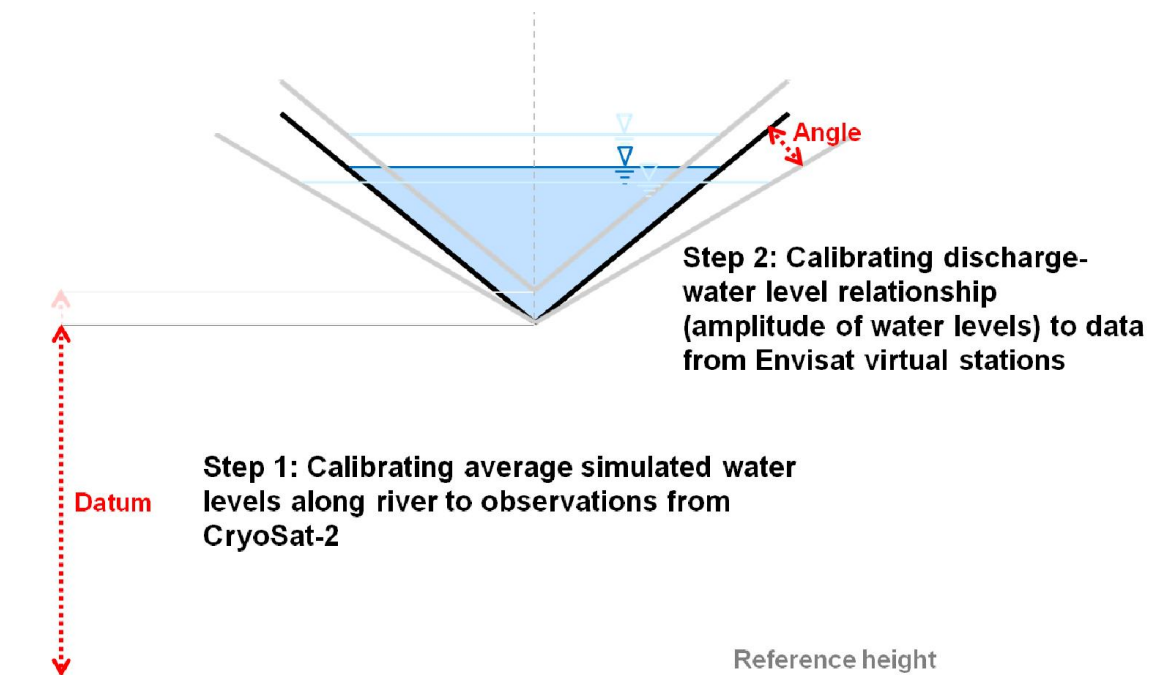


Figure 52: Sketch of the two-step cross section calibration process for one cross section, displaying the optimization parameters datum and angle.

As mentioned, the cross section calibration was performed after discharge calibration of the model. Cross section calibration showed to have only negligible influence on discharge routing, hence the entire calibration procedure for the model is as displayed in the flow chart in Figure 53.

		ESA Contract:	1/6287/11/I-NB
		Doc. Title	D4200 Product Validation
		Doc. No	Report NCL_CRUCIAL_D4200
		Version No	3
		Date	30.08.17

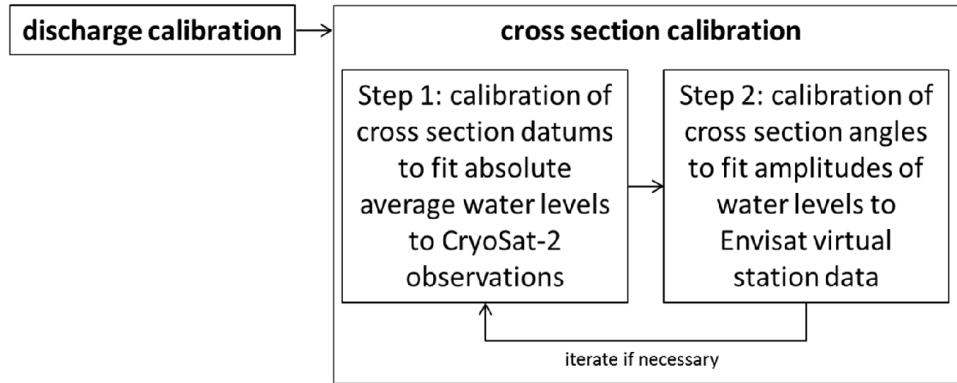


Figure 53: Flow chart showing the calibration of both discharge and water levels in the hydrodynamic model.

A hydrodynamic model calibrated in the way described here, accurately representing water levels and discharge in the entire model space, can be not only be the basis for assimilation of Cryosat-2 altimetry data, but in principle should be able to ingest any kind of water level information.

6.1.5 DHI Data Assimilation Framework

To be able to assimilate altimetry data of the distributed nature of Cryosat-2, a flexible DA framework was developed in cooperation with DHI that allows the assimilation of basically any altimetry information to MIKE 1D hydrodynamic models.

The DHI Data Assimilation Framework provides various filters, error models and observation mapping methods to assimilate various datasets to MIKE models. It is written in .NET/C# and communicates directly with the MIKE models. An overview over the framework can be seen in Figure 54. Configuration details are provided through an ASCII configuration file (.altpfs file). The framework provides different Kalman filtering algorithms such as EnKF and ETKF, or also a defined gain method. It also allows for state augmentation with a time-constant bias term, which is then estimated by the filter. Localization approaches are also provided, i.e. the state updating is restricted to model states in the neighbourhood of the measurement location. This is useful to avoid artefacts created by spurious correlations due to the limited ensemble size (Evensen, 2009, chapter 16). In the context of the assimilation of radar altimetry to a hydrodynamic model this for example has been discussed by Paiva et al. (2013). The framework also provides templates for the parameterization of model errors, including perturbation of the initial conditions and auto-correlated error representations for the model forcings. The auto-correlated model error is integrated in the model state using state augmentation.

		ESA Contract:	1/6287/11/I-NB
		Doc. Title	D4200 Product Validation
		Doc. No	Report NCL_CRUCIAL_D4200
		Version No	3
		Date	30.08.17

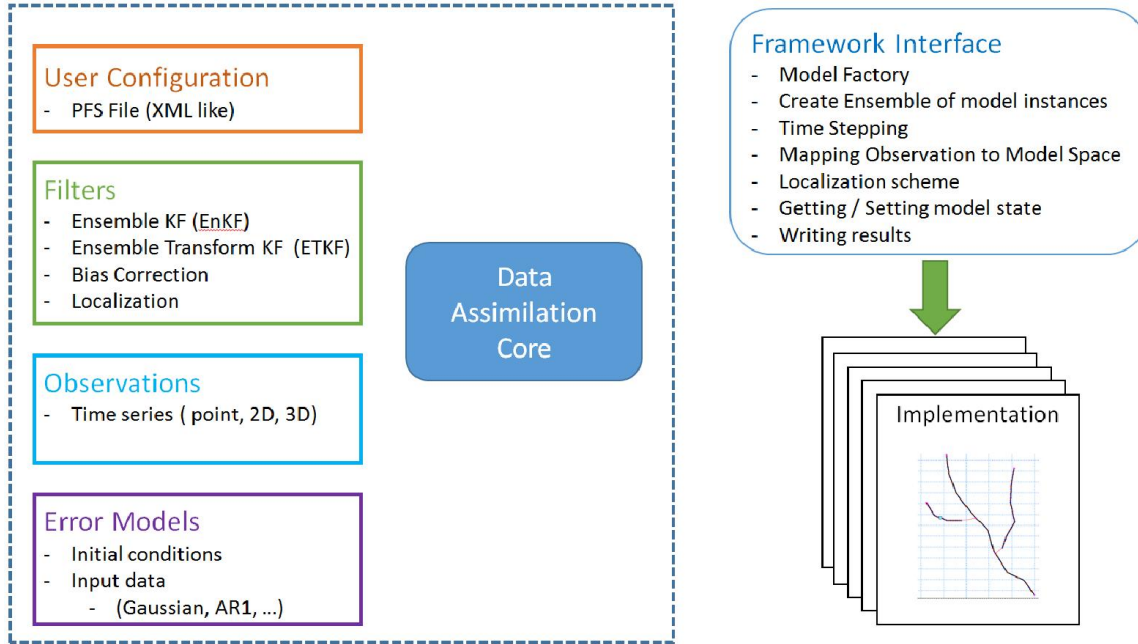


Figure 54: Overview over the DHI Data Assimilation Framework. Source: Marc-Etienne Ridler, DHI.

For our case, a version that ingests altimetry data as for example delivered by Cryosat-2 was used. The challenge with assimilating Cryosat-2 data is its spatial and temporal distribution. Commonly in hydrologic modelling assimilated data consists of time series of some value at certain points in the model space. Cryosat-2 however provides observations distributed over the entire model space at various points in time. Hence, the above described ETKF was chosen, and the modelled water levels were calibrated across the entire model as described in section 6.2.2.

For details of the DA setup with the Brahmaputra model, that were used to produce the results presented in the following, please refer to D4100.

6.1.6 Synthetic DA experiment

To test whether the just presented DA Framework works in principle, and to evaluate the potential value of Cryosat-2 altimetry data for hydrodynamic models, a synthetic DA experiment was conducted.

For this synthetic experiment, first a hidden truth model was created. This hidden truth model only differs from the original model by being forced by a perturbed version of the runoff forcing originating from the rainfall-runoff models. This perturbation leads to a different discharge and respective water levels in the model. From this hidden truth model, water levels were sampled at the exact locations and times of the real Cryosat-2 observations. White noise with a standard deviation of 0.2 or 0.4 metres was added to those synthetic measurements. There is no in situ

		ESA Contract:	1/6287/11/I-NB
		Doc. Title	D4200 Product Validation
		Doc. No	Report NCL_CRUCIAL_D4200
		Version No	3
		Date	30.08.17

data available to directly estimate the standard error of CryoSat-2 observations over the Brahmaputra River. However, an analysis of the CryoSat-2 data, assuming that data points from individual transects should represent the same water level, showed mean standard errors in the range of 0.3 metres. Hence, adding a standard error of 0.2 or 0.4 metres is considered a realistic estimate of true uncertainty.

When assimilating the synthetic observations extracted from the hidden truth model to the original model, one expects the original model to be corrected towards the hidden truth model. The results from the synthetic DA experiments will be presented in section 6.2.3, and the results from DA experiments using the real CryoSat-2 data will be presented in section 6.2.4.

6.2 Results and Discussion

6.2.1 Discharge calibration

After calibrating the rainfall-runoff models, the entire hydrodynamic model was calibrated to in situ observations at its outlet, at Bahadurabad station in Bangladesh (see Figure 50): Manning's number was adjusted, affecting the timing of the discharge routing.

Besides that, it was observed that the precipitation forcing likely is underestimating the actual precipitation. This applied both for the single subcatchments' rainfall-runoff models and the entire Brahmaputra River at Bahadurabad station. Scaling the TRMM 3B42 v7 precipitation forcing with a factor of 1.4 yielded good results in terms of water balance. An underestimation of precipitation by remote sensing products has been observed before, especially in regions where a relevant share of precipitation originates from small-scale convective rainfall events: Michailovsky et al. (2013) for example scaled the TRMM 3B42 product with a factor of 1.25 to obtain good results for a hydrologic model of the Brahmaputra River basin.

Figure 55 shows simulated and observed discharge at Bahadurabad station for both calibration and validation period. Note that during the validation period 2010 to 2013, data was available only for the high-flow season, i.e. mainly from the beginning of April to the end of October. This is also accounted for in Table 8, showing performance criteria comparing simulated and observed discharge at Bahadurabad station. It can be seen that the Nash-Sutcliffe efficiency (NSE) decreases from 0.89 to 0.81 between the calibration and validation period. The NSE is a popular indicator to assess the performance of hydrological models and is calculated as

		ESA Contract:	1/6287/11/I-NB
		Doc. Title	D4200 Product Validation
		Doc. No	Report NCL_CRUCIAL_D4200
		Version No	3
		Date	30.08.17

$$NSE = 1 - \frac{\sum_{t=1}^T (Q_{obs}^t - Q_{sim}^t)^2}{\sum_{t=1}^T (Q_{obs}^t - \bar{Q}_{obs})^2} \quad (10)$$

where Q_{obs}^t and Q_{sim}^t are observed and simulated discharges at time t . \bar{Q}_{obs} is the mean observed discharge. An NSE of 1 means that the simulation matches the observations perfectly, an NSE of 0 means that the simulated discharge is predicting observed discharge as good as the mean of observed data would. Hence, an NSE well above 0, close to 1 is desirable.

More notable however is the fact that, unlike during the calibration period, there is a clear bias in discharge during the validation period, meaning the model is overestimating discharge. In the calibration period, there was a slight underestimation. This behaviour cannot be explained directly, it for example may be due to biases in the temperature, evaporation and precipitation forcings, even though consistent products for the entire simulated period 2002 to 2013 have been used. Another possible explanation are changes in climate or anthropogenic interventions in the river system. Also, the in situ data may have flaws; discharge values are derived from water levels via a rating-curve introducing considerable uncertainty especially with large dynamic rivers such as the Brahmaputra River (see for example Sarma, 2005 for an analysis of stage-discharge relationships in the Brahmaputra).

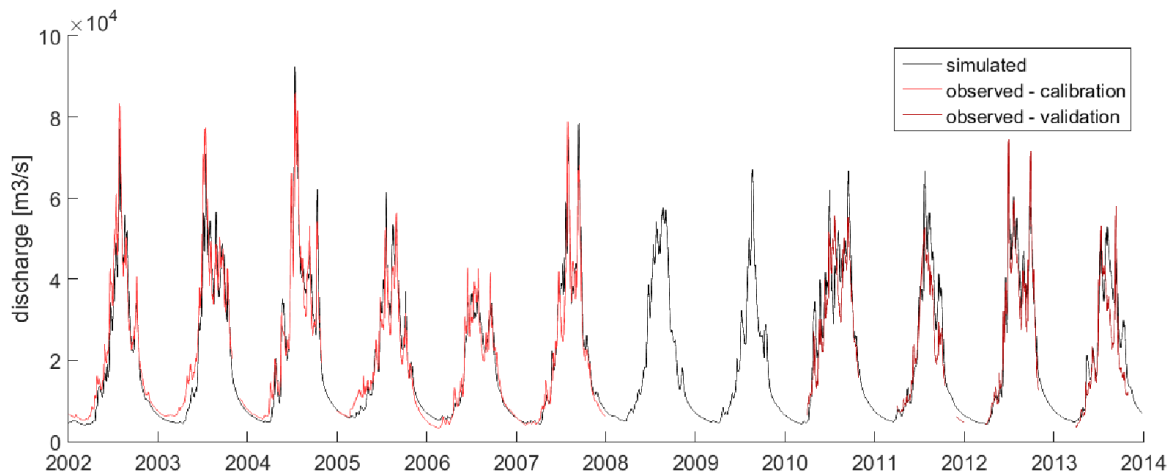


Figure 55: Simulated discharge at Bahadurabad station together with in situ observations. Calibration period: 2002 - 2007, validation period: 2010 – 2013.

		ESA Contract:	1/6287/11/I-NB
		Doc. Title	D4200 Product Validation
		Doc. No	Report NCL_CRUCIAL_D4200
		Version No	3
		Date	30.08.17

Table 8: Performance criteria for simulated discharge Q at Bahadurabad station. $\text{bias} = (Q_{\text{sim}} - Q_{\text{obs}}) / Q_{\text{sim}}$

	RMSE [m ³ /s]	NSE [-]	bias [%]
Calibration period 2002 – 2007	4329	0.93	-2.1
Calibration period, high-flow only	5323	0.89	-2.3
Validation period 2010 – 2013	6873	0.81	11.2

6.2.2 Cross section calibration

The results of the first step of the cross section calibration, i.e. the cross section datums adjustment can be seen in Figure 56. For better visibility, all elevations are shown relative to the reference model's cross section datums. The reference model's datums were extracted from the SRTM DEM. It can be seen easily that the average simulated water levels along the river from the reference model do not accurately represent the water levels observed by Cryosat-2. After datum calibration, some of the datums were moved by more than 5 metres compared to the reference model. The RMS between average simulated water levels and the Cryosat-2 observations was reduced from 3.1 metres for the reference model to 2.5 metres. The remaining deviation can largely be explained by the seasonal water level changes. Using data from a repeat orbit mission such as Envisat would – due to lower spatial resolution – not allow to calibrate the exact water level profile in the river.

		ESA Contract:	1/6287/11/I-NB
		Doc. Title	D4200 Product Validation
		Doc. No	Report NCL_CRUCIAL_D4200
		Version No	3
		Date	30.08.17

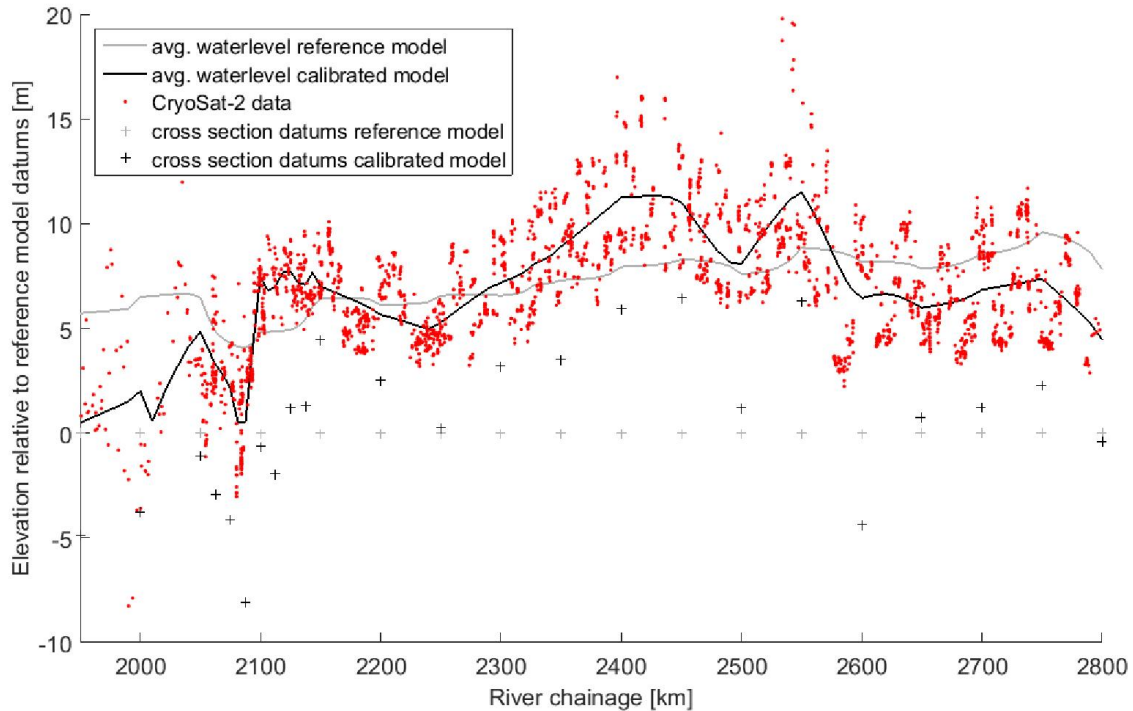


Figure 56: Result of the cross section calibration step 1 for the Assam Valley for the period 2010 to 2013. All levels are shown relative to the reference model's cross section datums based on SRTM DEM.

Figure 57 displays the results from the second step of the cross section calibration, i.e. adjusting the cross section angles, for one of the 13 virtual stations. The yearly water level amplitudes observed by Envisat can be reproduced; the RMS between simulated and observed yearly water level amplitudes across all 13 virtual stations was 0.8 metres after the calibration.

Changing the cross section angles in this step also showed to have not only an effect on water level amplitudes, but also on absolute average water levels. Hence, the first step of the calibration was repeated after the second step, which is also expressed in the flow chart in Figure 53.

Changing the cross section datums and angles in the calibration process showed to have no relevant effect on the discharge routing of the hydrodynamic model however: as shown in Figure 53, the discharge calibration was performed before the cross section calibration and had not to be repeated afterwards.

		ESA Contract:	1/6287/11/I-NB
		Doc. Title	D4200 Product Validation
		Doc. No	Report NCL_CRUCIAL_D4200
		Version No	3
		Date	30.08.17

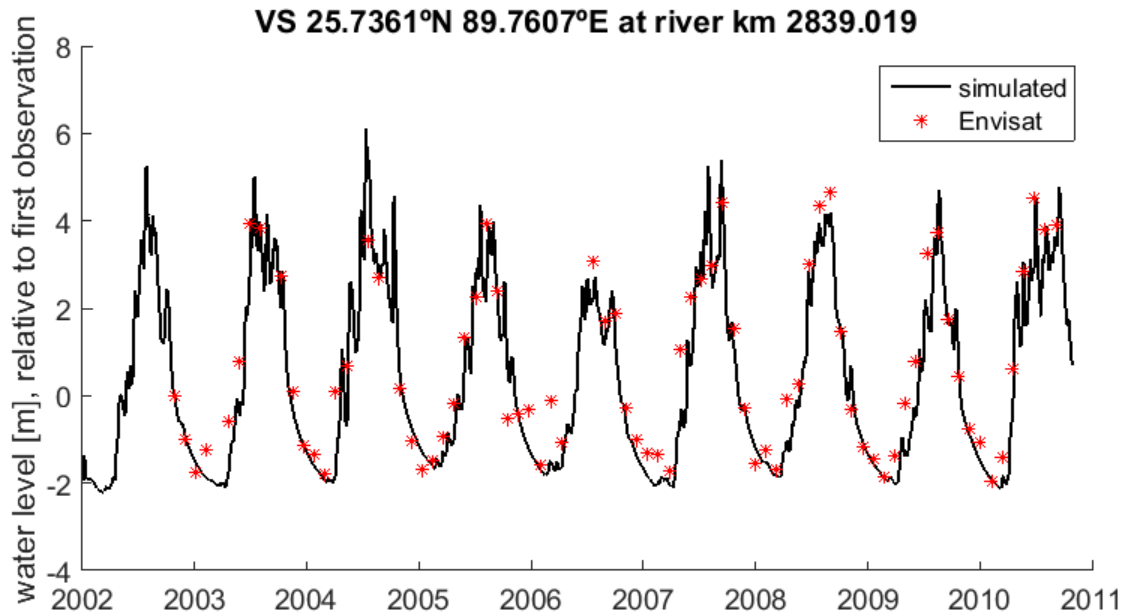


Figure 57: Result of the cross section calibration step 2 for one virtual station. All levels are relative to the water levels at the time of the first Envisat observation. The orbit provides a 35 day repeat cycle.

6.2.3 Results of synthetic DA

The just mentioned behaviour could be observed when conducting the DA experiment – see Figure 58: the original model is updated towards the hidden truth model, both in terms of discharge and water level as shown for Bahadurabad station in Figure 58 and Figure 59. The figures show a run with 0.2 metres of standard error in the synthetic observations. Most of the time, the DA model run (red) is corrected from the deterministic run of the original model (black) towards the hidden truth model (blue).

The results are reported in terms of Continuous Rank Probability Score (CRPS) (Gneiting et al., 2005) and sharpness of the ensemble's 90% confidence interval in Table 9. The CRPS is an indicator to evaluate probabilistic forecasts. Its value can be interpreted as the accumulated area between the cumulative distribution function of the forecast and the observation over all time steps. The deterministic observation is represented by a Heaviside step function. The smaller the CRPS the better the forecast, with a CRPS of 0 indicating a perfect forecast. The sharpness in this case is given as the average width of the 90% confidence interval of all ensemble runs, giving an idea of the model uncertainty. Here, the results of the DA run are compared to an open-loop run of the same setup. It can be seen that the assimilation of synthetic Cryosat-2 observations improves the CRPS by about 25%. The effect of choosing a standard error of 0.2 or 0.4 metres for the synthetic observations is small.

		ESA Contract:	1/6287/11/I-NB
		Doc. Title	D4200 Product Validation
		Doc. No	Report NCL_CRUCIAL_D4200
		Version No	3
		Date	30.08.17

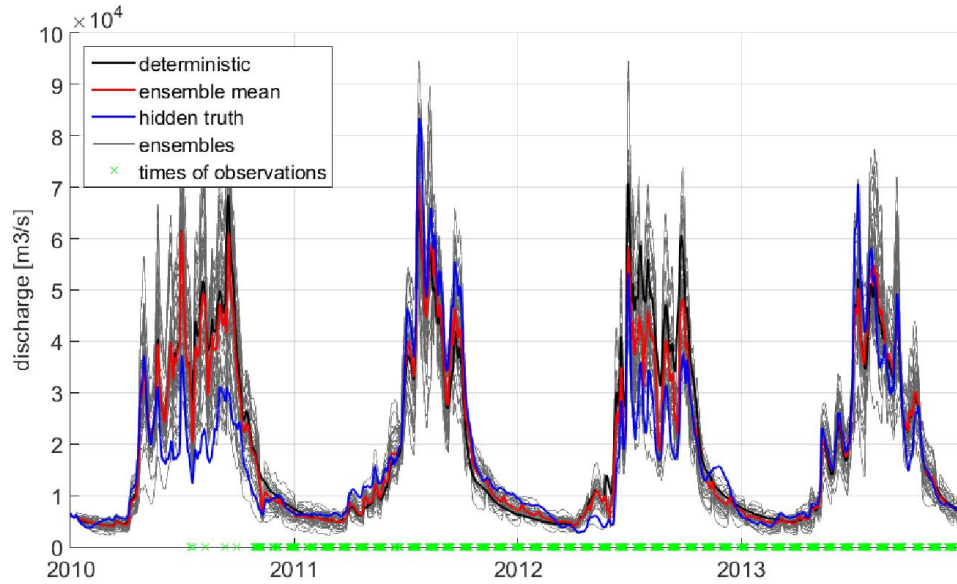


Figure 58: Results of the DA of *synthetic* Cryosat-2 data in terms of *discharge* at Bahadurabad station. The times of synthetic observations are marked with green dots on the x-axis.

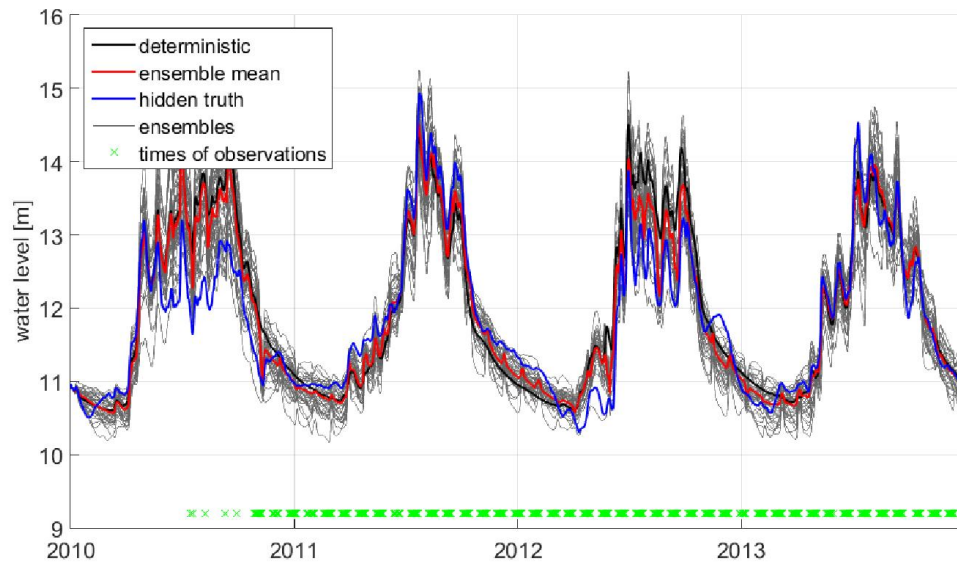


Figure 59: Results of the DA of *synthetic* Cryosat-2 data in terms of water level at Bahadurabad station. The times of synthetic observations are marked with green dots on the x-axis.

		ESA Contract:	1/6287/11/I-NB
		Doc. Title	D4200 Product Validation
		Doc. No	Report NCL_CRUCIAL_D4200
		Version No	3
		Date	30.08.17

Figure 60 shows the improvements of the model predictions along the river. On the x-axis, the location along the river is shown, moving downstream from left to right. The displayed stretch is approximately the stretch highlighted in Figure 50. It can be seen that, while moving downstream along the river, the DA helps more and more to improve the model predictions: The relative CRPS

$$CRPS_{rel} = \frac{CRPS_{DA}}{CRPS_{open}}$$

gradually improves from approximately 1 (meaning no improvement by assimilating the synthetic Cryosat-2 data) from around 0.6 (valid for the first issue) to around 0.75 (confirmed by the updated figure) at the downstream end of the stretch where Cryosat-2 data was assimilated. This applies to both CRPS in terms of water level and discharge.

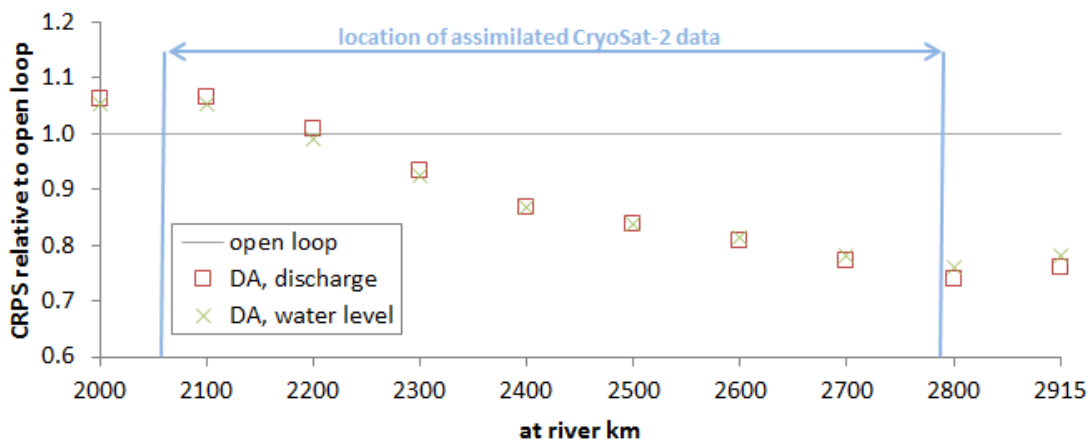


Figure 60: Relative CRPS of the DA experiment compared to the respective open-loop run along the river. Values smaller than 1, i.e. below the black line indicate that the model predictions are improved by DA.

6.2.4 Results of real DA

As a next step, actual Cryosat-2 data was assimilated to the model. The model's performance in this case was evaluated against available in situ discharge data at Bahadurabad station. This data however only was available during the high-flow seasons, i.e. usually from the beginning of April to the end of October. Results are shown in Figure 61.

		ESA Contract:	1/6287/11/I-NB
		Doc. Title	D4200 Product Validation
		Doc. No	Report NCL_CRUCIAL_D4200
		Version No	3
		Date	30.08.17

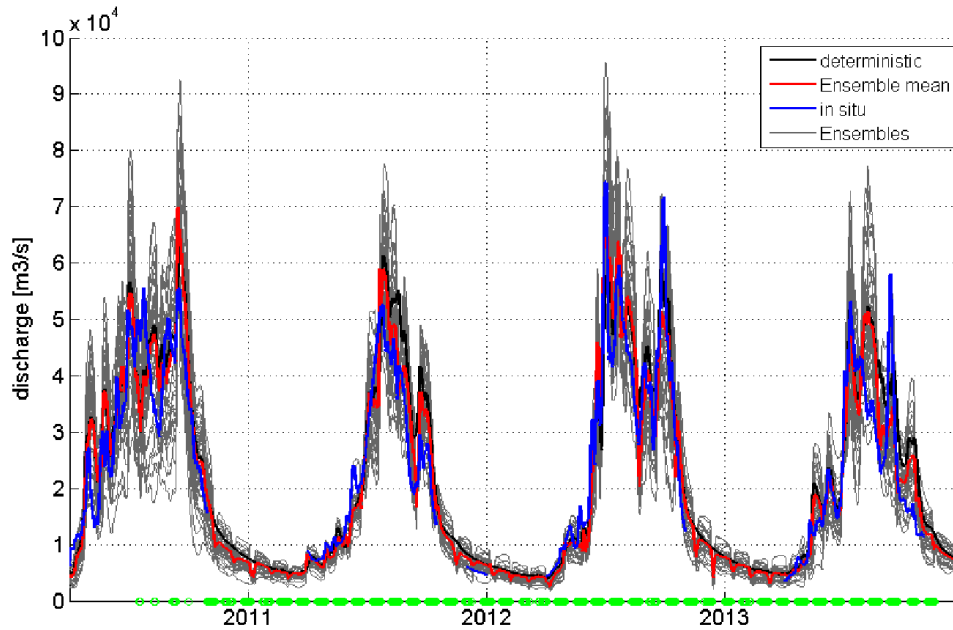


Figure 61: Results of the DA of real Cryosat-2 data in terms of discharge at Bahadurabad station. The times of observations are marked with green dots on the x-axis.

For this real case, the CRPS was improved by approximately 15% in the DA run over the open loop run (see Table 9). This is noticeably less than the 25% improvement for the synthetic case, however the synthetic case is a controlled experiment: the accuracy of the real Cryosat-2 might still have been overestimated, or there is uncertainty in the in situ observations used as a benchmark for the real case. Also, in situ data was only available for the high-flow season, and the quality of the in situ data might be low as it contains sections where values simply seem to have been interpolated linearly over a number of timesteps.

Table 9: Results of DA experiments shown in Figure 58 and Figure 61 in terms of discharge at Bahadurabad station. Sharpness is given as the width of the 90% confidence intervals

		CRPS [m ³ /s]	sharpness [m ³ /s]
synthetic data	open loop run	3688	15647
	DA, 0.2m obs. error	2778	11500
	DA, 0.4m obs. error	2757	11336
real data	open loop run	4198	14893
	DA	3557	10957

		ESA Contract:	1/6287/11/I-NB
		Doc. Title	D4200 Product Validation
		Doc. No	Report NCL_CRUCIAL_D4200
		Version No	3
		Date	30.08.17

Notable in the outcome of the assimilation of real Cryosat-2 data is the fact that during the low-flow season, the DA updates usually cause a reduction of water level and discharge in the model. It is hard to evaluate whether these updates actually improve the model's performance, as in situ observations or other validation data is lacking. However, for the validation period (which is equal to the DA period) there is a positive bias in discharge, meaning that the model is overestimating discharge (see Table 8). Also, the only existing data for the low-flow season during the DA period in December 2011 suggests that the model without DA actually is overestimating discharge and the updates improve this by correctly decreasing discharge (see Figure 61).

6.3 Conclusions

In the framework of this project, Cryosat-2 altimetry data for one of the first times was used in combination with river models. New ways of processing altimetry data over rivers and integrating it into river models had to be developed due to the distributed nature of Cryosat-2 data, not allowing the direct extraction of the commonly used virtual station water level time series.

The developed processing methods of Cryosat-2 prove to be able to extract a relevant amount of usable altimetry data along the Brahmaputra River in South Asia (see also D4100). Furthermore, a procedure of cross section calibration based on Cryosat-2 altimetry data in combination with virtual station type altimetry data was developed. This allows to obtain hydrodynamic that accurately reproduce water levels across the entire model space and time, despite lacking accurate DEM or bathymetry data for the parameterization of their cross sections. Here, the high spatial resolution of CryoSat-2 observations due to its drifting orbit is exploited. Instead of virtual station data every few tens or hundreds of kilometres along a river, CryoSat-2 provides a continuous river water level profile.

A hydrodynamic model of the Brahmaputra River prepared in such a way was used to evaluate the potential of assimilating Cryosat-2 altimetry data. The Data Assimilation Framework developed by DHI allows the assimilation of altimetry data of basically any kind of altimetry data, also arbitrarily distributed along a river. Hence, it also can cope with Cryosat-2 data. Its general capability was shown in a synthetic DA experiment, using synthetic Cryosat-2 observations of water levels. Also the assimilation of real Cryosat-2 data did improve the model prediction of in situ discharge at Bahadurabad station, even though the improvement was noticeably smaller than the one obtained in the synthetic experiment. Reasons for this can lie in the quality of the real Cryosat-2 data, or also in the quality of the available in situ discharge data. Furthermore, due to cloud cover issues, only one river mask per year could be extracted, representing low-flow conditions. Using SAR imagery instead of optical imagery, for example from Sentinel-1, should

		ESA Contract:	1/6287/11/I-NB
		Doc. Title	D4200 Product Validation
		Doc. No	Report NCL_CRUCIAL_D4200
		Version No	3
		Date	30.08.17

enable the extraction of river masks at higher frequency, ultimately increasing the amount of extracted CryoSat-2 observations. The results from the assimilation of real data for example hint to a general overestimation of discharge in the low-flow season. This is also supported by the discharge bias between simulated and observed discharge of the deterministic model at Bahadurabad station. Evaluation of the DA experiment using real Cryosat-2 data however is complicated by the limited availability of in situ or other validation data.

For the cross section calibration and DA of real altimetry data as described in chapter 6, CryoSat-2 data processed by the National Space Institute, Technical University of Denmark has been used. This was due to earlier data availability. As shown in section 4.2 however this data compares well to CryoSat-2 processed during this project by the University of Newcastle. Consequently, no major differences are expected if the same work was conducted with the data from the University of Newcastle.

		ESA Contract:	1/6287/11/I-NB
		Doc. Title	D4200 Product Validation
		Doc. No	Report NCL_CRUCIAL_D4200
		Version No	3
		Date	30.08.17

7. References

- Armitage, T., Davidson, M., 2014. Using the Interferometric Capabilities of the ESA CryoSat-2 Mission to Improve the Accuracy of Sea Ice Freeboard Retrievals. *IEEE Trans. Geosci. Remote Sens.* 42, 529–536. doi:10.1109/TGRS.2013.2242082
- Becker, M., da Silva, J., Calmant, S., Robinet, V., Linguet, L., Seyler, F., 2014. Water Level Fluctuations in the Congo Basin Derived from ENVISAT Satellite Altimetry. *Remote Sens.* 6, 9340–9358. doi:10.3390/rs6109340
- Berry, P., 2009. River and Lake Product Handbook v3.5.
- Berry, P.A.M. et al. 2010a, An enhanced ocean and coastal zone retracking technique for gravity field computation, Gravity, Geoid and Earth Observation, International Association of Geodesy Symposia 2010, 135,(3), pp. 213-220
- Berry P.A.M., Smith R.G., Witheridge S., Wheeler J., 2010b; Global Inland water monitoring from Satellite Radar Altimetry - a glimpse into the future. ESA Living Planet Symposium, Bergen, Norway, 27th June - 2nd July, ESA SP-686, ISBN 978-92-9221-250-6
- Berry P.A.M., Smith R.G., 2010c; A Global Assessment of the Envisat RA-2 Performance over Non-Ocean Surfaces. ESA Living Planet Symposium, Bergen, Norway, 27th June - 2nd July, ESA SP-686, ISBN 978-92-9221-250-6
- Berry, P.A.M., Smith, R.G. and Benveniste, J., 2012a. EnviSat altimetry for river and lakes monitoring. *International Geoscience and Remote Sensing Symposium (IGARSS)*, 1844-1847
- Berry, P.A.M., Smith, R.G., Salloway, M.K. and Benveniste, J., 2012b. Global Analysis of EnviSat Burst Echoes Over Inland Water. *IEEE Transactions on Geoscience and Remote Sensing*, 50 (5), 1980-1985
- Birkett, C., 1995. The contribution of topex/poseidon to the global monitoring of climatically sensitive lakes, *Journal of Geophysical Research: Oceans*, 100 (C12) , 25179–25204
- Birkett, C. M., L. A. K. Mertes, T. Dunne, M. H. Costa, and M. J. Jasinski, 2002, Surface water dynamics in the Amazon Basin: Application of satellite radar altimetry, *J. Geophys. Res.*, 107(D20), 8059, doi:10.1029/2001JD000609, 2002.
- Birkinshaw, S. J., O'Donnell, G. M., Moore, P., Kilsby, C. G., Fowler, H. J. and Berry, P. A. M. (2010), Using satellite altimetry data to augment flow estimation techniques on the Mekong River. *Hydrol. Process.*, 24: 3811–3825. doi:10.1002/hyp.7811
- Birkinshaw, S.J., Moore, P., Kilsby, C.G., O'Donnell, G.M., Hardy, A.J., Berry, P.A.M., 2014. Daily discharge estimation at ungauged river sites using remote sensing. *Hydrol. Process.* 28, 1043–1054. doi:10.1002/hyp.9647

		ESA Contract:	1/6287/11/I-NB
		Doc. Title	D4200 Product Validation
		Doc. No	Report NCL_CRUCIAL_D4200
		Version No	3
		Date	30.08.17

Crétaux, J-F. and Birkett, C. 2006. Lake studies from satellite radar altimetry, *Comptes Rendus Geoscience*, 338 (14), 1098–1112

Evensen, G., 2009. *Data Assimilation - The Ensemble Kalman Filter*, 2nd ed, Vasa. Springer, Berlin Heidelberg.

Frappart, F., Seyler, F., Martinez, J.-M., Leon, J.G., Cazenave, A., 2005, Floodplain water storage in the negro river basin estimated from microwave remote sensing of inundation area and water levels, *Remote Sensing of Environment*, 99 (4) 387–399

Frappart, F., Calmant, S., Cauhop, M., Seyler, F., Cazenave, A. 2006 Preliminary results of ENVISAT RA-2-derived water levels validation over the Amazon Basin, *Remote Sensing of Environment*, 100 (2) (2006), pp. 252–264

Gneiting, T., Raftery, A. E., Westveld, A. H. and Goldman, T.: Calibrated Probabilistic Forecasting Using Ensemble Model Output Statistics and Minimum CRPS Estimation, *Mon. Weather Rev.*, 133, 1098–1118, doi:10.1175/MWR2904.1, 2005.

Gommenginger, C., Martin-Puig, C., Cotton, P.D., Dinardo, S., and Benveniste, J., 2010, A prototype SAR altimeter retracker to assess the precision of SAR altimetry over the ocean. *ESA SeaSAR Workshop 25-29 January 2010*

Hernandez, F., and P. Schaeffer (2001), *The CLS01 Mean Sea Surface: A validation with the GSFC00.1 surface*, technical report, 14 pp., CLS, Ramonville St Agne, France.

Hossain, F., Maswood, M., Siddique-E-Akbor, A. H., Yigzaw, W., Mazumdar, L. C., Ahmed, T., Hossain, M., Shah-Newaz, S. M., Limaye, A., Lee, H., Pradhan, S., Shrestha, B., Bajracahrya, B., Biancamaria, S., Shum, C. K. and Turk, F. J.: A promising radar altimetry satellite system for operational flood forecasting in flood-prone bangladesh, *IEEE Geosci. Remote Sens. Mag.*, 2(3), 27–36, doi:10.1109/MGRS.2014.2345414, 2014.

Kleinherenbrink, M., Ditmar, P.G., Lindenbergh, R.C., 2014. Retracking Cryosat data in the SARIn mode and robust lake level extraction. *Remote Sens. Environ.* 152, 38–50. doi:10.1016/j.rse.2014.05.014

Michailovsky, C. I., Milzow, C. and Bauer-Gottwein, P.: Assimilation of radar altimetry to a routing model of the Brahmaputra River, *Water Resour. Res.*, 49(8), 4807–4816, doi:10.1002/wrcr.20345, 2013.

MIKE by DHI: *MIKE 11 - A Modelling System for Rivers and Channels - Reference Manual*, Hørsholm, Denmark., 2009.

Nielsen, S. A. and Hansen, E.: Numerical simulation of the rainfall runoff process on a daily basis, *Nord. Hydrol.*, 4, 171–190, 1973.

Nielsen, K., Stenseng, L., Andersen, O.B., Villadsen, H., Knudsen, P. Validation of CryoSat-2 SAR mode based lake levels. *Remote Sens. Environ.* 171, 162–170. <http://dx.doi.org/10.1016/j.rse.2015.10.023>, 2015

Paiva, R. C. D., Collischonn, W., Bonnet, M.-P., de Gonçalves, L. G. G., Calmant, S., Getirana, A. and Santos da Silva, J.: Assimilating in situ and radar altimetry data into a large-scale hydrologic-

		ESA Contract:	1/6287/11/I-NB
		Doc. Title	D4200 Product Validation
		Doc. No	Report NCL_CRUCIAL_D4200
		Version No Date	3 30.08.17

hydrodynamic model for streamflow forecast in the Amazon, *Hydrol. Earth Syst. Sci.*, 10(3), 2879–2925, doi:10.5194/hess-17-2929-2013, 2013.

Sarma, J.N., 2005. Fluvial process and morphology of the Brahmaputra River in Assam, India. *Geomorphology* 70, 226–256. doi:10.1016/j.geomorph.2005.02.007

Schwatke, C., Koch, T., Bosch, W. Satellite altimetry over inland water: A new tool to detect geoid errors!, <http://adsabs.harvard.edu/abs/2012eguga..14.7738s>, 2012.

Schwatke, C., Dettmering, D., Bosch, W. and Seitz, F.: DAHITI – an innovative approach for estimating water level time series over inland waters using multi-mission satellite altimetry, *Hydrol. Earth Syst. Sci.*, 19, 4345–4364, doi:10.5194/hess-19-4345-2015, 2015.

Smith, R.G. and Berry, P.A.M., 2011. Evaluation of the differences between the SRTM and satellite radar altimetry height measurements and the approach taken for the ACE2 GDEM in areas of large disagreement. *Journal of Environmental Monitoring*, 13 (6), pp. 1646-1652

Song, C. Huang, B., Ke, L., 2014. Inter-annual changes of alpine inland lake water storage on the Tibetan Plateau: Detection and analysis by integrating satellite altimetry and optical imagery, *Hydrological Processes*, 28 (4) (2014), pp. 2411–2418

Song C., Ye, Q., Sheng, Y., Gong, T., 2015a, Combined ICESat and Cryosat-2 Altimetry for Accessing Water Level Dynamics of Tibetan Lakes over 2003–2014, *Water*, 7, 4685–4700, doi:10.3390/w7094685

Song, C., Ye, Q., Cheng, X., 2015b. Shifts in water-level variation of Namco in the central Tibetan Plateau from ICESat and Cryosat-2 altimetry and station observations. *Sci. Bull.* 60, 1287–1297. doi:10.1007/s11434-015-0826-8

Wheeler J., Berry P.A.M., Smith R.G., Benveniste J., 2010; The ESA Near-Real-Time River & Lake Processor. ESA Living Planet Symposium, Bergen, Norway, 27th June - 2nd July, ESA SP-686, ISBN 978-92-9221-250-6

Wingham D. J., Francis C.R., Baker S., Bouzinac C., Cullen R., de Chateau-Thierry P., Laxon S.W., Mallow U., Mavrocordatos C., Phalippou L., Ratier G., Rey L., Rostan F., Viau P., and Wallis D., Cryosat: A Mission to Determine the Fluctuations in Earth's Land and Marine Ice Fields. *Advances in Space Research* 37 (2006) 841-871

Villadsen, H., Andersen, O. B., Stenseng, L., Nielsen, K. and Knudsen, P.: Cryosat-2 altimetry for river level monitoring - Evaluation in the Ganges-Brahmaputra basin, *Remote Sens. Environ.*, 168, 80–89, doi:10.1016/j.rse.2015.05.025, 2015.

Zakharova, E.A., Kouraev, A.V., Rémy, Zemtsov, V.A., Kirpotin, S.N., 2014, Seasonal variability of the Western Siberia wetlands from satellite radar altimetry, *Journal of Hydrology*, 512 (2014), pp. 366–378